



저작자표시-비영리-변경금지 2.0 대한민국

이용자는 아래의 조건을 따르는 경우에 한하여 자유롭게

- 이 저작물을 복제, 배포, 전송, 전시, 공연 및 방송할 수 있습니다.

다음과 같은 조건을 따라야 합니다:



저작자표시. 귀하는 원저작자를 표시하여야 합니다.



비영리. 귀하는 이 저작물을 영리 목적으로 이용할 수 없습니다.



변경금지. 귀하는 이 저작물을 개작, 변형 또는 가공할 수 없습니다.

- 귀하는, 이 저작물의 재이용이나 배포의 경우, 이 저작물에 적용된 이용허락조건을 명확하게 나타내어야 합니다.
- 저작권자로부터 별도의 허가를 받으면 이러한 조건들은 적용되지 않습니다.

저작권법에 따른 이용자의 권리는 위의 내용에 의하여 영향을 받지 않습니다.

이것은 [이용허락규약\(Legal Code\)](#)을 이해하기 쉽게 요약한 것입니다.

[Disclaimer](#)

공학박사 학위논문

Gas-phase synthesis of monodisperse
nanoparticles

기상공정을 이용한 단분산
나노입자의 합성

2015년 8월

서울대학교 대학원

재료공학부

양 승 민

Abstract

Gas-phase synthesis of monodisperse nanoparticles

Seungmin Yang

Department of Materials Science and Engineering

The Graduate School

Seoul National University

Nickel (Ni) nanoparticles have received great attention due to their interesting optical, magnetic, and catalytic properties. Especially, Ni nanoparticles are applied as the substitute for precious metal used as electrode materials for multilayer ceramic capacitor (MLCC). The recent trend in miniaturization of electronic components requires the MLCCs to be smaller and to have larger capacitance. Hence Ni nanoparticles as electrode material should become smaller and should be prepared as non-agglomerated spheres to improve the particle packing density.

Ni nanoparticles are generally produced by both liquid and vapor phase synthesis. The liquid phase syntheses have the advantage of producing Ni nanoparticles of uniform size and controlled shape. However low crystallinity, low purity, contamination and agglomeration of particles are inevitable in the liquid phase syntheses. On the other hand, most vapor phase syntheses have the advantage of producing highly dispersed Ni nanoparticles of high crystallinity and purity. Therefore, the vapor phase syntheses are preferred in some case, although it is difficult to control the shape and size distribution of particles in the vapor phase. Among many vapor phase processes, chemical vapor deposition (CVD) process was used for this study due to the fact that it is a promising method to produce highly crystalline and pure nanoparticles and easy to control the particle size and process conditions.

However, the degree of polydispersity and aggregates (hard-agglomerates) is a typical characteristic of particles made by gas-phase process. An aggregated mass of nanoparticles is of little benefit during densification because grain growth prevails over sintering, and generally eliminates the benefits of a narrow particle size distribution. In this research, to avoid the aggregation and to narrow the size distribution of particles, an improved vertical reactor was proposed and studied. The results show that this method is appropriate for the synthesis of monodisperse Ni particles in the gas phase. Furthermore, this method is not limited to Ni CVD process. By applying to the synthesis of Fe and Co particles, it was confirmed that this method could be applied to the synthesis of the other materials by CVD process. Also, the mechanism of this method might be applied to the other methods such as thermal decomposition and physical vapor deposition.

Meanwhile the properties of a Ni nanoparticle are determined not only by its size but also by shape, composition, and crystallinity. It was reported that the saturated magnetization of cubic Ni nanoparticles much higher than one of spherical Ni

nanoparticles of the similar size range. However it is not easy to prepare cubic Ni nanoparticles due to the facts that Ni adopts the face-centered cubic (fcc) crystal structure and the energy of {100} faces is higher than one of {111} faces. Therefore many cubic metal nanoparticles have been prepared with various surfactants to reduce surface energies of {100} faces in the liquid phase. However, in this study, we found that both cubic and spherical Ni nanoparticles could be prepared without additional surfactants and the shape of Ni nanoparticles could be controlled by adjusting conditions in CVD process. The reason why the unstable cubic Ni nanoparticles are formed without surfactants in the gas phase was also studied. Based on understanding of the shape evolution of Ni particles, cubic and spherical Ni particles could be synthesized systematically by CVD.

.....
Keyword: Monodisperse, Nickel nanoparticles, Aggregation, Gas phase synthesis, Equilibrium crystal shape

Student Number: 2011-30935

CONTENTS

| | |
|---|-----|
| Chapter 1. Introduction | 1 |
| Chapter 2. Gas-phase synthesis of monodisperse nickel nanocubes | 21 |
| Chapter 3. Shape change of fine nickel particles under hydrogen and nickel chloride vapor | 36 |
| Chapter 4. Gas-phase synthesis of monodisperse nickel nanoparticles..... | 59 |
| Chapter 5. Gas-phase synthesis of monodisperse metal nanoparticles..... | 95 |
| Chapter 6. Gas-phase coagulation of nickel nanoparticles | 104 |
| Chapter 7. Generation of charged nanoparticles during thermal evaporation of silver at atmospheric pressure..... | 111 |
| REFERENCES | 124 |
| APPENDIX | 136 |

Chapter 1. Introduction

1. Introduction of particles

Nanoparticles have attracted a great attention over the past decades not only from scientific fields but also from industrial fields [1-4]. The properties of nanoparticles such as melting temperature, band gap, magnetic and optical properties differ significantly from those of the bulk materials. Due to their fascinating properties that could not be achieved by their bulk materials, nanoparticles can be utilized in pharmacy, biomedicine, sensing, electronics, catalysis, information storage, and so on [4-27].

Among these nanoparticles, conductive metal nanoparticles such as nickel, copper, silver, have attracted great attention for the researches of conductive nanoparticle paste, internal electrode materials in multilayer ceramic capacitors (MLCCs). To follow the trend of miniaturization of electronic devices such as cellular phones, laptop, and so on, electronic components used in them should be integrated and miniaturized. These aims for MLCCs can be achieved by increasing the number of stacking layers of BaTiO₃ dielectric layers and Ni electrode layers. Therefore, the proportion of internal electrode materials is also increased. The internal electrodes of MLCCs based on BaTiO₃ were prepared conventionally with noble metals such as platinum, palladium, and silver. Hence, the increasing of internal metal electrode had led to the replacement of expensive noble metals by cheap nickel as an electrode material to decrease cost [28].

1-1. Terminology for particles sizes

In nanoscale science and technology, a particle is a small physical object which behaves as a unit concerning its transport and properties. As shown in Table 1.1 particles can be classified into 4 types by diameter according to Environmental Protection Agency (EPA) particle size terminology. Nanoparticles are the same as ultrafine particles with a size in the range of 1-100 nm. Fine particles are sized in the range of 100-2500 nm. Coarse particles are sized in the range of 2500-10000 nm.

Table 1. EPA terminology for particle sizes (d_{pa})

| EPA description | Particle size |
|-----------------|---|
| Supercoarse | $d_{pa} > 10 \mu\text{m}$ |
| Coarse | $2.5 \mu\text{m} < d_{pa} \leq 10 \mu\text{m}$ |
| Fine | $0.1 \mu\text{m} < d_{pa} \leq 2.5 \mu\text{m}$ |
| Ultrafine | $d_{pa} \leq 0.1 \mu\text{m}$ |

1.2. Terminology for assemblages of particles

The assemblage of particles is an important factor to estimate the properties of particles. There are two kinds of assemblages of particles. Due to the fact that particles have been studied in various fields, the terminology for assemblages of particles is frequently interchanged and causes a confusion as shown in Table 2. When primary particles form necks between them by chemical/sinter forces (metallic, ionic, or covalent bonds), in this study, these are termed hard-agglomerates or

aggregates difficult to break into individual primary particles. An aggregated mass of nanoparticles is of little benefit during densification because grain growth prevails over sintering, and generally eliminates the benefits of a narrow particle size distribution. The terminology for agglomerates and aggregates is summarized in Figure 1 [29].

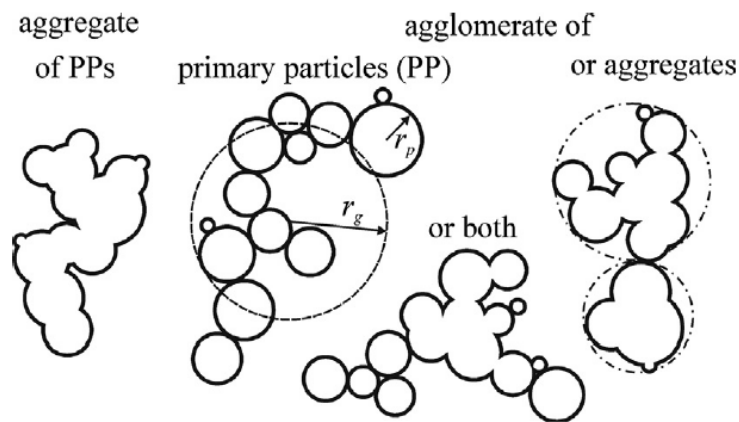


Figure 1. The structure of fractal-like particles [30]. Courtesy of Eggersdorfer et al.

Table 2. Summary of the use of the terms agglomerate and aggregate [31]. Courtesy of Nichols et al.

| Source | Assemblage of particles that is loosely bound with particles that are loosely attached by contact at their corners and edges. Readily dispersed | Assemblage of particles that is rigidly bound with particles that are firmly attached at their faces by fusion, sintering or growth. Not readily dispersed |
|--|--|---|
| BS 2955: 1993 ⁴ | Aggregate | Agglomerate |
| ISO 14887 ⁵ | Agglomerate | Aggregate |
| USP 24 2000 (Monograph 776) ⁶ | Aggregate | Agglomerate |
| Chambers Science and Technology Dictionary (1988) ² | Aggregate | Agglomerate |
| A. Van Hook (1961) ⁹ | Aggregate | Agglomerate |
| W. Gerstner (1966) ³ | Agglomerate | Aggregate |
| J.W. Mullin (1993) ⁸ | | Agglomerate |

2. Preparation of particles

Particles can be prepared by two approaches as shown in Figure 2. Top down approach refers to the milling or attrition of bulk materials to get particles. Bottom up approach refers to the growth of particles from monomers such as sol-gel method, pyrolysis, inert gas condensation, chemical vapor deposition, and so on. Both approaches have advantages and disadvantages. Top down approach induces defect and damage of particles. Furthermore, top down approach is extended from preparation of micron sized particles. Though bottom up approach is more economical, less waste process, and promises high quality particles with less defect and damage. Therefore, in nanoscience and nanotechnology, bottom up approach is generally selected to synthesize nanoparticles.

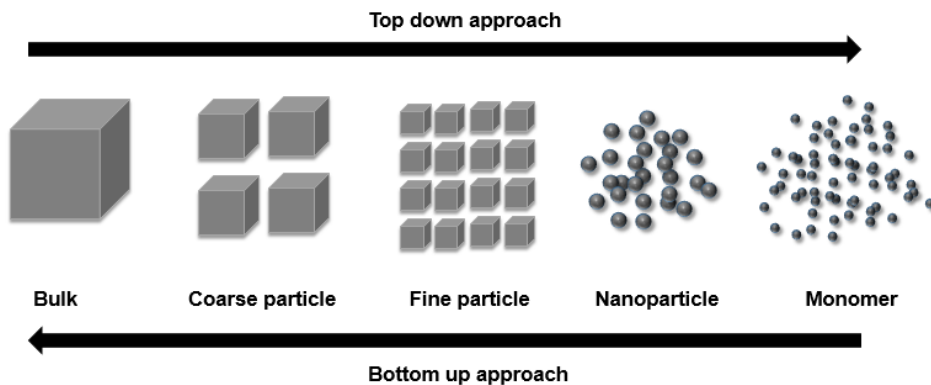


Figure 2. Top down and bottom up approaches to prepare particles.

Particles are generally produced by both liquid and vapor phase synthesis. Various methods such as thermal plasma, spray pyrolysis, chemical vapor deposition (CVD), chemical solution reduction, and others have been employed to produce nanoparticles [32, 33]. The liquid phase syntheses have the advantage of producing nanoparticles of uniform size and controlled shape. However contamination and agglomeration of particles are inevitable in the liquid phase syntheses [34, 35]. Most vapor phase syntheses have the advantage of producing highly dispersed nanoparticles of high crystallinity and purity, although it is difficult to control the shape and size distribution of particles in the vapor phase. Above all, CVD is a promising method to produce highly crystalline and pure nanoparticles and easy to control the particle size and process conditions [36].

3. Monodisperse particles

The size distribution of nanoparticles should be narrow to utilize size-dependent properties of them. Therefore, the synthesis of so-called monodisperse nanoparticles with uniform size and uniform internal structure has been intensively studied by many research groups.[37-39]

Two conditions should be achieved for the synthesis of monodisperse nanoparticles. The first condition is a separation of nucleation and growth stage. The second condition is an inhibition of coagulation. The separation of nucleation and growth stages can be achieved by high nucleation rate. If the additional nucleation in the growth stage is avoided, the particles will be under the same growth condition. And

they will grow into monodisperse particles, even though the nuclei are polydisperse. Because the growth of particles is diffusion-controlled.[40]

The coagulation of particles which is the second condition for the synthesis of monodisperse nanoparticles, can be easily inhibited by surfactants in the liquid-phase synthesis, but not in the gas-phase synthesis, because the surfactants cannot be used in the gas-phase synthesis. In the gas-phase synthesis, particles tend to aggregate due to collisions and coalescences which are caused by a high temperature and an absence of the surfactants. Hence, the aggregates (so-called hard-agglomerate) are often observed during the gas-phase synthesis of particles.[41] In spite of this disadvantage, the gas-phase syntheses are preferred due to the advantage of producing particles of high crystallinity and purity. Hence, the nanoparticles which are prepared in the gas-phase, need an additional classification process to eliminate the aggregates and to narrow the size distribution[42]. However, the additional process should be consumptive of time and cost.

3-1. Liquid phase synthesis of monodisperse particles

The synthesis of monodisperse particles in the liquid phase has been extensively studied. Recently, several methods have been developed to synthesize gram quantity monodisperse nanoparticles directly without size selection procedures. Park et al. successfully synthesized monodisperse nanoparticles with a regular shape as shown in Figure 3. These particles are prepared by burst of nucleation to enable separation of nucleation and growth stages during liquid phase process [43, 44]. Although nanoparticles have some size distribution in the nucleation stage, they became gradually monodisperse during growth. In this case, the principle for the direct

synthesis of monodisperse nanoparticles could be approached by sustained growth of nuclei formed by burst nucleation with some initial size distribution.

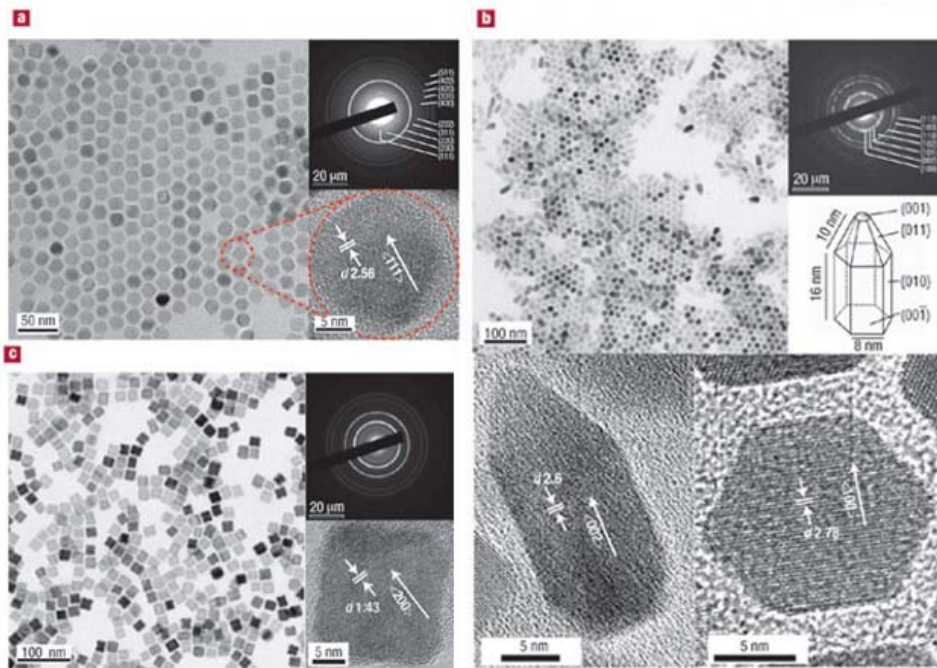


Figure 3. TEM images of monodisperse nanoparticles with a regular shape. ((a) MnO, (b) CoO, and (c) Fe) Courtesy of Park et al. [43]

3-2. Gas phase synthesis of monodisperse particles

The synthesis of monodisperse particles in the liquid phase has been reported frequently, however not in the gas phase. It is probably due to the fact that surfactant to prevent the coagulation of particles cannot be used for the synthesis of particles in the gas phase. Hence the aggregates are often observed during a gas phase

synthesis of particles. In the gas phase, particles tend to collide each other due to Brownian coagulation, and form the agglomerates. These agglomerates could change to aggregates due to the fusion, sintering of them, or growth. The formation of aggregates affects to the quality of synthesized particles. For this reason many researchers have been done about the agglomeration and aggregation for the past decades.

Aggregates are particularly attractive for sensors and electro-ceramics because their necks form long crystal planes that minimize contact resistance as well as facilitate electron flow and strong sensor signals [45]. However, an aggregated mass of nanoparticles is of little benefit during densification because grain growth prevails over sintering. Therefore aggregation generally eliminates the benefits of a narrow particle size distribution [46].

The geometric standard deviation (GSD) value at which an aerosol can be considered generally monodisperse is quite subjective, but a good rule of thumb is: monodisperse: $GSD \leq 1.25$, polydisperse: $GSD > 1.25$. Some of researchers prefers the strict conditions which is described as: monodisperse: $GSD \leq 1.1$. Generally highly-monodisperse is: $GSD \leq 1.05$.

4. Equilibrium shape of nickel

The equilibrium shape of pure nickel and the effect of carbon on changes in the equilibrium shape at 1200 °C were investigated by Hong et al. [47]. They suggested that the equilibrium crystal shape (ECS) of pure nickel is a polyhedron consisting of

{111}, {100}, {110} and {210} surfaces as shown in Figure 4. According to them, crystals with an {320} surfaces were frequently observed, and the reason of the appearance of {320} surfaces was believed that {320} surfaces were kinetically stabilized metastable surfaces, which remained during the thermal equilibrating process. It is probably due to a high nucleation energy barrier for the removal of the {320} surfaces.

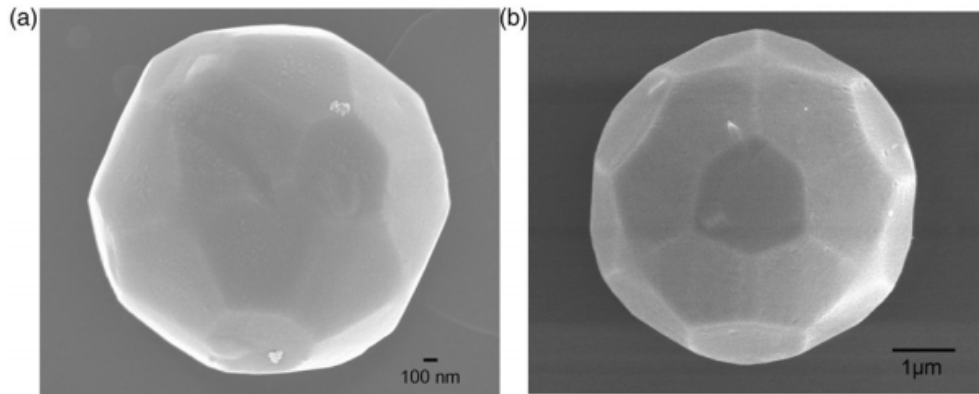


Figure 4. Near-equilibrium shape of pure nickel crystals annealed at 1200 °C for 100 h under 10^{-4} Torr atmospheric pressure. Courtesy of Hong et al. [47].

5. Non-classical crystallization

5-1. Non-classical crystallization in the liquid phase

Recently, a great finding in relation to nanoparticles has been made that nanoparticles can be a building block in crystal growth. This finding is revolutionary because the crystal growth based on atomic, molecular or ionic unit was so firmly established and believed. This new concept that crystals can grow by a building block of nanoparticles is called ‘non-classical crystallization’ in contrast with the classical crystallization where individual atoms or molecules are the building unit. Cölfen and Antonietti ([48]) made an extensive review on non-classical crystallization and made a meaningful remark that reanalyzing the literature, this mechanism turns out to be a ‘‘rediscovery’’, as it seems that many important original observations are meanwhile forgotten and hidden in the past literature, as they simply did not comply with the classical crystallization model ([48]). Non-classical crystallization has become a hot issue in the crystal growth community and extensively studied especially in the crystal growth in solution ([49, 50]; [51]; [52]; [53]; [54]). Recently, the direct evidences for non-classical crystallization were reported. Using a silicon nitride liquid cell for in-situ TEM observation, Liao et al. made detailed real-time imaging showing how Pt₃Fe nanorods grow by nanoparticles in solution ([55]) as shown in Figure 5. By in-situ TEM observation using graphene liquid cells, Yuk et al. made direct atomic-resolution imaging showing how Pt crystals grow in solution ([56]) as shown in Figure 6. The imaging clearly reveals that Pt nanocrystals grow not only by monomers but also by the coalescence of nanoparticles.

5-2. Non-classical crystallization in the gas phase – theory of charged nanoparticles

Although these studies on non-classical crystallization deal with the crystal growth in solution, Hwang et al. extensively studied non-classical crystallization of thin films and nanostructures in the gas phase synthesis by chemical vapor deposition (CVD) ([57]; [58]). In contrary to the previous belief that thin films and nanostructures should grow by an individual atom or molecule, Hwang et al. suggested a theory of charged nanoparticles (TCN), where charged nanoparticles (CNPs) are spontaneously generated in the gas phase and contribute to the growth of thin films and nanostructures in most conventional CVD processes ([57, 58]).

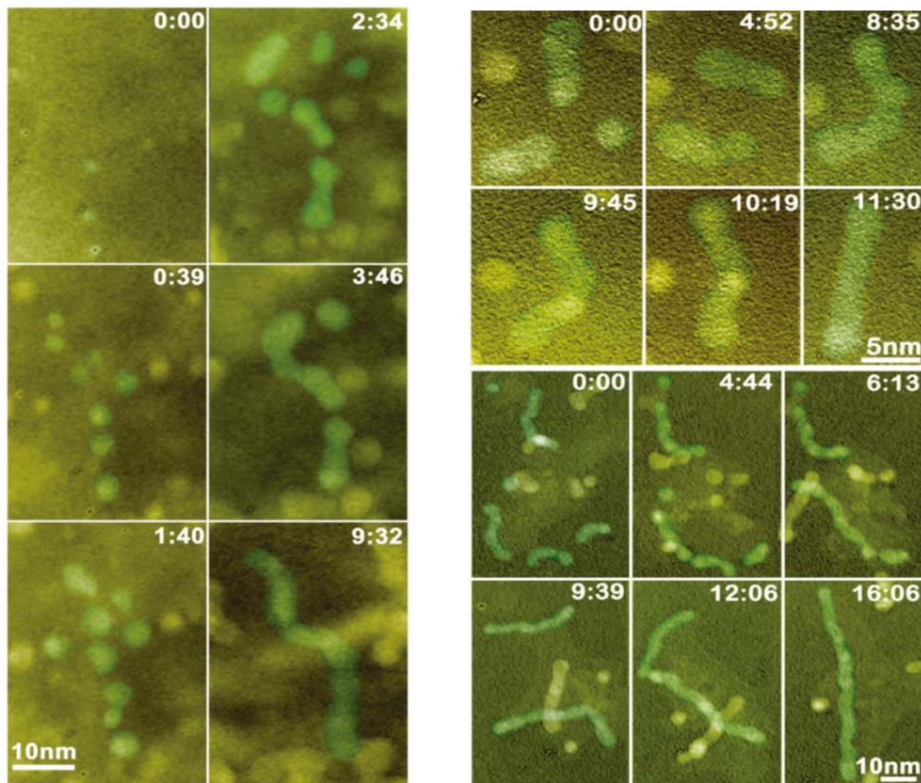


Figure 5. The direct observation of Pt_3Fe nanorods growth by in-situ TEM. Courtesy of Liao et al. [55]

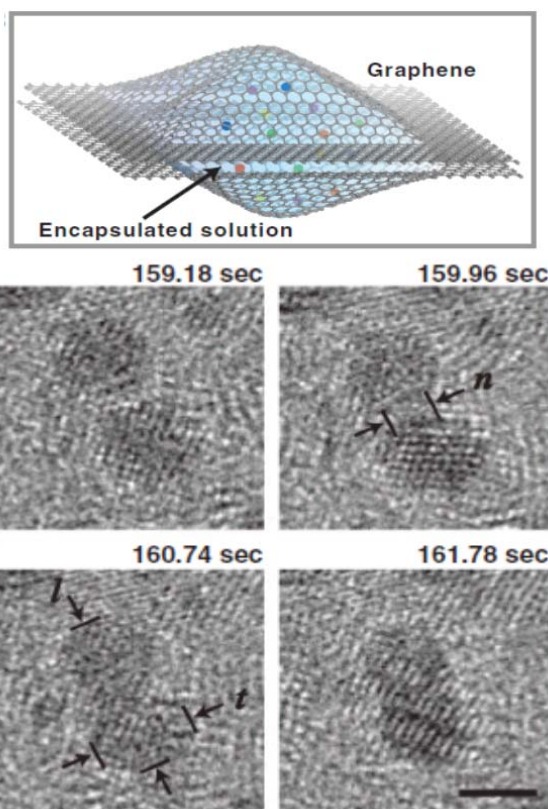


Figure 6. Pt nanocrystals grow not only by monomers but also by the coalescence of nanoparticles. This work was performed by in-situ TEM using graphene liquid cells. Courtesy of Yuk et al. [56]

In addition to the concept of non-classical crystallization, they emphasize the role of charge carried by nanoparticles, which makes the nanoparticle liquid-like. In other words, the charge enhances atomic diffusion. Therefore, the reason why CNPs can be a building block in the growth of high quality films and nanostructures with highly

smooth surface without voids is attributed to the liquid-like property of CNPs. The liquid-like property is diminished with increasing number of atoms per charge. Therefore, if nanoparticles are singly charged, smaller nanoparticles are more liquid-like than larger ones. Therefore, neutral nanoparticles (NNPs) produce porous films whereas CNPs produce dense films. In relation with this fact, Youn et al.[59] reported that CNPs produce nanowires or a dense silicon film on the floating substrate but produce porous structures on the grounded substrate as shown in Figure 7.

According to this new understanding, in the aerosol deposition process, where nanoparticles are carried through the pipe and made to deposit as films, the nanoparticles should be charged to produce dense films. Considering that films produced by aerosol deposition tend to be dense, it can be predicted that nanoparticles must be charged unintentionally. However, nanoparticles tend to be self-charged through contact ionizations or triboelectricity between nanoparticles and between the nanoparticle and the wall.

In relation to this possibility, Fuchita et al. ([60, 61]) reported that the film could be fabricated by aerosol deposition. They also observed luminescence, which was concluded to be due to static electricity induced by the friction between powder particles, the carrier tubing and the nozzle.

Considering these, it is worth studying whether the nanoparticles produced by thermal evaporation are self-charged or not. If nanoparticles are charged, their deposition behavior would be affected by the electric bias. In relation to the possibility of the generation of charged nanoparticles, extensive studies have been made in the CVD process. By measuring the size distribution of charged

nanoparticles using nano-DMA or conventional DMA, Kim et al. confirmed that charged nanoparticles are spontaneously generated without exception during the syntheses of ZnO nanowires shown in Figure 8([62]), carbon nanotubes ([63]), silicon nanowires shown in Figure 9([64]) and silicon films ([65]) under a typical CVD process.

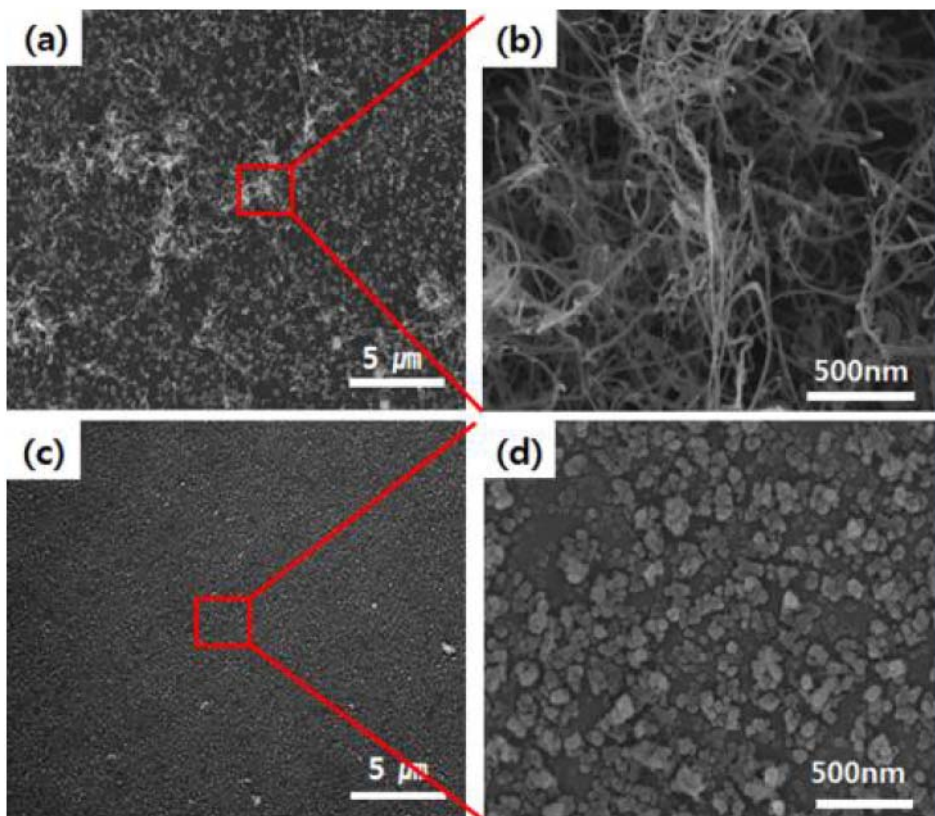


Figure 7. FESEM images: (a) low-magnification and (b) high-magnification images of a floating silicon substrate and (c) low-magnification and (d) high-magnification images of a grounded silicon substrate at a N_2 flow rate of 500 sccm. Courtesy of Youn et al. [59]

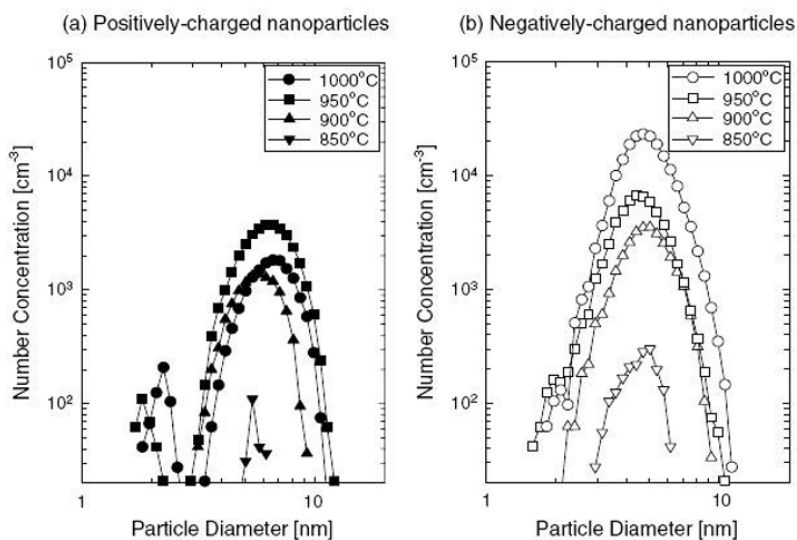
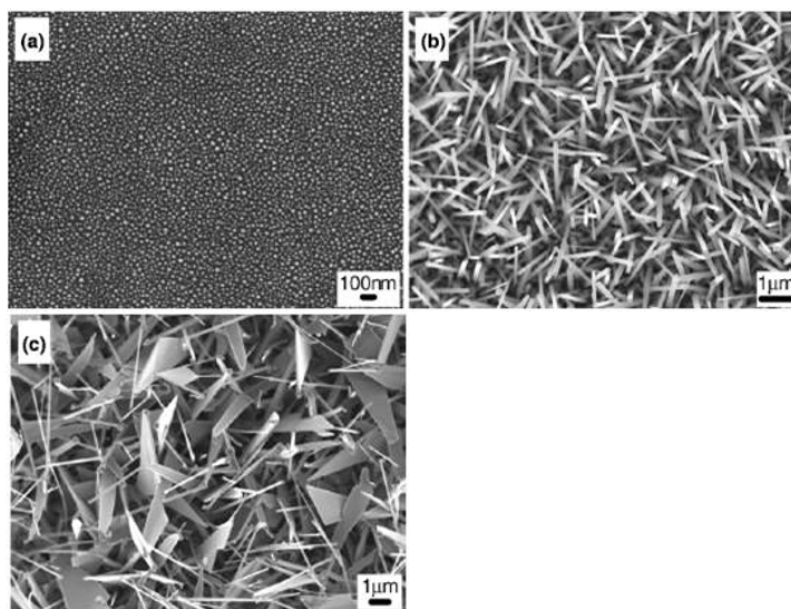


Figure 8. Top image: FESEM images of ZnO nanowires and nanosheets at reactor temperatures of (a) 800°C, (b) 900°C, and (c) 1000°C. Bottom image: The size distribution of (a) positively and (b) negatively charged ZnO nanoparticles measured at the same conditions. Courtesy of Kim et al. [62]

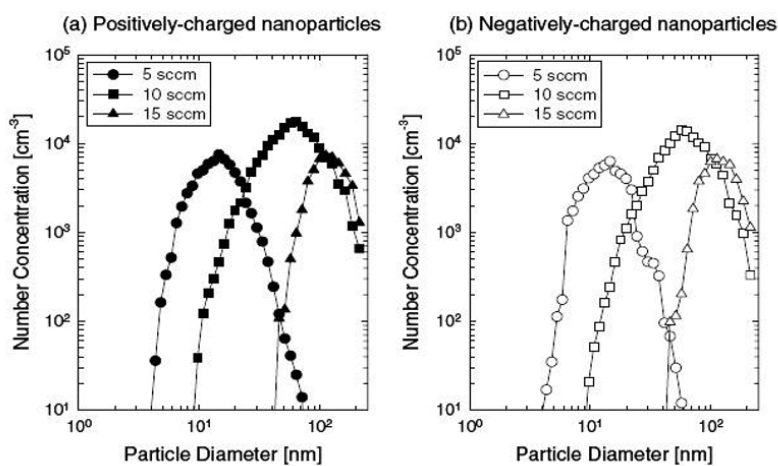
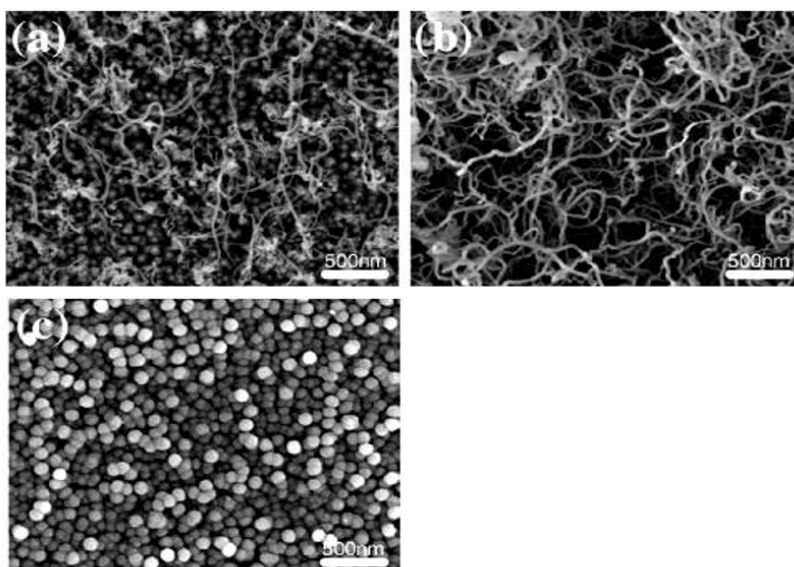


Figure 9. Top image: FESEM images of Si nanowires and nanoparticles at hydrogen flow rates of (a) 5, (b) 10, and (c) 15 sccm at a SiCl₄/H₂ molar ratio of 0.05 and a reactor temperature of 975°C. Bottom image: The size distribution of (a) positively and (b) negatively charged nanoparticles measured at the same conditions. Courtesy of Kim et al. [62]

Using the same technique, Lee et al. could confirmed that charged GaN nanoparticles are generated under the growth condition of GaN films and nanowires ([66]). Using a particle beam mass spectroscopy (PBMS), which was developed to measure the size distribution of nanoparticles at low pressure, Hong et al. could measure the size distribution of charged silicon nanoparticles during hot wire CVD at 1.5 torr and confirm that charged nanoparticles were spontaneously generated also under the film deposition condition of the low pressure CVD process ([67]).

Generally, the heating of metal results in thermionic emission of electrons from the heated hot metal surface to the gas phase as shown in Figure 10. The amount of emitted electrons from hot wires is determined by Richardson-Dushman equation [68] which is described as

$$J = AT^2 \exp\left(-\frac{WF}{kT}\right) \quad (1)$$

where J, A, k and T are respectively a current density, Richardson constant, Boltzmann constant, and a temperature of a heated hot metal surface. WF is the work function of metal. The current density increases with increasing the temperature of the metal and decreasing WF of the metal. These thermal emission of electrons is believed to contribute to negative charge carriers.

On the other hand, the generated particles in the gas phase would be electrically charged by a surface ionization as shown in Figure 11, can be described by Saha-Langmuir equations [69] which is described as

$$\frac{n^+}{n^o} = \frac{g^+}{g^o} \exp\left(-\frac{IP - WF}{kT}\right) \quad (2)$$

$$\frac{n^-}{n^o} = \frac{g^-}{g^o} \exp\left(-\frac{WF - EA}{kT}\right) \quad (3)$$

where n^o , n^+ , and n^- are the numbers of neutral, positive, and negative charge carriers, respectively. g^o , g^+ , and g^- are the statistical weight of neutral, positive, and negative charge carriers, respectively. IP , EA , WF , k , T are respectively the ionization potential, electron affinity, work function of the substances which is related to the surface ionization, and Boltzmann constant.

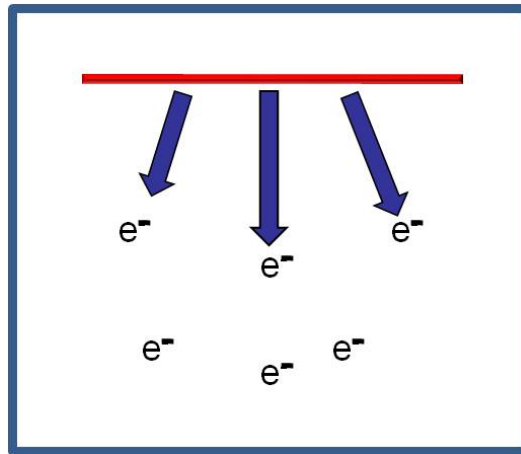
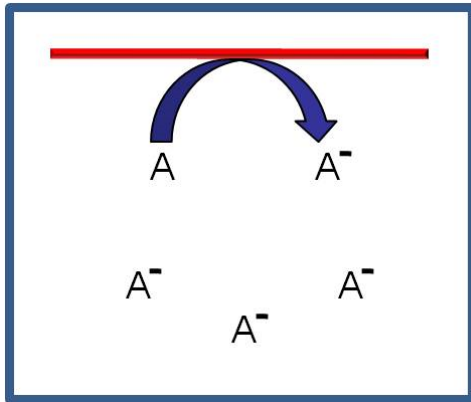
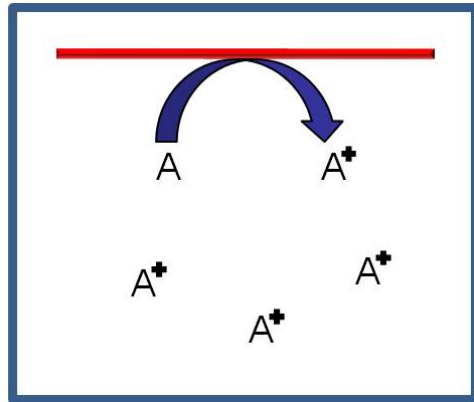


Figure 10. A schematics of thermionic emission of electrons from the heated hot metal surfaces..



(a) Negative surface ionization



(b) Positive surface ionization

Figure 11. A schematics of surface ionization.

Chapter 2. Gas-phase synthesis of monodisperse nickel nanocubes

1. INTRODUCTION

The size distribution of nanoparticles should be narrow to utilize size-dependent properties of them. Therefore, the synthesis of so-called monodisperse nanoparticles with uniform size and uniform internal structure has been intensively studied by many research groups.[37-39]

Two conditions should be achieved for the synthesis of monodisperse nanoparticles. The first condition is a separation of nucleation and growth stage. The second condition is an inhibition of coagulation. The separation of nucleation and growth stages can be achieved by high nucleation rate. If the additional nucleation in the growth stage is avoided, the particles will be under the same growth condition. And they will grow into monodisperse particles, even though the nuclei are polydisperse. Because the growth of particles is diffusion-controlled.[40] Monodisperse nanoparticles were successfully synthesized with a regular shape by Park et al.[43, 44]. These particles are prepared by burst of nucleation to enable the separation of nucleation and growth stages.

The coagulation of particles which is the second condition for the synthesis of monodisperse nanoparticles, can be easily inhibited by surfactants in the liquid-phase synthesis, but not in the gas-phase synthesis, because the surfactants cannot be used in the gas-phase synthesis. In the gas-phase synthesis, particles tend to aggregate due to collisions and coalescences which are caused by a high temperature and an absence of the surfactants. Hence, the aggregates (so-called hard-agglomerate) are often observed during the gas-phase synthesis of particles.[41] In spite of this disadvantage, the gas-phase syntheses are preferred due to the advantage of producing particles of high crystallinity and purity. Hence, the nanoparticles which

are prepared in the gas-phase, need an additional classification process to eliminate the aggregates and to narrow the size distribution[42]. However, the additional process should be consumptive of time and cost.

The shape of particles is also an important factor to determine the property of nanoparticles. For example, it was reported that the cubic Ni particles have much higher saturated magnetization than a spherical Ni particles of the similar size.[70, 71] In our preliminary study which will be reported in the other publication, it was confirmed that high and low reduction rate of NiCl₂ which is a reactant in Eq. (1), favor respectively spherical and cubic Ni particles due to the adsorption of NiCl₂ on {100} faces of Ni particles during chemical vapor deposition (CVD).

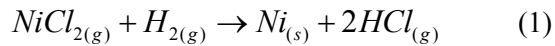
In this research, a modified vertical reactor was proposed and studied for the synthesis of non-aggregated and monodisperse Ni nanocubes. The cubes were synthesized by CVD which is one of the most simple method to produce highly crystalline and pure Ni nanoparticles.[36]

2. EXPERIMENTAL PROCEDURE

The experiments were carried out in the 2-stage horizontal tubular reactor shown in Figure 1(a) and 2-stage vertical tubular reactor shown in Figure 1(c). Both reactors consist of a quartz tube with an inner diameter of 4.5 cm and a length of 120 cm. Carrier gas N₂ and reduction gas H₂ were passed through (10) and (11) respectively at the flow rates of 500 and 125 sccm. The inlets of H₂ and N₂ for the horizontal reactor both consist of one quartz tube. The flow direction in the horizontal reactor

is vertical to the gravity. Hence, when a hot gas meets a cold gas, the cold gas tends to sink in the gravity direction due to higher density of the cold gas than one of the hot gas. Because of this buoyancy effect, an axisymmetric gas flow cannot be made. On the other hand, an axisymmetric gas flow can be made in the vertical reactor. Therefore, the inlets of H₂ and N₂ for the vertical reactor both consist of six quartz tubes to make gas flow axisymmetric.

A commercial nickel (II) chloride (NiCl₂) powder (98%, Aldrich) was put in the quartz crucible, which was placed in the center of the first heating zone (8) in Figure 1(a) and (c). NiCl₂ is reduced by H₂ in the middle of the second heating zone (7) in Figure 1(a) and (c), the reduction is shown in Eq. (1).



The first heating zone temperature which is equal to evaporation temperature, was 850 and 900 °C respectively for the vertical and horizontal reactors. The second heating zone temperature was varied at 950 and 1050 °C for the vertical reactor, and fixed at 950 °C for the horizontal reactor. The outlet position is fixed at the right end of the reactor when the horizontal reactor was used. The outlet position was varied at 70 and 80 cm when the vertical reactor was used. The temperature of the reduction zone or the region where NiCl₂ vapor begins to mix with H₂, was measure by a thermocouple.

The particle collection was done for 30 min by filter which is connected to the outlet. The collected Ni particles were characterized by field-emission scanning electron microscope (FESEM, SU-70, Hitachi), transmission electron microscope (TEM,

Tecnai F20, FEI). Ni particles were dispersed in deionized water by ultrasonic vibration. TEM sample were prepared by dropping solutions containing Ni particles on holey carbon-coated copper grids.

The temperature distribution of the horizontal and vertical reactors and particle trajectory for the vertical reactor are analyzed by a commercial CFD code (ANSYS Fluent v16.0). As mentioned, the flow direction in a horizontally placed reactor is vertical to the gravity, so that an axisymmetric 2D model cannot be used due to the buoyancy effect. Hence, for a horizontal reactor, a half-cylindrical 3D model was used, so that the gravity could be taken into account by the buoyancy effect. This study is focused in the behavior of particles in a reactor. Therefore, the first heating zone and an injection of H_2 in the horizontal reactor were not considered to simplify the calculation. On the contrary, the flow direction in the vertical reactor is horizontal to the gravity. Hence, an axisymmetric 2D model was used for the analysis of the vertical reactor and the first heating zone was not considered for the same reason.

In the calculation, gases were assumed to be ideal and incompressible. The temperature-dependent density of gases was considered to determine the buoyancy effect. The wall boundary conditions represent the inner surface of tube wall, so that the heat conduction through tube wall was not considered. Insulator placed between cooling and heating zone was assumed to be perfect thermal insulator. The boundary conditions for both horizontal and vertical reactor are summarized in Table 1.

Figure 1(a) shows a typical temperature distribution of a horizontal reactor. Away from the hot zone whose length is shorter than a half length of the heating zone, the temperature drops steeply. In this region, the hot and cold gases should coexist. The hot gas having lower density than the cold gas tends to float due to the buoyancy. The hot gas will be cooled by cold wall, and then it will tend to sink. Hence the gas

flow will circulate. The tendency of gas flow to circulate increases a residence time of particles, and the chance of aggregation. The circulating flow also widens a residence time distribution of particles. It means that all particles cannot be under the same conditions for growth. Consequently the temperature gradient of this region will cause a poor quality of nanoparticles.

Table 1. Boundary conditions for CFD analysis.

| Reactor | Type | Boundary | Value |
|-----------------|-----------------|--------------|--------------------|
| Horizontal | Wall | Cooling zone | 300 K |
| | | Insulator | 0 W/m ² |
| | | Heating zone | 1300 K |
| | Velocity inlet | Nitrogen | 0.005 m/s |
| | Pressure outlet | Outlet | 0 Pa |
| | Vertical | Wall | Cooling zone |
| Insulator | | | 0 W/m ² |
| Heating zone | | | 1300 K |
| Velocity inlet | | Nitrogen | 0.022 m/s |
| | | Hydrogen | 0.006 m/s |
| Pressure outlet | | Outlet | 0 Pa |

For this reason, a modified vertical reactor as shown in Figure 1(c) is proposed in this study. For a narrow residence time distribution and a short mean residence time, the gas flow in a reactor should be axisymmetric. The vertical reactor was used, because the horizontal reactor is not suitable to achieve the axisymmetric gas flow due to the fact that the flow direction is vertical to the gravity in a horizontal reactor. However, the buoyancy effect is inevitable in both horizontal and vertical reactors due to the fact that there are regions where cold and hot gases coexist in both reactors as shown in Figure 1(b) and (e). Therefore, it is important that particles should not be in the region where cold and hot gases coexist.

For this reason, H_2 is injected to the top of a vertical reactor, and the outlet is placed at the middle of the reaction zone. The trajectory of particles as shown in Figure 1(d) indicates that particles are exhausted without residence in the buoyancy region. It also shows that the narrow residence time distribution and the short mean residence time can be achieved by the modified vertical reactor.

Particles pass through the outlet tube with the inner diameter of ~ 4 mm, therefore they will reach to the cooling zone where the temperature is low enough to prevent collision and coalescence of particles in a short time. It means that this condition is suitable not only for the synthesis of monodisperse particles, but also for the avoiding of the formation of aggregates in the gas phase.

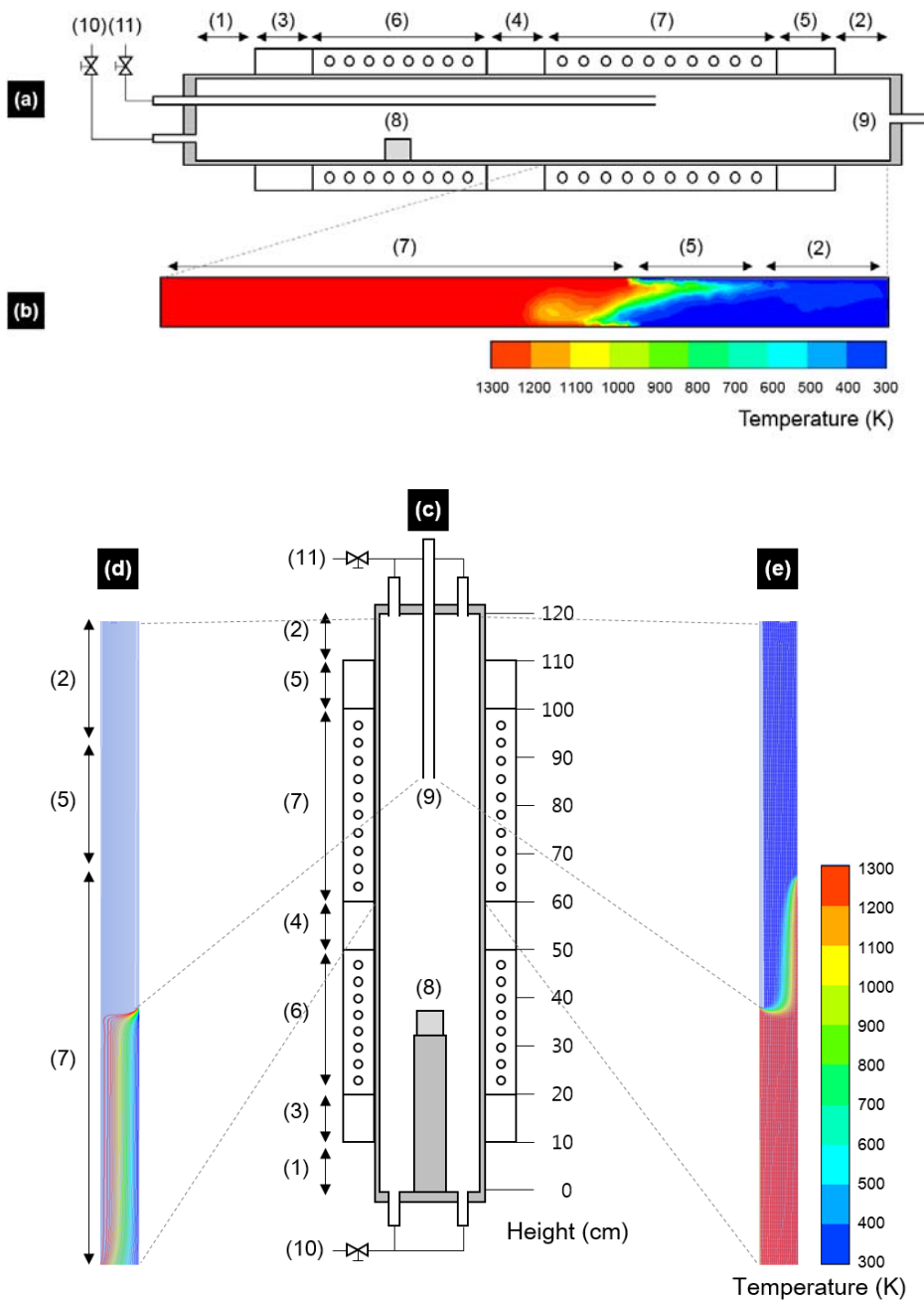


Figure 1. Schematics of reactors: (a) the horizontal reactor, (c) the vertical reactor. CFD analyzed temperature distribution in reactors: (b) the horizontal reactor, (e) the

vertical reactor. CFD analyzed trajectory of particles: (d) the vertical reactor. (1, 2) cooling zone, (3-5) insulation, (6) first heating zone, (7) second heating zone, (8) NiCl₂ in crucible, (9) outlet, (10) N₂ inlet, (11) H₂ inlet

3. RESULTS AND DISCUSSION

To compare the horizontal and vertical reactors experimentally, microstructures of Ni particles prepared by both reactors were observed as shown in Figure 2. The size of Ni particles in Figure 2 was obtained by approximately measuring of the edge and diameter respectively of cubes and spheres with a ruler. From these measurement, the geometric standard deviation (GSD) and the mean size of particles were calculated. The size distribution of Ni particles in Figure 2 are presented in Figure 3.

Figure 2(a) shows the FESEM image of Ni particles prepared by the horizontal reactor under the first and second heating zone temperatures of 900 and 950 °C respectively. All Ni particles show the cubic shape. The mean size is approximately 205 nm, and the GSD is 1.46.

Figure 2(b) shows the FESEM image of Ni particles prepared by the vertical reactor under the first and second heating zone temperatures of 850 and 1050 °C respectively. The outlet was placed at 80 cm high. Both cubic and spherical Ni particles were observed. The ratio of cubes to spheres is lower than 0.5. The mean sizes of cubes and spheres are approximately 309 and 237 nm respectively. GSD of cubes and spheres are 1.23 and 1.15 respectively.

Figure 2(c) shows the FESEM image of Ni particles prepared by the vertical reactor under the first and second heating zone temperatures of 850 and 1050 °C respectively. The outlet was placed at 70 cm high. All Ni particles show the cubic shape. The mean size is approximately 114 nm, and the GSD is 1.17.

Figure 2(d) shows the FESEM image of Ni particles prepared by the vertical reactor under the first and second heating zone temperatures of 850 and 950 °C respectively. The outlet was placed at 80 cm high. All Ni particles show the cubic shape. The mean size is approximately 172 nm, and the GSD is 1.21.

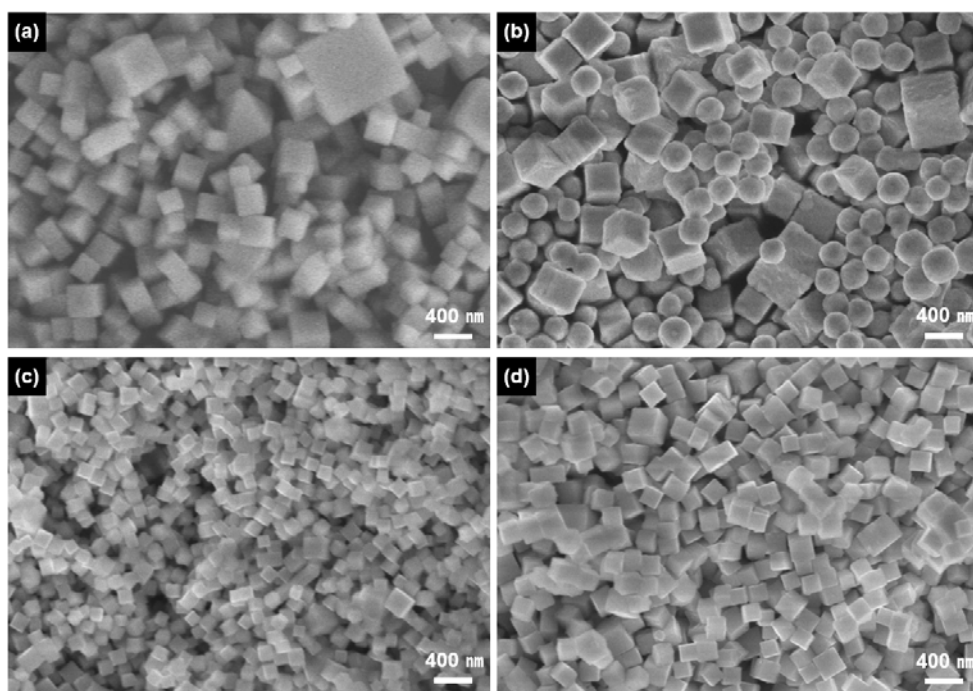


Figure 2. FESEM images of Ni particles prepared by (a) the horizontal reactor under the first and second heating zone temperatures of 900 and 950 °C respectively, and by the vertical reactor under (b) the first and second heating zone temperatures of 850 and 1050 °C respectively, and the outlet was placed at 80 cm high, (c) the first

and second heating zone temperatures of 850 and 1050 °C respectively, and the outlet was placed at 70 cm high, and (d) the first and second heating zone temperatures of 850 and 950 °C respectively, and the outlet was placed at 80 cm high.

TEM results of cubic particles in Figure 2(c) and (d) are presented in Figure 4(a) and (b). The diffraction pattern of the cubic particles both in the inset of Figure 4(a) and (b), matched the reflection of {200} faces of single-crystalline Ni, confirming that the cubic particles are pure single-crystalline Ni.

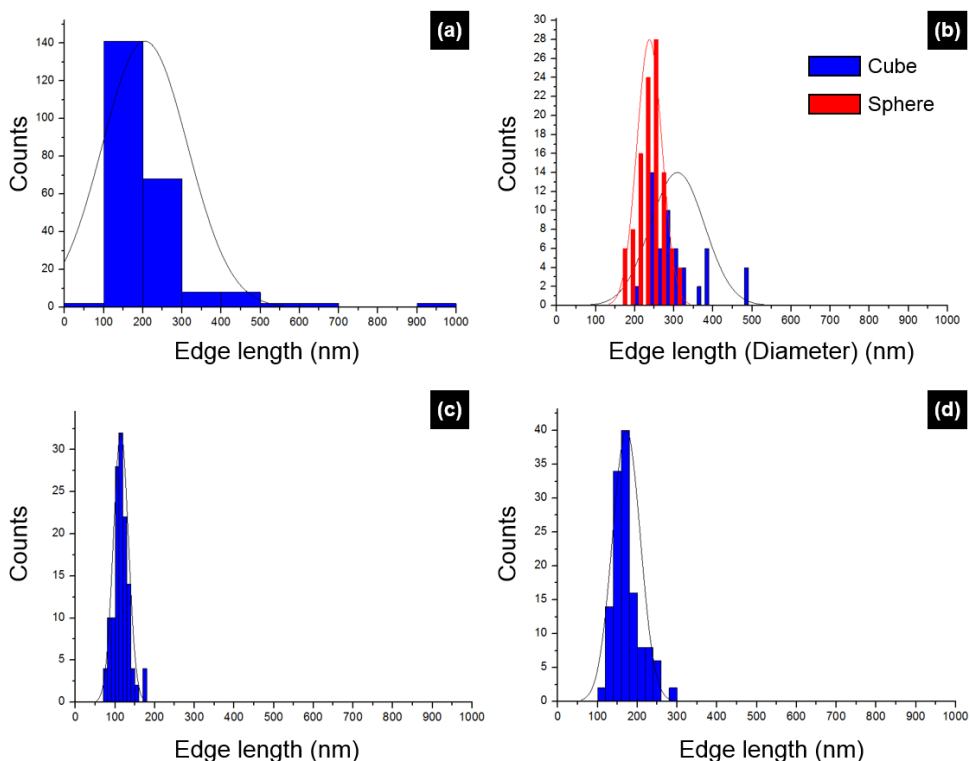


Figure 3. Size distribution of Ni particles in (a) Figure 2(a), (b) Figure 2(b), (c) Figure 2(c), and (d) Figure 2(d).

The reason why cubic and spherical Ni particles were observed in Figure 2(b) is explained by the reduction rate of NiCl₂. In the other study which will be introduced in the next chapter, it was confirmed that high and low reduction rate of NiCl₂ favor respectively spherical and cubic Ni particles due to the adsorption of NiCl₂ on {100} faces of Ni particles during CVD.

By this understanding, the Ni particles of both shapes in Figure 2(b) indicates that the reduction rate was too high or the vapor pressure of NiCl₂ was not enough to synthesize only cubic Ni particles. Therefore, to synthesize only cubes, the reduction rate should be decreased or the vapor pressure of NiCl₂ should be increased. In this study, the reduction rate was controlled for the synthesis of cubes by two ways. The first way is shifting of the outlet position. And the second way is lowering of the second heating zone temperature.

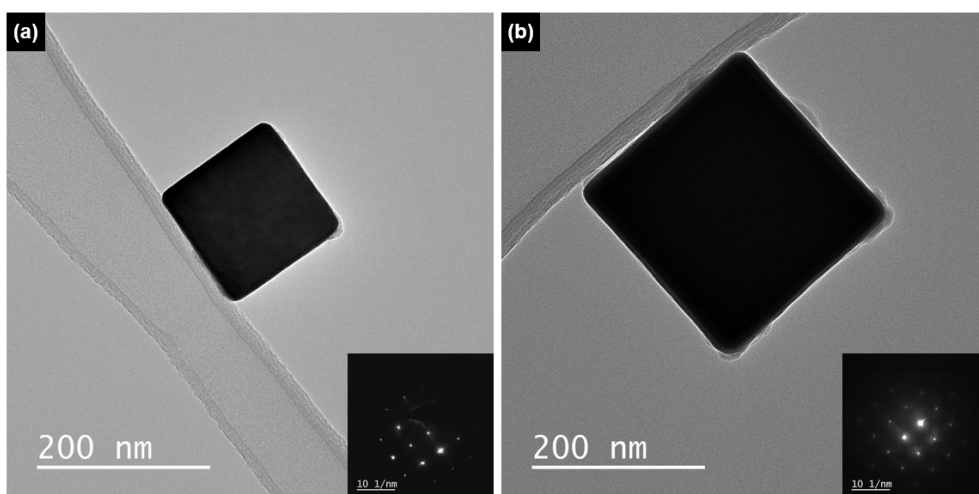


Figure 4. TEM images of cubic Ni particles of samples in (a) Figure 2(c) and (b) Figure 2(d).

The reduction temperature was controlled to decrease the reduction rate by shifting of the outlet position. The location of the reduction zone where the NiCl_2 and H_2 are mixed, is depend on the position of the outlet. For example, if the outlet is lowered from 80 to 70 cm high, the location of the reduction zone will be lowered approximately from 64 to 56 cm when the under the first and second heating zone temperatures of 850 °C and 1050 °C respectively. These locations of the reduction zones were roughly measured by observation of Ni films on the inner wall after the synthesis of particles. Furthermore, the temperature in the reactor decreases steeply away from the hot zone as mentioned before. Therefore, if the outlet which is placed at the middle of the second heating zone which is (7) in Figure 1(c), is lowered to the insulation which is (4) in Figure 1(c), the location of reduction zone should be lowered. To synthesize cubic Ni particles shown in Figure 2(c), the outlet position was shifted from 80 to 70 cm, and the reduction zone was shifted to approximately 56 cm where the temperature is approximately 902 °C. According to the fact that all Ni particles show the cubic shape in Figure 2(c), this condition seems to be appropriate for the synthesis of cubes including the reduction temperature and residence time of particles. As mentioned before, the high nucleation rate is required to synthesize monodisperse particles. It is expected that the size distribution of cubes in Figure 2(c) might be improved by shifting the outlet position precisely between 70 and 80 cm, considering of the shape change of particles.

To lower the reduction temperature, the second heating zone temperature was decreased from 1050 to 950 °C for the synthesis of cubic Ni particles in Figure 2(d). The location of the reduction zone was approximately 68 cm where the temperature is approximately 916 °C. According to the fact that all Ni particles show the cubic shape in Figure 2(d), this condition seems to be appropriate for the synthesis of cubes.

The mean size difference between cubes in Figure 2(c) and (d) is probably due to the different residence times of particles under conditions in Figure 2(c) and (d).

The GSD of cubic Ni particles prepared by the horizontal reactor in Figure 2(a) is far from the GSD of monodispersity which is lower than 1.25. On the contrary, the GSDs of Ni particles prepared by vertical reactor in Figure 2(b)-(d), are lower than 1.25 without exceptions.

Cubes in Figure 2(a) shows non-aggregated cubic Ni particles, even though they were synthesized by the horizontal reactor. This is might be due to the adsorption of NiCl_2 on the $\{100\}$ surfaces. Therefore, the reason why non-aggregated cubic Ni particles in Figure 2(c), (d) were synthesized, might be expected that the aggregations were prevented by the adsorption of NiCl_2 on the surfaces. However, Figure 2(b) shows rarely aggregated spheres which should not be adsorbed by NiCl_2 . Consequently, the condition of the vertical reactor for the synthesis of Ni particles seems to be suitable for the synthesis of monodisperse and non-aggregated Ni particles.

4. CONCLUSIONS

In conclusion, it was confirmed that the monodisperse cubic Ni particles can be synthesized by the vertical CVD reactor. By injecting H_2 to the top of the reactor and placing the outlet in the middle of the second heating zone, the flow which affects to the residence time of particles, can be appropriately controlled for the synthesis of monodisperse cubic Ni particles. This method might provide the way not only for

the cubic Ni particles, but also for the spherical Ni particles and other metal particles which are synthesized by reduction of metal chlorides.

Chapter 3. Shape change of fine nickel particles under hydrogen and nickel chloride vapor

1. INTRODUCTION

Ni nanoparticles have received great attention due to their unique optical, magnetic, and catalytic properties.[72] Ni nanoparticles are used as electrode materials for multilayer ceramic capacitor (MLCC), substituting for the precious metal Pd. The recent trend in miniaturization of electronic components requires the MLCCs to be smaller and to have larger capacitance. Hence Ni nanoparticles used as an electrode material become smaller. The shape of the particles is also important. For example, a spherical shape is favored to improve the packing density.[72-74]

Ni nanoparticles are generally synthesized in both liquid and vapor phases. Various methods such as thermal plasma, spray pyrolysis, chemical vapor deposition (CVD), chemical solution reduction, and others have been employed to produce Ni nanoparticles.[32, 33] The liquid phase syntheses have the advantage of producing Ni nanoparticles of uniform size and controlled shape. However, contamination and agglomeration of particles are inevitable in the liquid phase syntheses.[34, 35] Vapor phase syntheses have the advantage of producing non-agglomerated Ni nanoparticles of high crystallinity and purity but have the disadvantage of having difficulty in controlling the morphology and size distribution of particles in the vapor phase. Especially, CVD is a promising method to produce highly crystalline and pure nanoparticles and has an advantage of controlling the particle size and process conditions.[36] The shape of Ni particles has a great effect on magnetic property. For example, a cubic shape was reported to have much higher saturated magnetization than a spherical shape of Ni particles of the similar size.[70, 71]

In our preliminary experiment, Ni particles synthesized by the CVD process had a cubic shape, which is in contrast with the equilibrium crystal shape (ECS) of pure

Ni, which was reported to be nearly spherical with facets of $\{111\}$, $\{100\}$, $\{110\}$ and $\{210\}$ by Hong et al.[47]. There are two possibilities for the evolution of the cubic Ni particles. One is that the cube is the kinetic shape. The other is that the cube is the equilibrium shape under the given processing environment. The explanation of the cube by the kinetic shape is not simple because the cube cannot be explained by classical crystallization kinetics, where individual atoms or molecules are the growth unit. Ni has a face-centered cubic (fcc) crystal structure, for which $\{111\}$ faces has the lowest surface energy and the lowest growth rate. Since the growth shape is enclosed by the faces with the lowest growth rate, the kinetic shape is expected to be a tetrahedron or octahedron. Therefore, to explain the evolution of the cubic shape by growth kinetics, non-classical crystallization, where nanoparticles are the growth unit, should be considered.[49-52, 54, 75] For example, to explain the development of $\{100\}$ facets in the synthetic diamond, Sunagawa[76] suggested that the growth unit should be much larger than an atom.

The other possibility of the cube being an equilibrium shape can be explained if the $\{100\}$ surfaces is stabilized by impurity adsorption. It is well-known that preferential adsorption of impurity reduces surface energies and increases the surface energy anisotropy, causing development of facets different from those of the clean surface.[77] Many cubic metal nanoparticles have been prepared with various surfactants such as cetyltrimethylammonium bromide (CTAB) and polyvinylpyrrolidone (PVP) to reduce surface energies of $\{100\}$ faces in the liquid phase.[78-84] LaGrow et al.[71] prepared cubic Ni nanoparticles by adding surfactants hexadecylamine (HDA) and trioctylphosphine (TOP) in the liquid phase. Even in the gas phase, Gao et al.[70] reported that cubic Ni nanoparticles were prepared in the gas phase due to the adsorption of sodium chloride. Harris[85] reported that spherical Pt nanoparticles changed into cubes under H_2S atmosphere.

Cabié et al.[86] observed reversible shape transformations of Pt nanoparticles by environmental transmission electron microscopy (ETEM) with the increase or decrease of the ratio of (111) to (100) face in H₂ or O₂ respectively.

The purpose of this study is to examine whether the cubic shape of Ni particles synthesized by CVD is the growth or the equilibrium shape. For this, Ni particles were annealed in H₂ or NiCl₂ vapor and their shape change was analyzed.

2. EXPERIMENTAL SECTION

In the CVD synthesis of Ni particles, NiCl₂ is reduced by H₂ to produce Ni as



When N₂ used as a carrier gas was replaced by Ar, the shape of Ni particles did not change. In Eq. (1), NiCl₂, H₂ and HCl are the main gas. Since the production of HCl depends on the reaction between NiCl₂ and H₂, HCl was excluded as a candidate of absorbate.

Experimental procedures are divided into two: one is to examine the effect of H₂ and NiCl₂ vapor on the shape of Ni particles and the other is to examine the effect of the reduction rate of NiCl₂ on the shape of Ni particles. The tube reactor to examine the effect of H₂ and NiCl₂ vapor is a 2-stage horizontal furnace, consisting of a quartz

tube with an inner diameter of 4.5 cm and a length of 120 cm, which is shown in Figure 1(a). N_2 or H_2 was passed through an inlet of the quartz tube at the flow rate of 1000 standard cubic centimeter per minute (sccm). To examine the effect of H_2 atmosphere on the shape of Ni particles, cubic Ni particles of the average size 185 nm prepared by CVD were used as a starting material. These cubic Ni particles were dispersed with ultrasonic vibration on sapphire single crystal substrates (C-plane (0001), Crystal Bank), which is shown in Figure 3 of the Result section. The substrate with dispersed particles was placed in the center of the second heating zone, which is (7) in Figure 1(a), and annealed at 950 °C for 30 min under flowing H_2 .

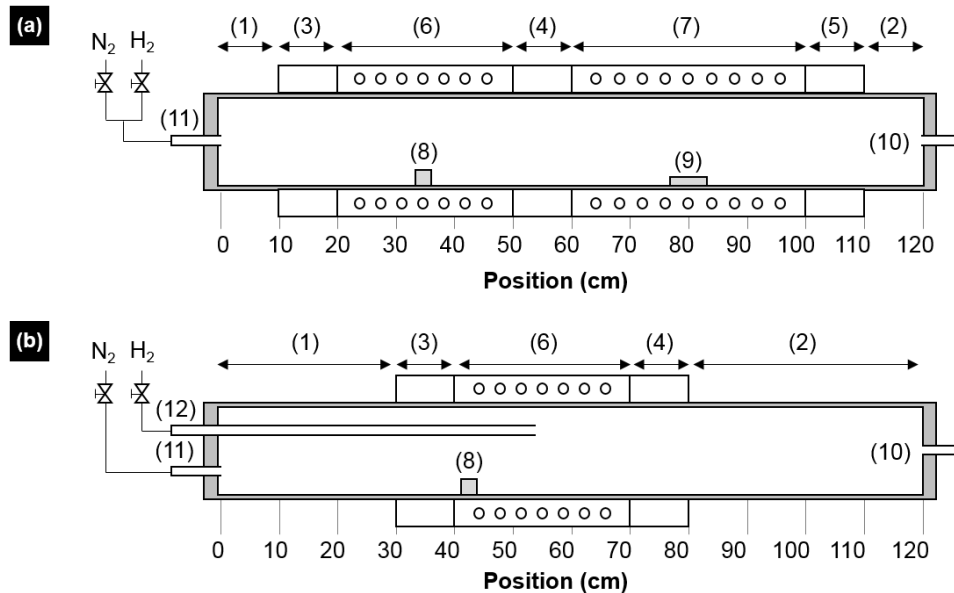


Figure 1. Schematics of (a) the 2-stage horizontal tubular reactor used to anneal Ni particles on the sapphire substrate and (b) the 1-stage horizontal tubular furnace: (1,

2) cold zone, (3-5) insulation, (6, 7) first and second heating zones, (8) crucible, (9) substrate, (10) outlet and (11, 12) inlet of the quartz tube.

To examine the effect of NiCl_2 vapor on the shape of Ni particles, a commercial nickel (II) chloride (NiCl_2) powder (98%, Aldrich) was put in the quartz crucible, which was placed in the center of the first heating zone (8) in Figure 1(a). The Ni particles dispersed on the substrate, which had been annealed previously for 30 min under H_2 atmosphere, were annealed in the center of the second heating zone at 950 °C under NiCl_2 vapor. If NiCl_2 vapor meets with H_2 , NiCl_2 vapor would be reduced and produce Ni particles. To prevent this reduction of NiCl_2 , H_2 was switched to N_2 and purged for 30 min before annealing under NiCl_2 vapor. Three temperatures of 750, 800, and 850 °C were used for the first heating zone to control the vapor pressure of NiCl_2 that rises exponentially with increasing temperature.[87, 88] The annealing time was varied at 0, 15, 45, and 75 min. The annealed Ni particles on the sapphire substrate were observed by field-emission scanning electron microscope (FESEM, MERLIN Compact, Zeiss). The reason why FESEM (SU-70, Hitachi), which was used for observation in the next experiment, was not used to observe Ni particles on the sapphire substrate is because of electric charging. In order to estimate the relative surface energy for each face of Ni particles from FESEM observations, the Wulffman software[89] was used.

To examine the effect of the reduction rate of NiCl_2 on the shape of Ni particles, the experiments were carried out in the 1-stage horizontal furnace as shown in Figure 1. N_2 and H_2 were passed through (11) and (12) in Figure 1(b), the inlets of the quartz tube respectively at the flow rates of 900 and 300 sccm. The furnace temperature was increased to 950 °C, at which the evaporation temperature was approximately

900 °C. The carrier gas N₂ containing NiCl₂ vapor was mixed with H₂ in the middle of the heating zone (6) in Figure 1(b). Under this condition, Ni particles were generated in the gas phase and could be collected for 30 min by the filter connected to the outlet. Since the reduction rate of NiCl₂ depends on the location where N₂ containing NiCl₂ vapor was mixed with H₂, it could be controlled by adjusting the location. For this, the position of the H₂ inlet (12) in Figure 1(b) was made to move and varied at 55, 62.5, 70, and 75 cm, which are shown in Figure 1(b). The collected Ni particles were characterized by FESEM (SU-70, Hitachi), transmission electron microscope (TEM, JEM-2100F, JEOL), and X-ray diffraction (XRD, D8 Advance, Bruker).

3. RESULTS AND DISCUSSION

3.1. The effect of NiCl₂ vapor on the shape of Ni particles

Figure 2 shows the FESEM images of Ni particles of ~ 185 nm prepared by CVD. These are an initial shape of Ni particles on the sapphire substrate before annealing under H₂ atmosphere. All Ni particles have a cubic shape.

The specimen shown in Figure 2 was annealed under flowing H₂ for 30 min at 950 °C. The evolved shape of Ni particles is shown in Figure 3. Clearly the shape of Ni particles was changed from a cube to a faceted but almost sphere. Some Ni particles in Figure 3(b) show a shape deviating somewhat from a sphere. For

example, some have an ellipsoidal shape. The almost spherical particle in Figure 3(a) appears to be an equilibrium shape. Ni particles deviating from a sphere in Figure 3(b) appear to be on their way to an equilibrium shape. This means that the annealing time was not sufficiently long or the annealing temperature was not sufficiently high to reach the equilibrium shape. However, it is for sure that H₂ atmosphere should destabilize the (100) surface and be responsible for the shape change from a cube to a sphere.

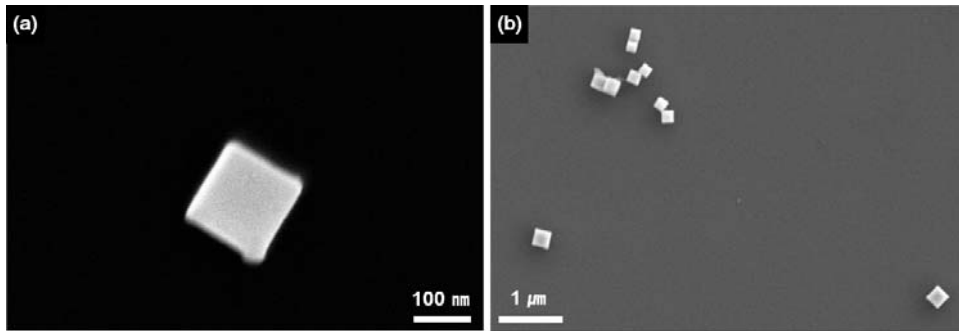


Figure 2. FESEM images of dispersed cubic Ni particles on a sapphire substrate: (a) higher and (b) lower magnifications.

Using the Wulffman software[89], the numerical value for the energy on each facet could be input by trial-and-error to reproduce the shape of the Ni particle in Figure 3(a). By this scheme, the software-generated equilibrium crystal shape (ECS) could be obtained for Ni particles annealed in H₂ as shown in Figure 4(a). The developed facets in Figure 4(a) are {100}, {111}, and {210}. The ECS corresponds to the surface energy ratios of $\gamma_{100}/\gamma_{111} = 1.05$ and $\gamma_{210}/\gamma_{111} = 1.01$, where the subscripts 100, 111 and 210 represent the miller indices. It should be noted that since {110} faces

were not observed, $\gamma_{110}/\gamma_{111}$ should be larger than 1.065. Consequently, It can be deduced that the relative magnitude of surface energies are $\gamma_{111} < \gamma_{210} < \gamma_{100} < \gamma_{110}$.

Figure 5 shows the FESEM images of Ni particles annealed at 950 °C under NiCl₂ atmosphere. Figure 5(a) shows spherical Ni particles obtained by annealing in H₂ atmosphere, which were changed to Figure 5(b)-(d) after annealing respectively for 15, 45 and 75 min under NiCl₂ atmosphere. Figure 5(b) shows that Ni particles were changed to a cuboctahedral shape after being annealed for 15 min under NiCl₂ atmosphere. The software-generated ECS for the experimentally observed Ni particle in Figure 5(b) is shown in Figure 4(b), which shows that {100} and {111} facets are developed. The surface energy ratio is estimated as $\gamma_{100}/\gamma_{111} = 1.00$. The relative magnitude of surface energies can also be estimated as $\gamma_{100} = \gamma_{111} < \gamma_{110}$.

Figure 5(c) shows Ni particles annealed at 950 °C for 45 min under NiCl₂ atmosphere. Ni particles smaller than 600 nm in Figure 5(c) were changed into a cubic shape. However, Ni particles larger than 600 nm maintained a non-cubic shape, which would be attributed to the slower kinetics of larger particles.

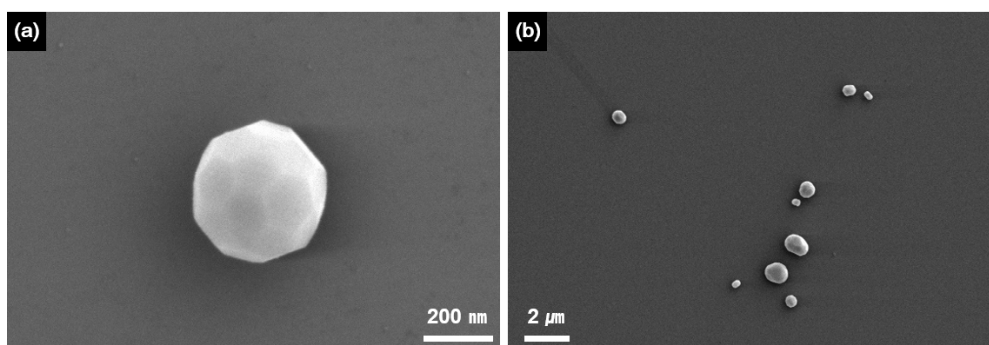


Figure 3. FESEM images of Ni particles annealed for 30 min at 950 °C in the H₂ atmosphere: (a) higher and (b) lower magnifications.

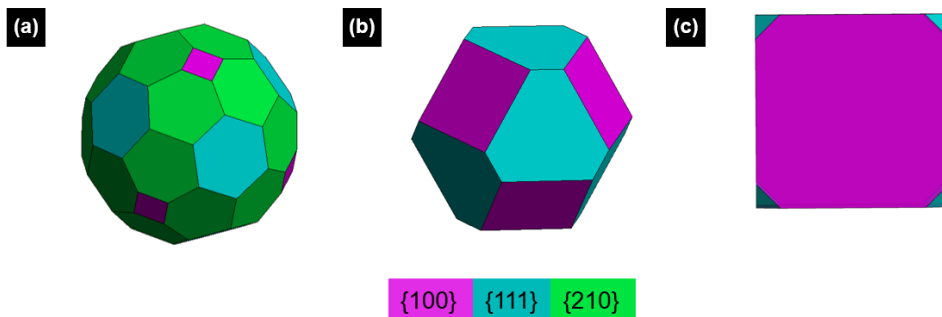


Figure 4. Software-generated ECS for the experimentally observed Ni particles shown in Figures 3, Figure 5b, and Figure 5c(or 5d) correspond to (a), (b), and (c) respectively.

Figure 5(d) shows that all Ni particles observed changed into a cubic shape after being annealed for 75 min under NiCl₂ atmosphere. The software-generated ECS for experimentally observed Ni particles in Figure 5(d) is presented in Figure 4(c). {100} and {111} facets are developed. The surface energy ratio is estimated to be $\gamma_{100}/\gamma_{111} = 0.63$. This gives the inequalities of the surface energies as $\gamma_{100} < \gamma_{111} < \gamma_{110}$. Consequently, the surface energy ratio (100) to (111) surface becomes 1.05, 1.0, and 0.63 after annealing respectively for 0, 15, and 75 min under NiCl₂ atmosphere. It should be noted that the surface energy was reversed from (100) to (111) after annealing for 15 min under NiCl₂ atmosphere. This means that NiCl₂ vapor stabilizes {100} surfaces of Ni particles. The stabilization of {100} surfaces appears to be due to the adsorption of NiCl₂ molecules preferentially on {100} surfaces.

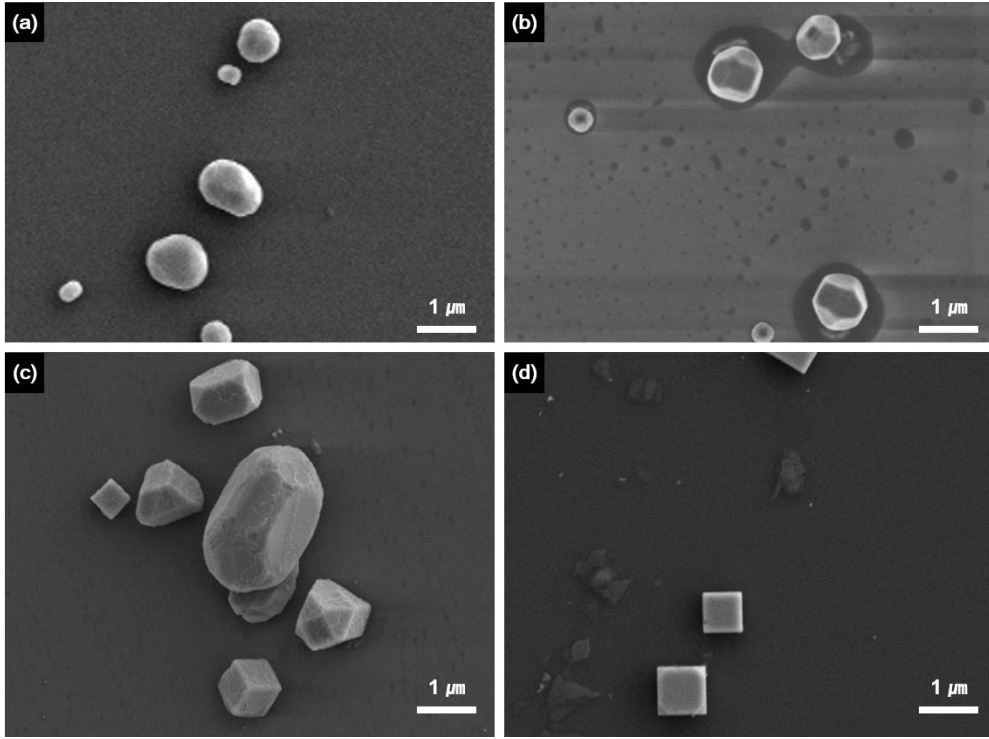


Figure 5. FESEM images of Ni particles annealed for (a) 0, (b) 15, (c) 45, or (d) 75 min at 950 °C under NiCl₂ atmosphere.

Adsorption is described by many isotherms.[90] The Langmuir adsorption isotherm, which is one of the simplest and the most direct model, is described as

$$K_{eq} = \frac{k_{ad}}{k_d} = \frac{\theta_A}{(1-\theta_A)P_A} \quad \text{or} \quad \theta_A = \frac{K_{eq}P_A}{1+K_{eq}P_A} \quad (2)$$

where θ_A is the fraction of the adsorption sites occupied, P_A is the partial pressure of adsorbate over the surface, k_{ad} and k_d represent the kinetic rate constants of

adsorption and desorption respectively. If Eq. (2) is applied to the adsorption of NiCl_2 , the fraction of the surface sites covered with NiCl_2 would increase with the partial pressure of NiCl_2 . This means that the partial pressure of NiCl_2 would affect the degree of $\{100\}$ stabilization. In other words, if the partial pressure of NiCl_2 is not high enough, the $\{100\}$ surface might not be stabilized sufficiently to produce a cube.

This possibility was tested by examining the effect of the partial pressure of NiCl_2 on the shape of Ni particles. Spherical Ni particles were annealed at $950\text{ }^\circ\text{C}$ for 45 min with varying evaporation temperature. Figure 6(a) shows the FESEM image of Ni particles annealed at $950\text{ }^\circ\text{C}$ for 45 min under H_2 atmosphere, which will be a reference for the shape change of Ni particles annealed additionally for 45 min at evaporation temperatures, 750, 800 and $850\text{ }^\circ\text{C}$ of NiCl_2 respectively shown in Figures 6(b), (c) and (d).

Even after additional annealing for 45 min in H_2 atmosphere, ellipsoidal particles are still observed in Figures 6(a). However, ellipsoidal particles were evolved from the initial cubic particles, it is evident that H_2 does not stabilize $\{100\}$ and induces an equilibrium shape to be nearly spherical.

Figure 6(b) shows the FESEM image of Ni particles after being annealed for 45 min at the evaporation temperature of $750\text{ }^\circ\text{C}$. Most particles are still spherical and the shapes did not change much from those of Figure 6(a). Maintenance of spherical shapes is attributed to the low vapor pressure of NiCl_2 , which might affect the shape change both thermodynamically and kinetically. Figure 6(c) shows Ni particles annealed for 45 min at the evaporation temperature of $800\text{ }^\circ\text{C}$. Some of particles changed into a shape approaching a truncated cube, indicating that $\{100\}$ facets were developed. This shape change is attributed to the little high vapor pressure of NiCl_2 .

Figure 6(d) shows Ni particles annealed for 45 min at the evaporation temperature at the evaporation temperature of 850 °C. Ni particles smaller than 500 nm changed to a cubic shape, which is an ECS under NiCl₂ atmosphere. The dominance of {100} surfaces indicates that the kinetics for the change to the cubic shape is high, which is attributed to the high vapor pressure of NiCl₂. Figures 6(b)-(d) indicate that thermodynamics and kinetics for the shape change of Ni particles depend on the vapor pressure of NiCl₂.

Considering that NiCl₂ vapor stabilizes {100} faces of Ni, if the polycrystalline Ni sheet is annealed under NiCl₂ atmosphere, the sheet is expected to have a cube texture with {100} faces. As another application, the synthesis of cubic and spherical Ni particles could be controlled systematically.

According to the analysis on the effect of the vapor pressure of NiCl₂ on the shape change, Ni particles with developed {100} such as a cube would be synthesized under the CVD condition where the vapor pressure of NiCl₂ is high and the fraction of the adsorption sites occupied by NiCl₂ is high. And nearly spherical particles would be synthesized under the CVD condition where the vapor pressure of NiCl₂ is low and the fraction of the adsorption sites occupied by NiCl₂ is low.

The CVD condition of high NiCl₂ vapor pressure can be realized by decreasing the reduction rate of NiCl₂ vapor by H₂. In this condition, the amount of Ni particles produced is small. At the same time the vapor pressure of NiCl₂ is high and the fraction of the adsorption sites occupied by NiCl₂ is high. Then, the cubic shape would be favored. The CVD condition of low NiCl₂ vapor pressure can be realized by decreasing the reduction rate of NiCl₂ vapor by H₂. In this condition, the amount of Ni particles produced is small. At the same time the vapor pressure of NiCl₂ is

high and the fraction of the adsorption sites occupied by NiCl_2 is low. Then, the nearly spherical shape would be favored.

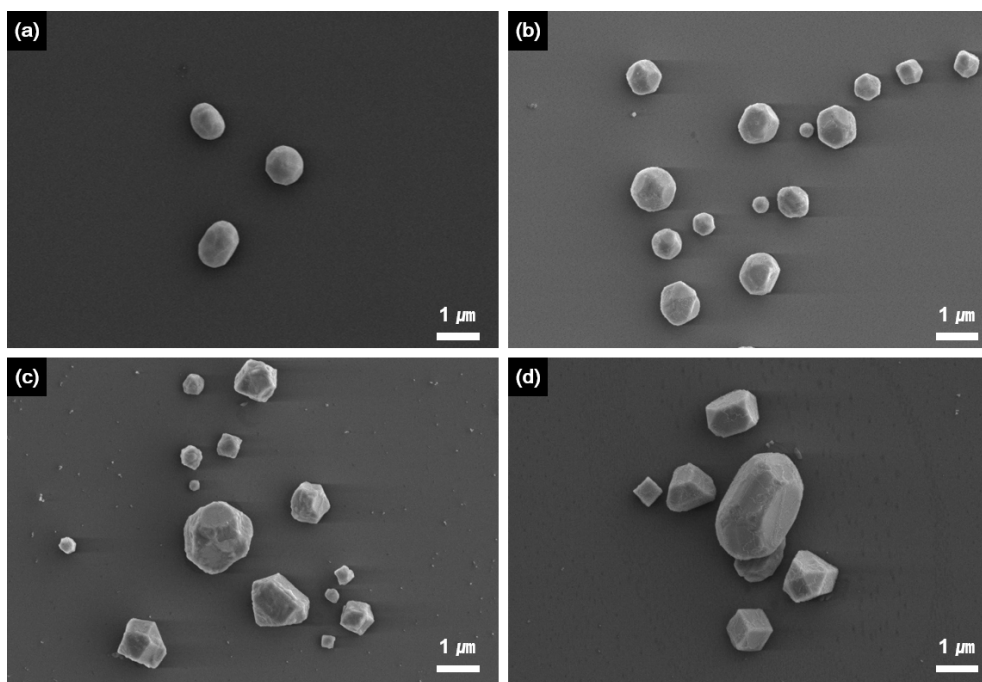


Figure 6. FESEM images of (a) Ni particles annealed at 950 °C for 45 min in H_2 atmosphere and Ni particles annealed at 950 °C in NiCl_2 atmosphere under various NiCl_2 evaporation temperatures of (b) 750, (c) 800, and (d) 850 °C.

This possibility was tested by decreasing or increasing the reduction rate of NiCl_2 vapor during the synthesis of Ni particles by CVD. In order to control the reduction rate, the position of H_2 inlet, which is (12) in Figure 1(b), was adjusted. Four positions were chosen with (a) 55, (b) 62.5, (c) 70 and (d) 75 cm away from the left end of the reactor tube, the distance of which is shown in Figure 1(b). It should be

noted that the position of H₂ inlet does not coincide with the reduction zone or the region where NiCl₂ vapor begins to mix with H₂. By experience, we noticed that the reduction zone is revealed indirectly by the metallic colored Ni film deposited on the inner wall of the tube reactor, which can be examined after the CVD process. The position of Ni film deposition is shifted roughly 10 cm to the left of the position of H₂ inlet. This shift would be attributed to the diffusion of H₂ before their reaction with NiCl₂.

3.2. The effect of the reduction rate of NiCl₂ on the shape of Ni particles during CVD

For the synthesis of Ni particles by CVD, N₂ and H₂ were supplied through the inlets of the quartz tube respectively at the flow rates of 900 and 300 sccm. The hot zone of the furnace was at 950 °C, at which the evaporation temperature was approximately 900 °C. Under this condition, Ni particles were generated in the gas phase. These particles were collected for 30 min by the filter.

Figure 7(a)-(d) shows the FESEM images of collected Ni particles synthesized for H₂ inlet positions of 55, 62.5, 70, or 75 cm respectively. Figure 7(a) shows that most Ni particles are cubic with relatively wide size distribution without any noticeable aggregation. In contrast, Figure 7(b) shows that most Ni particles are non-cubic and aggregated. Figure 7(c) shows also that most Ni particles are non-cubic and aggregated. Figure 7(d) shows that Ni particles have various shapes such as cube, sphere, and cuboctahedron with some aggregation of spherical particles.

Considering that Ni has an fcc lattice, which has the lowest surface energy on {111}, the evolution of the cubic shape in Figure 7(a) and (d) is somewhat puzzling. Since cube-shaped particles might have a composition or crystal structure different from that of spherical particles, samples of Figure 7(a)-(d) were analyzed by XRD and especially a cube in Figure 7(a) was observed by TEM.

The peaks in Figure 7(e) were at 2θ of 44.5, 51.8, and 76.4°, which coincide respectively with the 2θ values of JCPDS no. 04-0850 for Miller indices (111), (200), and (222) of fcc Ni. Since other peaks were not observed in Figure 7(e), all particles in Figure 7(a)-(d) appear to be pure crystalline Ni.

For TEM observation of cubes in Figure 7(a), cubic particles were dispersed in deionized water and the liquid was dropped on a holey carbon membrane on the copper grid. Figure 7(f) shows the TEM image for one of cubes on a holey carbon membrane. The diffraction pattern of the cube in the inset matched the reflection of {200} faces of single-crystalline Ni, confirming that the cubic particle is pure single-crystalline Ni.

Figure 7(a)-(d) shows that the shape of Ni particles depends on the position of H₂ inlet, which can be an important process parameter to control the particle shape. As mentioned earlier, the reduction zone is shifted ~10 cm left from the H₂ inlet position. Therefore, four positions of H₂ inlet produce four corresponding reduction zones as shown in Figure 8, which shows the temperature distribution of the reactor and the reduction zone for various H₂ inlet positions. The hot zone, where the temperature is uniform, is only half the length of the heating zone. Away from the hot zone, the temperature drops steeply as shown in Figure 8.

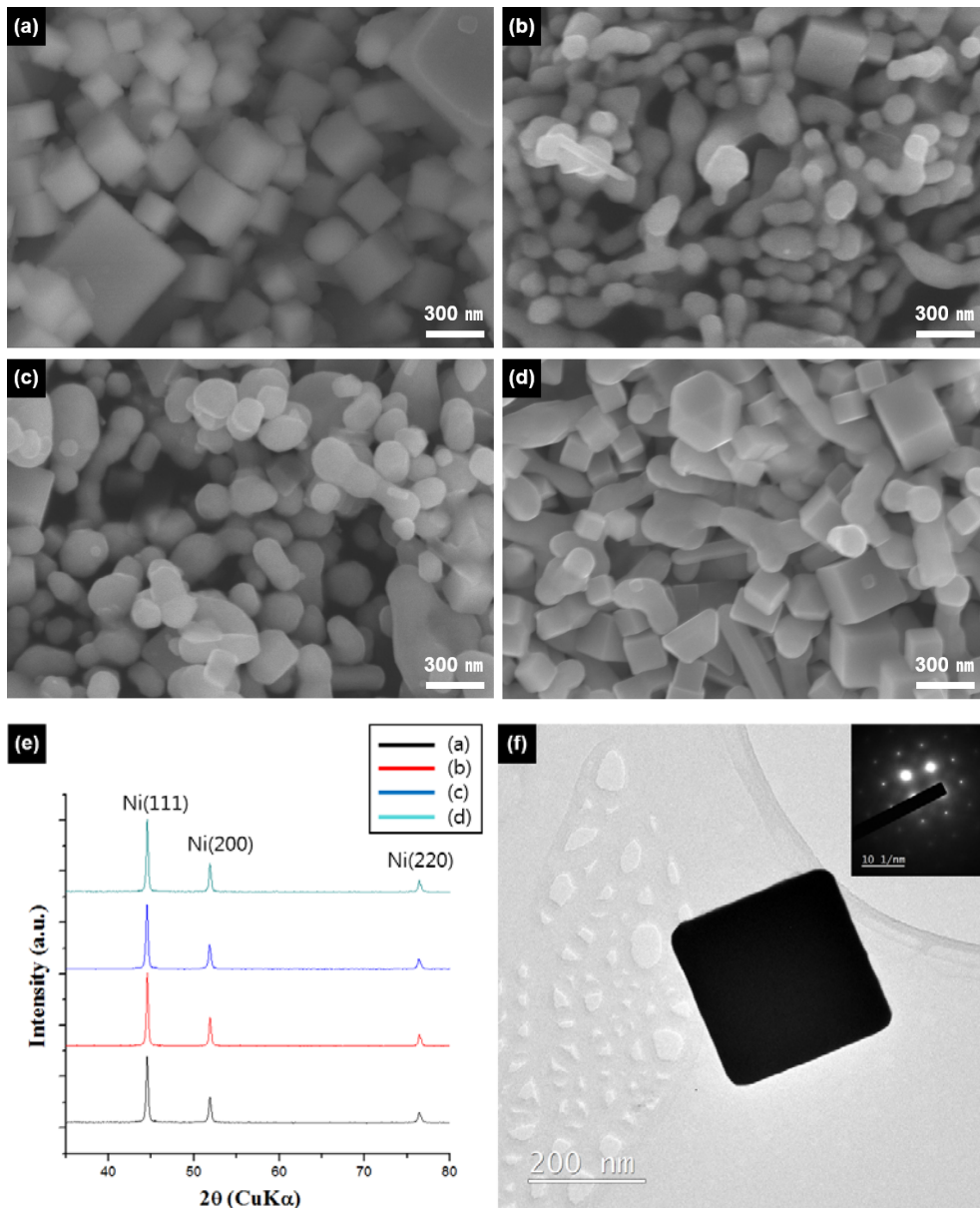


Figure 7. SEM image of collected Ni particles synthesized under various H₂ inlet position of (A) 55, (B) 62.5, (C) 70, or (D) 75 cm. (E) XRD pattern of samples (A-D). (F) TEM images of cubic Ni particle of sample (A).

H₂ inlet positions of 55, 62.5, 70, and 75 cm correspond respectively to reduction zones (a), (b), (c) and (d) of Figure 8. The temperature of the reduction zones (b) and (c) is 950 °C. However, the temperatures of the reduction zones (a) and (d) are much less than 950 °C because the temperature gradient is steep. Since the reduction rate depends exponentially on the temperature, it would be high in the reduction zones (b) and (c) but low in the reduction zones (a) and (d). It should be noted that reduction zones (a) and (d), which have a low reduction rate, should be longer than reduction zones (b) and (c). Therefore, adjusting the H₂ inlet position could be an alternative way to control the reduction temperature.

The result of Figure 7, where the high and low reduction rates produced respectively spherical and cubic particles, agrees with the result of Figure 6, where the low and high evaporation temperatures produced respectively spherical and cubic particles.

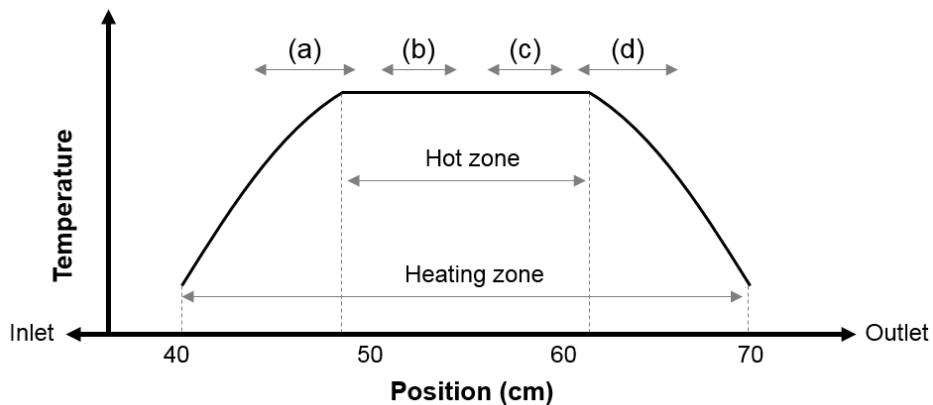


Figure 8. Schematic of temperature distribution and reduction zone in a reactor at H₂ inlet position of (a) 55, (b) 62.5, (c) 70, and (d) 75 cm.

On the other hand, particles synthesized from the gas phase tend to be aggregated when no special efforts are made.[41] Figure 7 shows that spherical particles tend to aggregate but cubic particles don't. It should be noted that the particles in Figure 7(a) have the longest residence time in the reactor but the particles did not aggregate. One possibility for the non-aggregation of cubic particles would be the adsorption of NiCl_2 on the surface.

Furthermore, the effect of H_2 flow rate is confirmed when H_2 inlet position is fixed at the center of the hot zone. Figure 9 shows the temperature distribution reaction zone in a reactor under various H_2 flow rate. When the concentration of H_2 is increased in this reaction, it can be predicted that reaction rate will be increased by using Le Châtelier's principle.

Hence, when H_2 flow rate is 500 sccm, reaction will occur in reaction zone (A) in Figure 9. Also, when H_2 flow rate is 300 and 50 sccm, reaction will occur in reaction zone (B) and (C) in Figure 9, respectively. In reaction zone (A) H_2 flow rate is higher than in reaction zone (B), but the average temperature is lower than in reaction zone (B). For this reason, the reaction rate in reaction zone (A) should be slower than one in reaction zone (B). Furthermore, the length of reaction zone (A) should be wider than the length of reaction zone (B). In the case of reaction zone (C), H_2 flow rate and the average temperature are lower than ones in reaction zone (B). Therefore, the length of reaction zone (C) should be wider than the length of reaction zone (B).

Figure 10 shows the SEM images of collected Ni nanoparticles generated under various H_2 flow rate. In reaction zone (A), various shaped Ni nanoparticles are observed and their size distribution is wide. In reaction zone (B), only spherical Ni nanoparticles are observed, and their distribution of size is narrower than one in reaction zone (A). In reaction zone (C), various shaped Ni nanoparticles are observed

and their size distribution is wide. This result can be explained by La Mer model shown in Figure 11.

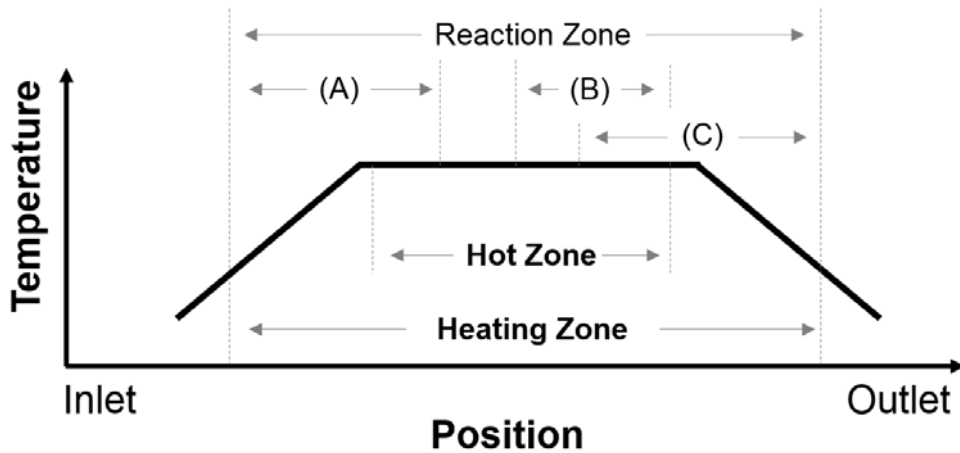


Figure 9. Temperature distribution and reaction zone in a reactor generated under various H_2 flow rates ((A) 500 sccm (B) 300 sccm (C) 50 sccm).

According to La Mer model, the size distribution of nanoparticles is determined by nucleation period. Hence, polydisperse and various shaped Ni nanoparticles are observed in reaction zone (A) and (C) due to a low nucleation rate. On the contrary, monodisperse and spherical Ni nanoparticles are observed in reaction zone (B) due to a high nucleation rate. This result indicates that reaction rate should affect not only the size distribution but also the shape of Ni nanoparticles.

On the other hand, the effect of hydrogen inlet position on the molar concentration of H_2 in a reactor is calculated by commercial CFD code (ANSYS Fluent v16.0) as shown in Figure 12. The main purpose of this simulation was to understand the diffusion of hydrogen under various inlet position, the reaction was not considered.

According to this result, hydrogen can diffuse to inlet direction although it is reverse direction to the flow.

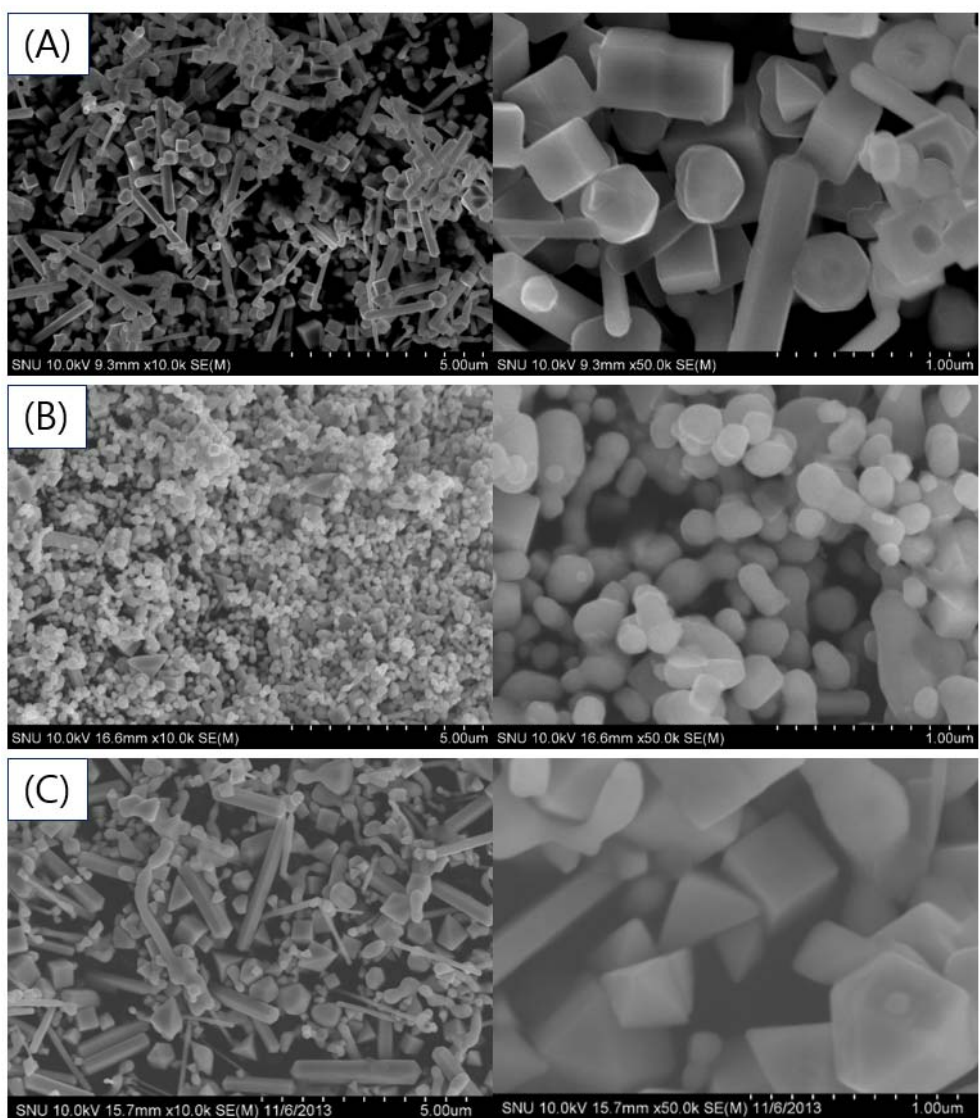


Figure 10. SEM images of collected Ni nanoparticles generated under various H₂ flow rates ((A) 500 sccm (B) 300 sccm (C) 50 sccm).

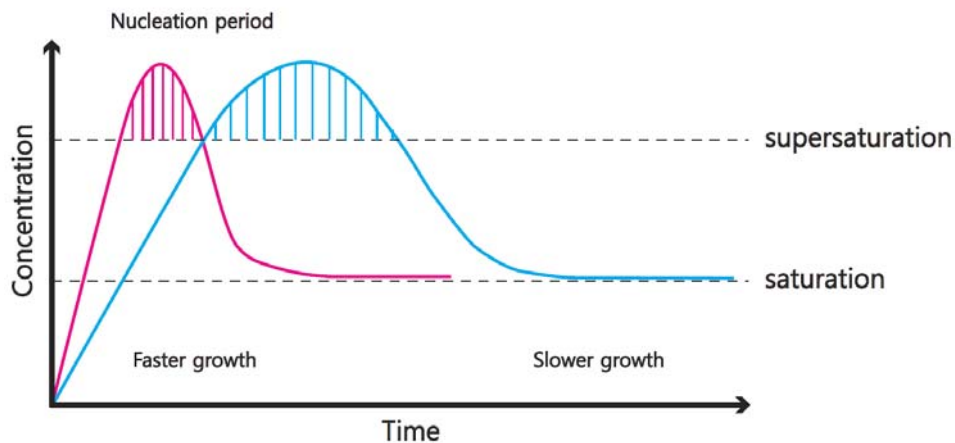


Figure 11. La Mer model.

4. CONCLUSIONS

By examining the shape change of Ni particles during annealing under H_2 and $NiCl_2$ atmospheres, it was confirmed that H_2 and $NiCl_2$ vapor favor respectively spherical and cubic shapes, which indicates that $NiCl_2$ stabilizes the $\{100\}$ faces of Ni. Using this fact, suitable synthetic conditions for cubic and spherical Ni particles could be derived. A similar concept can be applied to the syntheses of cubic and spherical Fe and Co particles, which is under study.

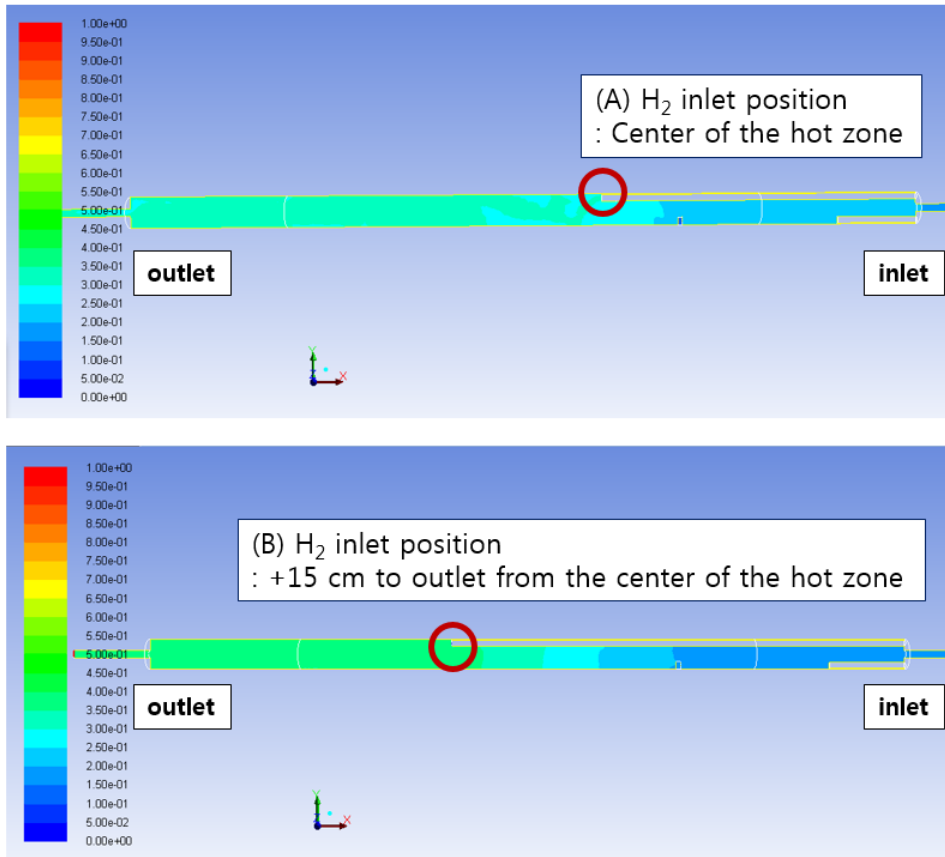


Figure 12. Diffusion behavior of H₂ depending on the H₂ inlet positions.

Chapter 4. Gas-phase synthesis of monodisperse nickel nanoparticles

1. Introduction

With trend of integration and miniaturization, MLCC should be smaller and capacitance of MLCC should be increased. These aims can be achieved by increasing the number of stacking layers of BaTiO₃ dielectric layers and Ni electrode layers. Therefore, the proportion of internal electrode materials is also increased. Hence, the increasing of internal metal electrode had led to the replacement of expensive noble metals by cheap nickel as an electrode material to decrease cost [28]. Meanwhile the number of stacked layers is increased in a small volume, nickel particles used as internal electrode layers should be small, narrow size distributed, non-agglomerated, spherical shaped, high purity, and high crystalline [91-93]. Fine nickel metal powder of uniform morphology, narrow size distribution, and high purity was prepared from high purity metal solution [28, 93].

The properties of nanoparticles are very size dependent. Hence, the size distribution of nanoparticles should be narrow to utilize these unique properties of nanoparticles. Therefore, the synthesis of so-called monodisperse nanoparticles with uniform size and uniform internal structure (generally less than 10% in coefficient of variation = standard deviation / mean size) has been intensively studied by many research groups. Park et al. successfully synthesized monodisperse nanoparticles with a regular shape. These particles are prepared by burst of nucleation to enable separation of nucleation and growth stages during liquid phase process [43, 44].

Meanwhile, the aggregates are often observed during a gas phase synthesis of particles. In the gas phase, particles tend to collide each other due to Brownian coagulation, and form the agglomerates. These agglomerates could change to aggregates due to the sintering of them. The formation of aggregates affects the

quality of synthesized particles. For this reason many researches have been done about the agglomeration and aggregation for the past decades.

The degree of polydispersity and agglomeration is a typical characteristic of particles made by gas-phase process. Loosely attached particles (so-called primary particles) by physical forces such as van der Waals and electrostatic force without any necking between primary particles constitute soft-agglomerates or just agglomerates. Agglomerate can be easily dispersed into liquid medium, and broken into individual primary particles by applying an appropriate energy such as ultrasonic. When primary particles form necks between them by chemical/sinter forces (metallic, ionic, or covalent bonds), these are termed hard-agglomerates or aggregates. Aggregates are difficult to break into individual primary particles. Aggregates are particularly attractive for sensors and electro-ceramics because their necks form long crystal planes that minimize contact resistance as well as facilitate electron flow and strong sensor signals [45]. However, an aggregated mass of nanoparticles is of little benefit during densification because grain growth prevails over sintering. Also, aggregation generally eliminates the benefits of a narrow particle size distribution [46]. In this research, to avoid the aggregation and to narrow the size distribution of particles, an improved vertical reactor was proposed and studied.

2. Experimental procedure

2-1. Reactor conditions and CFD analysis

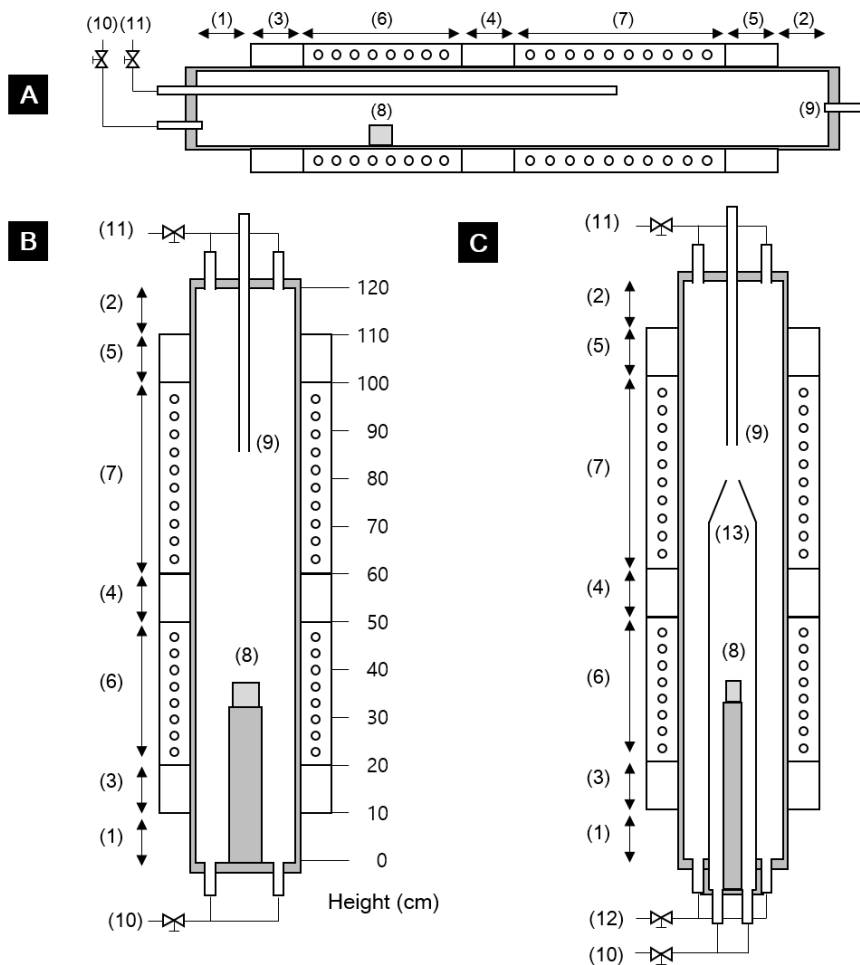


Figure 1. Schematic of reactor conditions ((A) Horizontal reactor: hydrogen is injected to the middle of the reaction zone through a quartz tube. (B) Vertical reactor: hydrogen is injected to the top of the reactor and outlet is placed at the middle of second heating zone, (C) Improved vertical reactor: hydrogen is injected to both ends of the reactor, outlet is placed at the middle of second heating zone, and the additional inner tube is placed, (1,2) Cooling zone, (3-5) Insulator, (6) first Heating zone, (7) second Heating zone, (8) NiCl₂ in crucible, (9) Outlet, (10) N₂ inlet, (11,12) H₂ inlet, (13) Inner tube).

Figure 1 shows the schematic of various reactor conditions examined in this study. Figure 1A shows a typical horizontal reactor condition. H_2 was injected to the middle of the reaction zone through a quartz tube. N_2 was injected to the left of the reactor and the outlet was placed at the right of the reactor. Figure 1B shows a vertical reactor condition. The same reactor with a horizontal reactor condition, was used but it was vertically placed. H_2 was injected to the top of the reactor. N_2 was injected to the bottom of the reactor and the outlet was placed at the middle of the reaction zone. Figure 1C shows an improved vertical reactor. The only difference between Figure 1B and C is the presence of the inner tube to isolate the $NiCl_2$ vapor.

The temperature distribution for a horizontal reactor and a vertical reactor and particle trajectory for a vertical reactor are analyzed by a commercial CFD code (ANSYS Fluent v16.0). The flow direction in a horizontally placed reactor is vertical to the gravity, so that the buoyancy effect is expected. On the contrary, the flow direction in a vertically placed reactor is horizontal to the gravity. Hence, for a horizontal reactor, a half-cylindrical 3D model was used, so that the gravity could be taken into account by the buoyancy effect. This study is focused in the behavior of particles in a reactor. Therefore, first heating zone and an injection of H_2 in a horizontal reactor were not considered to simplify the calculation. For a vertical reactor, an axisymmetric 2D model was used and first heating zone was not considered for the same reason.

In the calculation, gases were assumed to be ideal and incompressible. The temperature-dependent density of gases was considered to determine the buoyancy effect. The wall boundary conditions represent the inner surface of tube wall, so that the heat conduction through tube wall was not considered. Insulator placed between

cooling and heating zone was assumed to be perfect thermal insulator. The boundary conditions for both horizontal and vertical reactor are summarized in Table 1.

Table 1. Boundary conditions for CFD analysis.

| Reactor | Type | Boundary | Value | |
|------------|-----------------|--------------|-------|------------------|
| Horizontal | Wall | Cooling zone | 300 | K |
| | | Insulator | 0 | W/m ² |
| | | Heating zone | 1300 | K |
| | Velocity inlet | Nitrogen | 1.2 | m/s |
| | Pressure outlet | Outlet | 0 | Pa |
| Vertical | Wall | Cooling zone | 300 | K |
| | | Insulator | 0 | w/m ² |
| | | Heating zone | 1300 | K |
| | Velocity inlet | Nitrogen | 1.2 | m/s |
| | | Hydrogen | 0.13 | m/s |
| | Pressure outlet | Outlet | 0 | Pa |

2-2. Comparison between horizontal and vertical reactor

The experiments were carried out in tubular furnace under atmospheric pressure. A quartz reactor whose length is 120 cm and inner diameter is 4.5 cm was used for all conditions. There are two heating zones in the furnace. A commercial nickel (II)

chloride (NiCl_2) powder (98%, Aldrich) used as a precursor was placed in the center of the first heating zone (evaporation zone) whose length is 30 cm. Carrier gas (N_2) containing NiCl_2 vapor and H_2 used as a reduction gas are mixed with each other in the middle of the second heating zone (reaction zone) whose length is 40 cm. Ni nanoparticles generated by the gas phase reaction were collected by the filter at the outlet of the reactor. The particle collection was done for 30 min under the reaction temperature of $950\text{ }^\circ\text{C}$, the evaporation temperature of $850\text{ }^\circ\text{C}$, H_2 flow rate of 100 sccm and the N_2 flow rate of 500 sccm.

2-3. Effect of the temperature of second heating zone

To examine the effect of the second heating zone, a vertical reactor shown in Figure 1B was used. The temperature of the first heating zone was maintained as $850\text{ }^\circ\text{C}$, and the temperature of the second heating zone was varied at 950, 1050, or $1100\text{ }^\circ\text{C}$. The outlet was placed at 80 cm and the NiCl_2 was placed in crucible at 35 cm. The particle collection was done for 30 min under H_2 flow rate of 125 sccm and the N_2 flow rate of 500 sccm.

2-4. Effect of the outlet position

To examine the effect of the outlet position, a vertical reactor shown in Figure 1B was used. The outlet position was varied at 70, 80, or 90 cm. The temperatures of the first heating zone and the second heating zone were maintained as 850 and $1050\text{ }^\circ\text{C}$ respectively. The NiCl_2 was placed in crucible at 35 cm. The particle

collection was done for 30 min under H₂ flow rate of 125 sccm and the N₂ flow rate of 500 sccm.

2-5. Effect of the temperature of first heating zone

To examine the effect of the first heating zone, a vertical reactor shown in Figure 1B was used. The temperature of the second heating zone was maintained as 950 °C, and the temperature of the first heating zone was varied at 750, 800, 850, or 900 °C. The outlet was placed at 80 cm and the NiCl₂ was placed in crucible at 35 cm. The particle collection was done for 30 min under H₂ flow rate of 125 sccm and the N₂ flow rate of 500 sccm.

2-6. Effect of the precursor position

To examine the effect of the distance between position of precursor and reaction zone, a vertical reactor shown in Figure 1B was used. The position of NiCl₂ in a crucible was varied at 27, 31, 35, or 43cm. The temperatures of the first heating zone and the second heating zone were maintained as 850 and 1000 °C respectively. The outlet was placed at 80 cm. The particle collection was done for 30 min under H₂ flow rate of 125 sccm and the N₂ flow rate of 500 sccm.

2-7. Effect of the volume ratio

To examine the effect of the volume ratio of upper part where H_2 passes through to lower part where $NiCl_2$ and N_2 pass through, a vertical reactor shown in Figure 1B was used. The length of a quartz reactor was varied at 120 or 130 cm. Only the length of the cooling zone marked as (2) in Figure 1B was increased. The temperatures of the first heating zone and the second heating zone were maintained as 850 and 1050 °C respectively. The outlet was placed at 80 cm and the $NiCl_2$ was placed in crucible at 35 cm. The particle collection was done for 30 min under H_2 flow rate of 125 sccm and the N_2 flow rate of 500 sccm.

2-8. Improvement of vertical reactor

As shown in Figure 1C, to improve a vertical reactor, the inner tube for an isolating of $NiCl_2$ vapor, was inserted to a vertical reactor shown in Figure 1B.

3. Result and discussion

3-1. Comparison between horizontal and vertical reactor

Figure 2B shows the typical temperature distribution of a horizontal tubular reactor. Around the insulating zone placed between the heating and cooling zone, temperature drops sharply. In this region, the hot and cold gases should coexist. The hot gas having lower density than the cold gas tends to float due to the buoyancy.

The hot gas will be cooled by cold wall, and then it will tend to sink. Hence the gas flow will circulate as shown in Figure 2A. The tendency of gas flow to circulate increases a mean residence time and widens a residence time distribution of nanoparticles. The increase of a mean residence time increases the chance of Brownian coagulation and a thermal energy is high enough to cause sintering of the agglomerates in a typical gas phase process. Consequently the temperature gradient of this region will cause a poor quality of nanoparticles. Therefore an additional effort should be made to avoid the formation of aggregates.

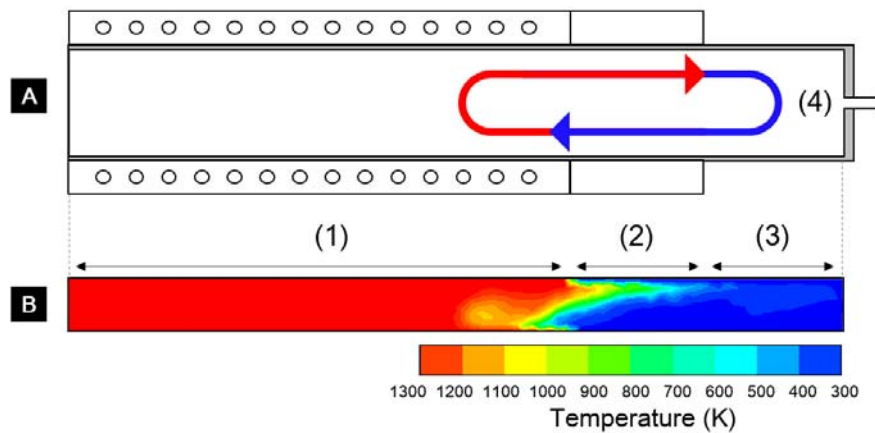


Figure 2. CFD analysis for a horizontally placed tubular reactor shows the temperature distribution on a symmetric plane ((A) Schematic of reactor, (B) Contours of Temperature, (1) second Heating zone, (2) Insulating zone, (3) Cooling zone, (4) Outlet).

Figure 3 shows a schematic of a temperature distribution during the gas phase synthesis of particles. To simplify the concept, it is assumed that particles are

monodisperse and the size of agglomerates and aggregates is uniform. When the temperature is over T_1 , primary particles easily collide each other and agglomerates will be formed. When the temperature is over T_2 , the sintering of agglomerates will occur and aggregations will be formed. When the temperature is over T_3 , the coalescence of aggregates or agglomerates will occur and larger particles than primary particles will be formed. For the typical temperature distribution, temperature drops sharply around the insulating zone placed between the heating and cooling zone. Therefore a wide size distribution of particles and the formation of aggregates should be caused in this region. For the ideal temperature distribution, the temperature gradient is extremely steep at the end of the hot zone to avoid the formation of aggregates. It is impossible to obtain the extremely steep temperature gradient in reality. Instead, if the residence time of particles in the region where temperature is over T_2 is reduced, the formation of aggregates will be suppressed.

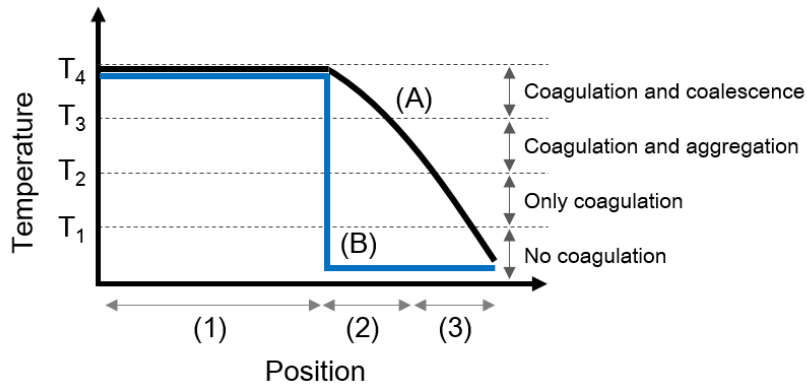


Figure 3. Schematic of (A) a typical and (B) an ideal temperature distribution during gas phase synthesis of particles ((1) Hot zone, (2) Insulating zone, (3) Cooling zone).

For this reason, a new type of reactor as shown in Figure 1B is proposed in this study. The main difference is that the reactor is vertically placed. For a narrow residence time distribution and a short mean residence time, the gas flow in a reactor should be axisymmetric. The horizontal reactor is not suitable to achieve the axisymmetric gas flow due to the fact that the flow direction is vertical to the gravity in a horizontal reactor. The buoyancy effect is inevitable in both a horizontal reactor and a vertical reactor due to the fact that there is a region where cold and hot gases coexist. To avoid/minimize the buoyancy effect, H₂ is injected to the top of the reactor, and the outlet is placed at the middle of the reaction zone. The upper part from the outlet will be filled with cold H₂ from the top of the reactor. Therefore, Ni particles generated in the reaction zone will be exhausted to the outlet without passing through the region where hot and cold gases coexist. The diameter of outlet is a tenth part of the one of reactor. Hence Ni particles will be quenched in a short time, and the formation of aggregates will be suppressed by using the vertical reactor.

Figure 4B and 4C show CFD analysis results for the vertical reactor. It is confirmed that the upper part from outlet is filled with cold gas, and the lower part is filled with hot gas as shown in Figure 4C. From the analysis of particle trajectory as shown in Figure 4B, it is confirmed that a short mean residence time and a narrow residence time distribution of particles could be achieved by the vertical reactor. Furthermore, this gas flow condition in the vertical reactor is suitable not only for the avoiding of the formation of aggregates, but also for the synthesis of monodisperse particles in the gas phase, only more efforts should be made for it. This will be discussed in a later part.

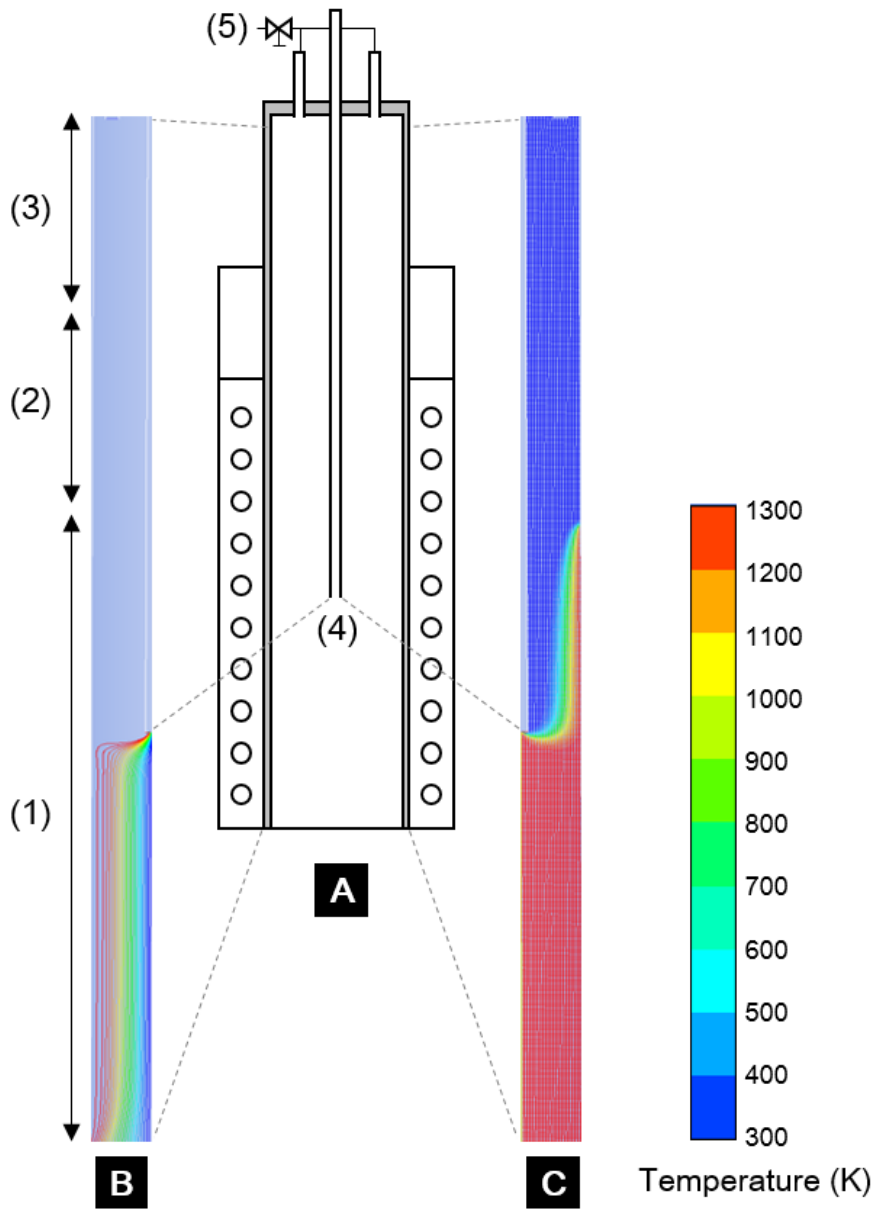


Figure 4. (A) Schematic of a vertical reactor and CFD analysis of (B) the particle trajectory (Colored to distinguish each particles) and (C) the temperature distribution on an axisymmetric plane ((1) second Heating zone, (2) Insulating zone, (3) Cooling zone, (4) Outlet, (5) H₂ inlet).

Also the difference between a horizontal and a vertical reactor was experimentally observed. The Figure 5 shows the SEM images of Ni particles prepared by a horizontal and a vertical reactor. The Figure 5A shows Ni nanoparticles prepared by a horizontal reactor, it is observed that their size distribution is relatively wide and an amount of aggregates is observed. The Figure 5B shows Ni nanoparticles prepared by a vertical reactor. It is observed that their size distribution is nearly monodisperse and few aggregates is observed. This result indicates that a short mean residence time and a narrow residence time distribution of particles could be achieved by a vertical reactor.

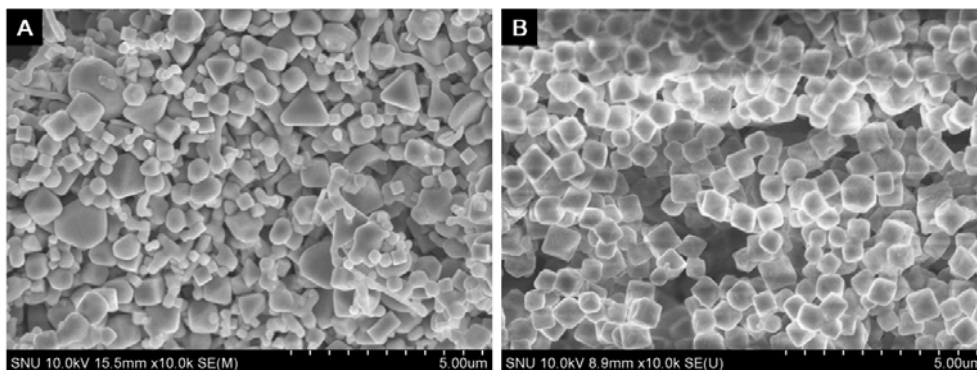
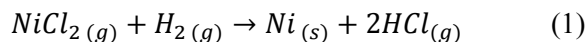


Figure 5. SEM images of nickel particles prepared by (A) a horizontal reactor and (B) a vertical reactor. The particle collection was done for 30 min under the first heating zone temperature of 850 °C, the second heating zone temperature of 950 °C, H₂ flow rate of 105 sccm and the N₂ flow rate of 500 sccm.

3-2. Conditions for synthesis of monodisperse particles

The following three conditions should be satisfied for the gas phase synthesis of monodisperse particles. The first condition is the avoiding of the formation of aggregates which could be achieved by a vertical reactor. The second condition is the same growth rate for all particles. This is also could be achieved by a vertical reactor due to a narrow residence time distribution of particles. The last condition is the separation of a nucleation and a growth stage. In the other words, an additional nucleation should be inhibited during a growth stage. It can be achieved by the initial burst of nucleation, where an appreciable amount of supersaturation is consumed during the burst of nucleation and the supersaturation should be maintained below the critical supersaturation for nucleation during growth according to La Mer model.

For the initial burst of nucleation, a fast reaction rate should be made. The reaction rate can be controlled by two ways. The first way is the increasing of reactants according to Le Châtelier's principle. In this system, the reactants are NiCl₂ and H₂ as shown in eq. 1. The increase of NiCl₂ used as a precursor is not unfavorable for a maintenance of low supersaturation during growth. Hence, only the flow rate of H₂ between reactants could be controlled for a fast reaction rate. The second way is the increasing of the reaction temperature according to Arrhenius equation.



However, in this system, it is not easy to control the reaction rate by both ways. Figure 6 shows the schematic of a temperature distribution in a vertical reactor. The

regions of constant temperature called “hot zone” are marked as (6) and (7). It is ideal for monodispersity that the reaction occurs in the hot zone of the second heating zone where the temperature is constant and the highest. If the reaction occurs in the region where the temperature is not constant, particularly is increasing, an additional nucleation should occur. And the reaction in the highest temperature region is desirable for the initial burst of nucleation. The temperature of an evaporation zone is decided by a vapor pressure of a precursor to evaporate and the temperature of a reaction zone is decided by considering of both thermodynamics and kinetics of the reaction. Generally the temperature of reaction zone is higher than one of evaporation zone, or the nucleation of precursor will occur without reduction of it. Consequently, the difference between evaporation and reaction zone causes the region where hot and cold gases coexist between them (marked as (2) in Figure 6), and makes the diffusivity of gases in a reaction zone relatively higher than one in an evaporation zone. It means that the region where the reaction occurs is not fixed but movable depending on the difference between both temperatures. If the reaction doesn't occur in the hot zone, it will occur in the region where the temperature is increasing around the insulating zone between hot zones (marked as (2) in Figure 6). Then, it is hard to expect the separation of nucleation and growth. Therefore appropriate temperatures should be considered by both points of view, the reaction temperature and for the position where reaction occurs. In case of the increasing of H_2 , H_2 will diffuse so far that the reaction will not occur in the hot zone, either. Therefore, appropriate flow rates should be considered.

For this reason, additional parameters should be added for the reaction in the hot zone and the high reaction rate. There are many parameters for it as following: the position of outlet, a distance between position of precursor and reaction zone, and a volume ratio of upper part where H_2 passes through to lower part where $NiCl_2$ and

N₂ pass through. By adjusting the outlet position, the position where reaction occurs can be controlled, but it also affects the flow condition where particles pass through. Especially, if particles are exposed to the flow condition where hot and cold gases coexist near the insulating zone marked as (3) in Figure 6, monodispersity of particles cannot be achieved.

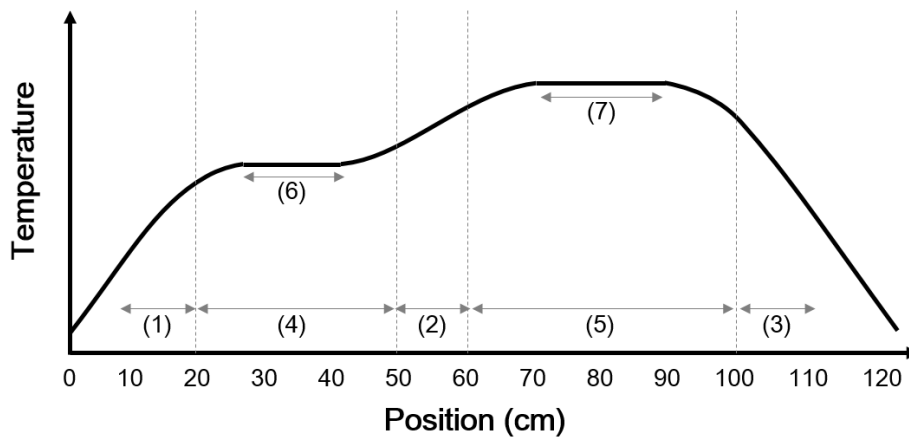


Figure 6. Schematic of temperature distribution in a vertical reactor. ((1-3) insulating zone, (4) first heating zone, (5) second heating zone, (6, 7) hot zone)

Heightening the position of precursor evaporated in the first heating zone is favorable for the reaction in the hot zone. However, there is a limit due to the fact that the precursor should be placed at the constant temperature region for the constant vapor pressure of NiCl₂. If the position of precursor is placed out of the hot zone (marked as (6) in Figure 6), not only the distance between a precursor and a reaction region but also the vapor pressure of a precursor will be changed. Increasing the volume ratio of upper part to lower part in a reactor is favorable for the reaction in

the hot zone, but if it is exceeded, it will cause the decreasing of H₂ participating in the reaction. Hence, these parameters should be controlled appropriately.

3-3. Effect of the temperature of second heating zone

Figure 7 shows the SEM images of Ni particles depending on the temperature ratio. The syntheses of Ni particles were performed where the temperature of the first zone was maintained as 850°C, and the temperature of the second zone was varied at 950, 1050, and 1100°C.

Where the reaction occurred can be observed from the films deposited on the inner wall of a reactor after experiments. It is confirmed that the reaction occurs at 68, 63, and 57cm of a reactor when the temperature of the first heating zone is fixed as 850°C and the temperature of the second heating zone is 950, 1050, or 1100°C respectively (second heating zone is placed at 60~100cm, first heating zone is placed at 20~50cm, as shown in Figure 6). Therefore all of the reactions occurred at the region where the temperature is not constant but increasing.

It was observed that the shape of Ni particles is nearly perfect cubic when the temperature of the second zone is 950°C as shown in Figure 7A. The size of them is around 200nm, and the size distribution is quite narrow except a few large particles near 400 nm. Both spherical and cubic Ni particles were observed when the temperature of the second zone is 1050°C as shown in Figure 7B.

The size distribution of cubic Ni particles is relatively wide, but the one of spherical Ni particles is nearly monodisperse. The average size of cubic particles is around 500 nm, and the average size of spherical ones is around 200 nm. Both spherical and

cubic Ni particles are observed when the temperature of the second zone is 1100°C as shown in Figure 7C. The cubic particles shown in Figure 7C are relatively roughened than ones shown in Figure 7A. The average size of both shaped particles is similar and around 400 nm.

Cubic Ni particles synthesized when the temperature of the second heating zone is 950 °C are nearly monodisperse. Therefore the conditions for monodispersity of cubic Ni particles would be satisfied. However the conditions for monodispersity of spherical Ni particles are stricter than ones for cubes.

The study about the mechanism of the shape evolution of Ni particles was already discussed in the previous chapter, so it will not be discussed in detail. It was confirmed in the other study that the cubic Ni nanoparticles are stabilized by adsorption on the {100} surfaces of Ni particles by NiCl₂. It was also confirmed that spherical Ni particles were observed when the reaction rate was appropriately fast.

According to this mechanism, reaction rate would affect to not only the size distribution of particles, but also the shape of them. Therefore, it can be predicted that the cubic Ni nanoparticles are synthesized under the relatively low reaction rate condition when the temperature of the second heating zone is 950 °C as shown in Figure 7A.

When the temperature of the second heating zone was 1050 °C, both spherical and cubic are observed, and the average size of them is far different. From this result, it can be predicted that an additional nucleation occurred. Spherical Ni particles would be formed by an additional nucleation due to the fact that their average size is relatively smaller than cubic ones. Also, after an additional nucleation, the shape of Ni particles is hard to be cubic due to the consumption of NiCl₂ vapor stabilizing the {100} surfaces of Ni particles.

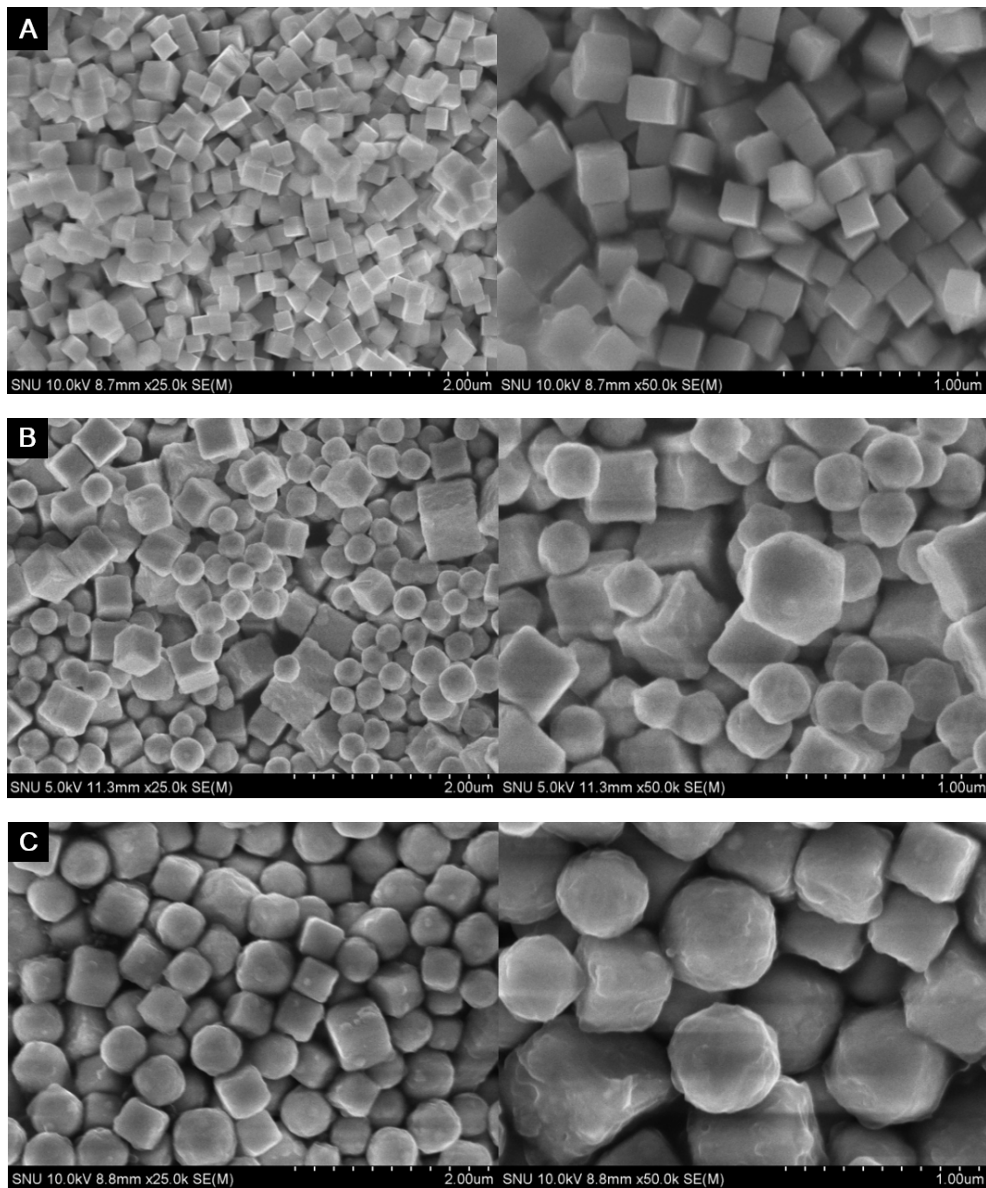


Figure 7. SEM images of nickel particles prepared by a vertical reactor. The particle collection was done for 30 min under the first heating zone temperature of 850 °C, the second heating zone temperature of (A) 950, (B) 1050, or (C) 1100°C, H₂ flow rate of 125 sccm and the N₂ flow rate of 500 sccm.

When the temperature of the second heating zone was 1100 °C, both nearly monodisperse spheres and roughened cubes are observed, and the average size of them is similar. It can be predicted that the reaction occurs at a quite high temperature but the reaction rate is not high enough to avoid the formation of the cubic Ni particles.

3-4. Effect of the outlet position

Figure 8 shows SEM images of Ni particles prepared by a vertical reactor. To examine the effect of the outlet position the outlet position was varied at 70, 80, or 90 cm. It was confirmed that the reaction occurs at 54, 63, and 75cm of a reactor when the outlet is placed at 70, 80, 90 cm respectively.

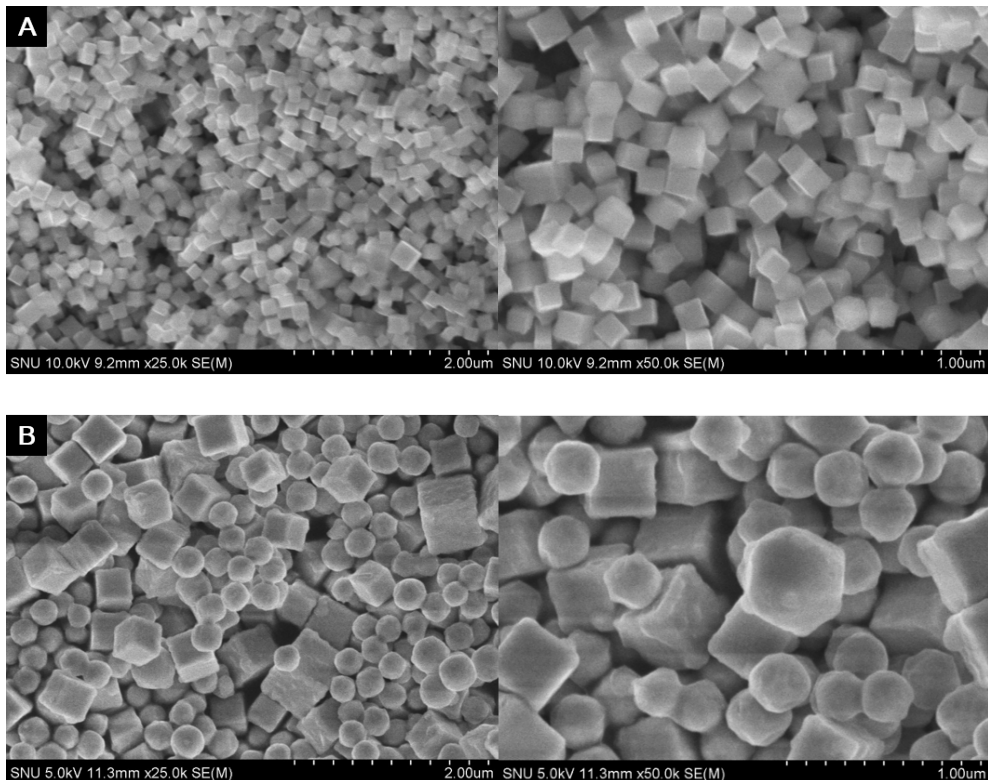
Figure 8A shows cubic Ni particles prepared under the outlet position of 70 cm. It is confirmed that the average size of them is around 120 nm, and the size distribution is quite narrow.

Figure 8B shows both cubic and spherical Ni particles prepared under the outlet position of 80 cm. The size distribution of cubic Ni particles is relatively wide, but the one of spherical Ni particles is nearly monodisperse. It is confirmed that the average size of cubic particles is around 500 nm, and the average size of spherical ones is around 200 nm.

Figure 8C shows irregular shaped Ni particles prepared under the outlet position of 90 cm. It is confirmed that the average size of them is around 500 nm.

From the observation of deposited films on the inner wall, it can be predicted that the reaction temperature increases with increasing a height of the outlet. The outlet position also affects the temperature of the region where particles pass through before the outlet. If particles are exposed to the high temperature region, they will grow not only by atoms but also by coalescence. Therefore, the size difference with the outlet position can be explained.

Meanwhile, the Ni particles of irregular shape when the outlet is placed at 60 cm, can be explained by the buoyancy effect. As shown in Figure 6, the temperature is decreasing around the outlet at 60 cm. Therefore, the flow condition where hot and cold gases coexist, causes a wide residence time distribution of particles.



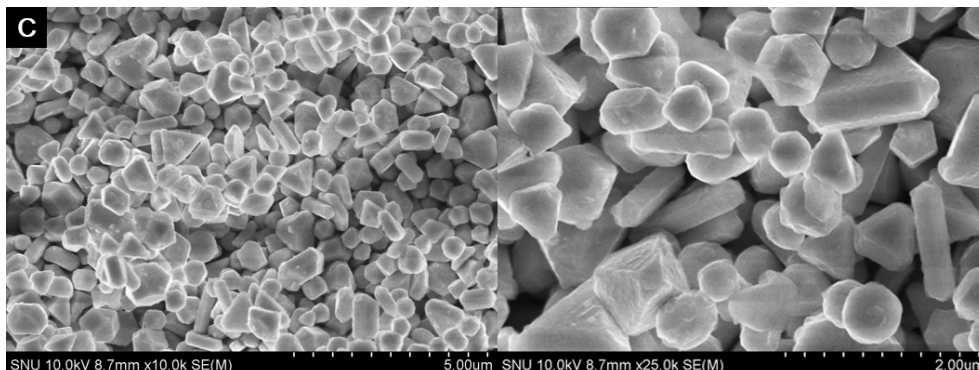


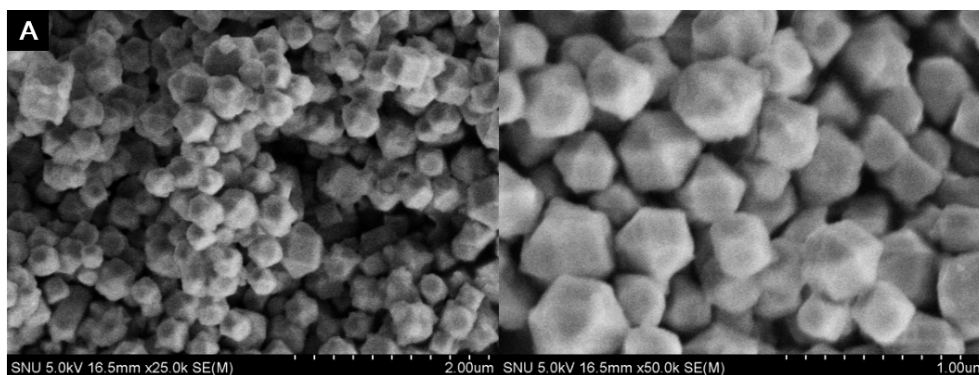
Figure 8. SEM images of nickel particles prepared by a vertical reactor. The outlet position was varied at (A) 70, (B) 80, or (C) 90 cm. The particle collection was done for 30 min under the first heating zone temperature of 850 °C, the second heating zone temperature of 1050 °C, H₂ flow rate of 125 sccm and the N₂ flow rate of 500 sccm.

3-5. Effect of the temperature of first heating zone

Figure 9 shows SEM images of Ni particles prepared by a vertical reactor. To examine the effect of the temperature of the first heating zone, the first heating zone temperature was varied at 750, 800, 850, or 900 °C. The decreasing of vapor pressure of a precursor is favorable not only for the maintenance of supersaturation below the critical supersaturation for nucleation during growth but also for the spherical shaped Ni particles. However, the temperature of the first heating zone where a precursor is placed, affects both the vapor pressure of a precursor and the region where the reaction occurs as discussed already. It is confirmed that the reaction occurs at 63, 68, and 71cm of a reactor when the temperature of the first heating is varied 800, 850, or 900°C respectively. Therefore, the reaction position should be lowered with

decreasing of first heating zone temperature. The deposited films on the inner wall of the reactor when the first heating zone temperature was 750 °C, was not observed due to the low evaporation rate. However, the position of reaction should be lowered than others as following the tendency.

Figure 9A shows cuboctahedral Ni particles prepared under the first heating zone temperature of 750 °C. It is confirmed that the average size of them is around 300 nm, and the size distribution is quite wide. Figure 9B shows cubic Ni particles prepared under the first heating zone temperature of 800 °C. It is confirmed that the average size of them is around 150 nm, and the size distribution is quite narrow except few large particles near 300 nm. Figure 9C shows cubic Ni particles prepared under the first heating zone temperature of 850 °C. It is confirmed that the average size of them is around 200 nm, and the size distribution is quite narrow except few large particles near 400 nm. Figure 9D shows cubic Ni particles prepared under the first heating zone temperature of 900 °C. It is confirmed that the average size of them is around 400 nm, and the size distribution is quite wide, and a few spherical Ni particles are also observed.



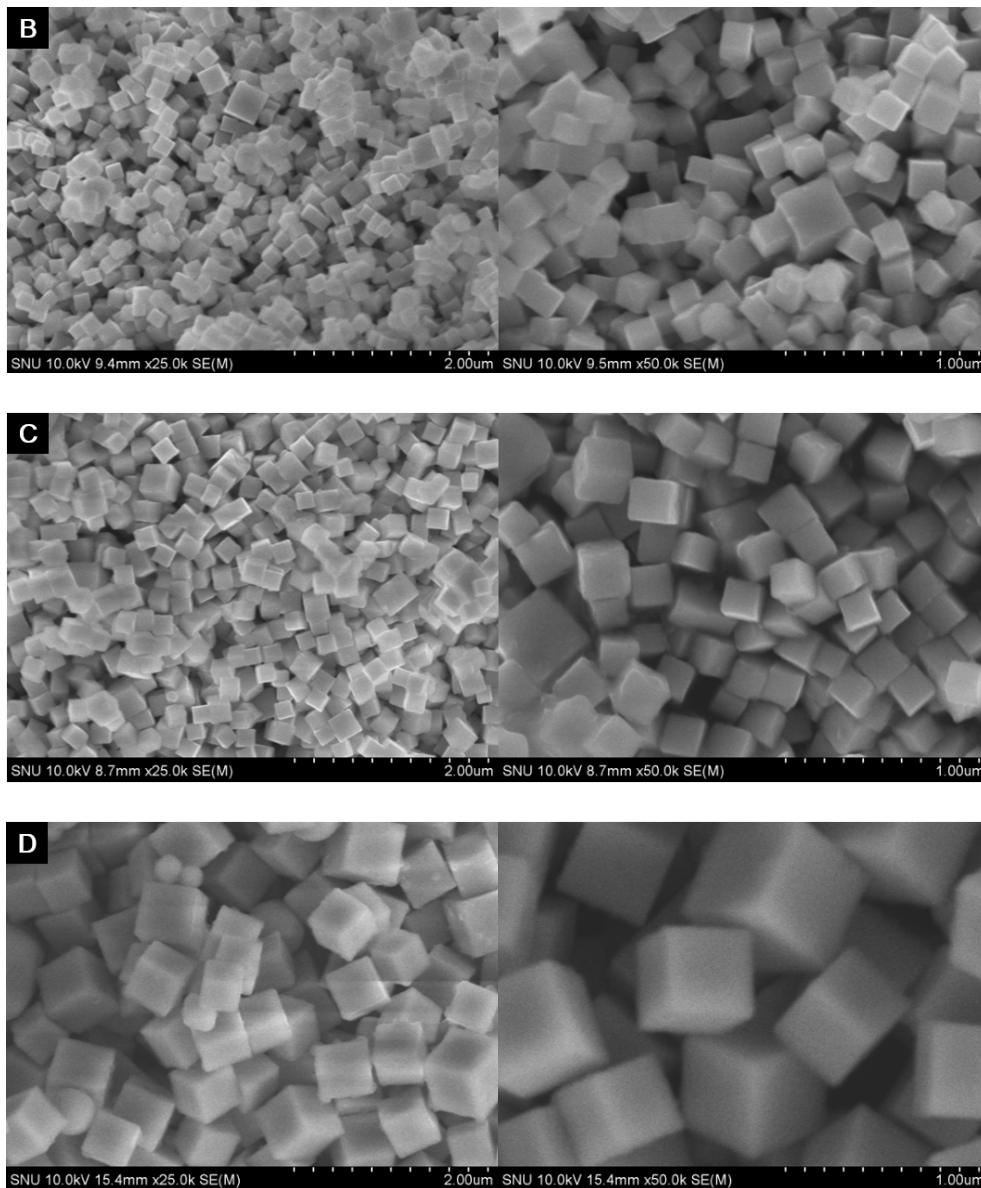


Figure 9. SEM images of nickel particles prepared by a vertical reactor. The particle collection was done for 30 min under the first heating zone temperature of 750, 800, 850, or 900 °C, the second heating zone temperature of 950 °C, H₂ flow rate of 125 sccm and the N₂ flow rate of 500 sccm.

3-6. Effect of the precursor position

Figure 10 shows the SEM images of nickel particles prepared by a vertical reactor with varying the precursor position as 27, 31, 35, or 43cm. The precursor position affects the evaporation temperature as well as the position of the region where reaction occurs. If the precursor is placed at the higher position, the reaction will occur at the higher position where the temperature is higher.

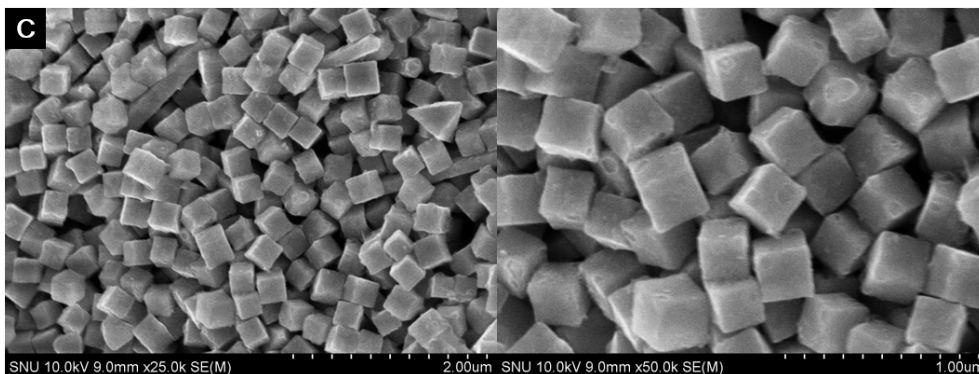
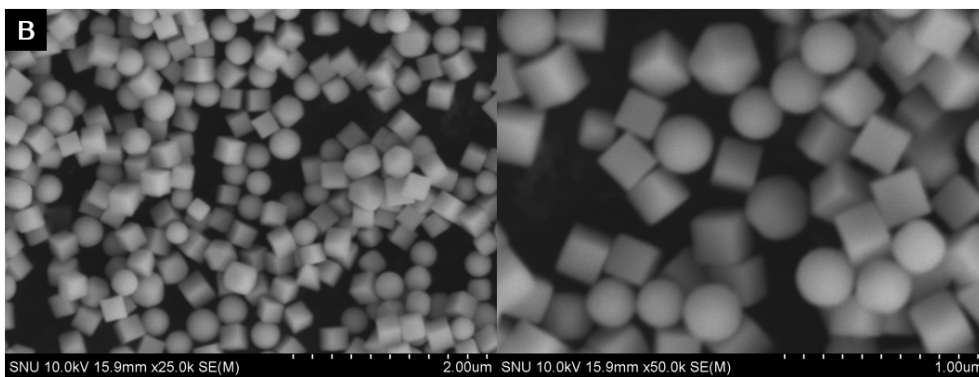
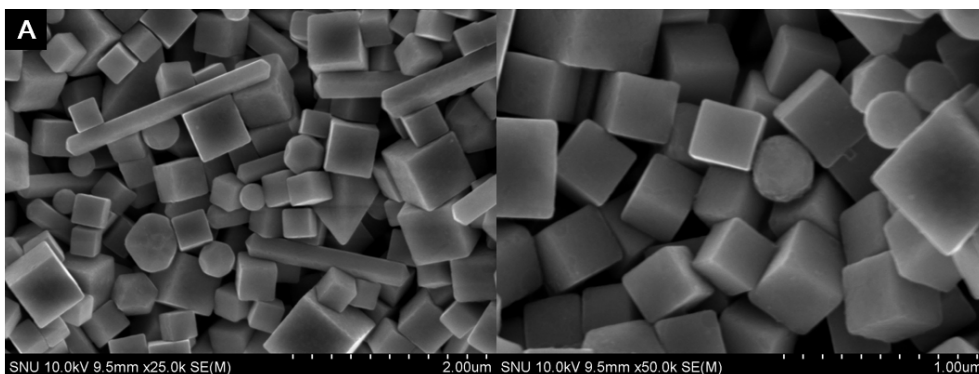
Figure 10A shows the Ni particles prepared where the precursor is placed at 27 cm. The cubic Ni particles whose average size is around 400 nm, the spherical Ni particles whose average size is around 200 nm, and a few nanorods whose diameter is around 200 nm, are observed. And their size distribution is quite wide.

Figure 10B shows the Ni particles prepared where the precursor is placed at 31 cm. The nearly monodisperse cubic Ni particles whose average size is around 200 nm, and the nearly monodisperse spherical Ni particles whose average size is around 200 nm, are observed. The ratio of the cubic particles to the spherical ones is almost 1.

Figure 10C shows the Ni particles prepared where the precursor is placed at 35 cm. The nearly monodisperse cubic Ni particles whose average size is around 250 nm, and a few nanorods are observed.

Figure 10D shows the Ni particles prepared where the precursor is placed at 43 cm. The nearly monodisperse cubic Ni particles whose average size is around 200 nm, and the nearly monodisperse spherical Ni particles whose average size is around 300 nm, are observed. The ratio of the cubic particles to the spherical ones is almost 1. This result indicates that the reaction rate can be controlled by the position of the precursor. Therefore, nearly monodisperse cubic Ni particles are synthesized and the

ratio of cubic particles to spherical ones is quite decreased, but it is fact that the cubic particles are still observed. It can be predicted that the formation of both cubic and spherical particles is due to the fact that the reaction occurs where the temperature is increasing.



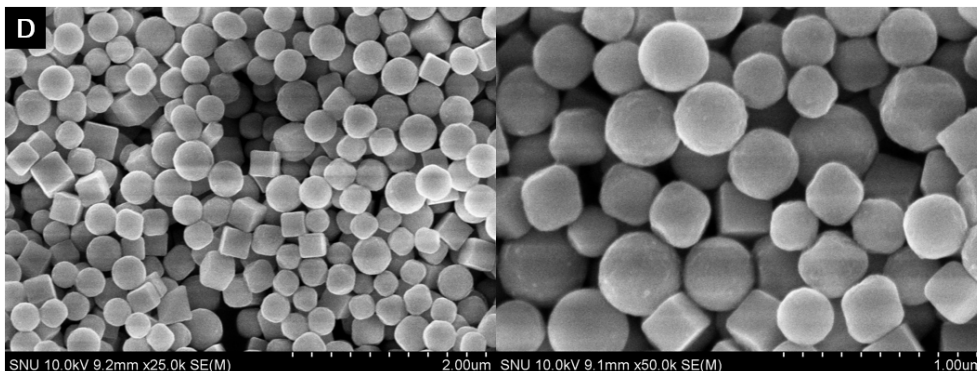


Figure 10. SEM images of nickel particles prepared by a vertical reactor. The position of NiCl_2 in a crucible was varied at (A) 27, (B) 31, (C) 35, or (D) 43cm. The particle collection was done for 30 min under the first heating zone temperature of $850\text{ }^\circ\text{C}$, the second heating zone temperature of $1000\text{ }^\circ\text{C}$, H_2 flow rate of 125 sccm and the N_2 flow rate of 500 sccm.

3-7. Effect of the volume ratio

Figure 11 shows the SEM images of nickel particles prepared by a vertical reactor with varying the length of a reactor as 120, or 130 cm. It is confirmed that the reaction occurs at higher position when the length where H_2 passes through is increased.

Figure 11A shows the Ni particles prepared when the length of a reactor is 120 cm. Both cubic and spherical Ni particles are observed. The ratio of cubic particles to spherical ones is almost 1. Figure 11B shows the Ni particles prepared when the length of a reactor is 130 cm. Both cubic and spherical Ni particles are observed, but the ratio of cubic particles to spherical ones is quite decreased. Also it is confirmed

that their size distribution is quite narrow. However, it can be predicted that the both cubic and spherical Ni particles are synthesized due to the fact that reaction occurs where the temperature is increasing.

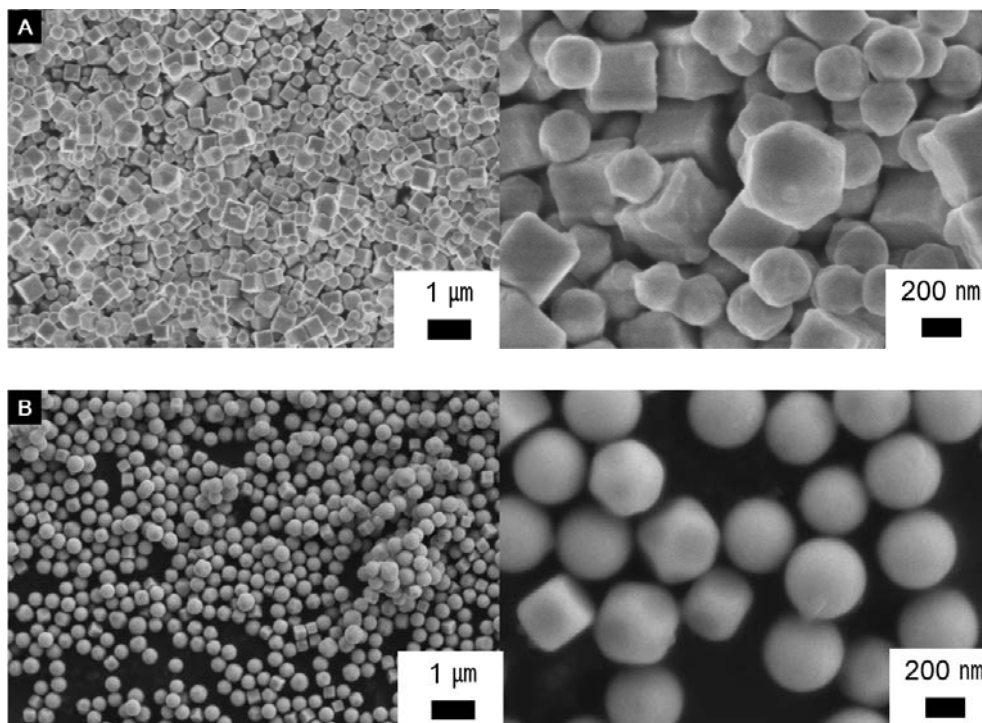


Figure 11. SEM images of nickel particles prepared by a vertical reactor. The length of a quartz reactor was varied at (A) 120 or (B) 130 cm. The particle collection was done for 30 min under the first heating zone temperature of 850 °C, the second heating zone temperature of 950 °C, H₂ flow rate of 125 sccm and the N₂ flow rate of 500 sccm.

3-8. Improvement of vertical reactor

To control the region where reaction occurs, many parameters were considered. However, it was confirmed that it was complicated to control the parameters to synthesize monodisperse and spherical Ni particles. Also, the cubic Ni particles were still observed after optimization of parameters. For this reason, the improvement of a vertical reactor was proposed as shown in Figure 1C.

From the results by a vertical reactor, it is confirmed that the key factor for the synthesis of monodisperse spherical Ni particles is where the reaction occurs. It is confirmed that it is still not sufficient for the reaction in the hot zone, although many parameters are considered. The main problem of a vertical reactor, under the conditions for fast reaction rate, it tends to cause the reaction at the region where the temperature is increasing and lower than one in the hot zone. It is predicted that the reaction at low temperature is caused by high diffusivity of H₂ or low diffusivity of NiCl₂.

From this point of view, if NiCl₂ is isolated before the reaching to the hot zone, the reaction will occur in the hot zone. Hence, the inner quartz tube is inserted inside the quartz reactor to isolate NiCl₂ vapor. By using this improved vertical reactor, it is confirmed that nearly monodisperse spherical Ni particles without cubic ones can be synthesized. The conditions for the average sizes of approximately 500, 200, 100, 75, and 50 nm was confirmed. The exact average size and size distribution will be introduced in the last of this chapter.

The size of particles was controlled by two ways. The first thing is the adjusting the vapor pressure of precursor. The second thing is the adjusting the total flow rate of gases. The change of vapor pressure of precursor affects not only the size but also

the shape of particles as discussed already. In the case of the total flow rate, if it is exceeded, the time is probably not enough to heating the gases, then it would cause the temperature gradient in the hot zone. If the total flow rate is too lowered, it will increase the chance of the Brownian coagulation between the particles. Therefore it is more favorable to adjust not by only the evaporation temperature or the total flow rate, but both of them appropriately.

Table 2. The conditions for monodisperse Ni spheres by using an improved vertical reactor.

| Average size (nm) | Nitrogen (sccm) | Hydrogen (sccm) | | first heating temperature (°C) | second heating temperature (°C) | Outlet (cm) | Precursor (cm) |
|-------------------|-----------------|-----------------|--------|--------------------------------|---------------------------------|-------------|----------------|
| | | Top | Bottom | | | | |
| 500 | 50 | 10 | 10 | 875 | 1000 | 90 | 35 |
| 200 | 250 | 25 | 25 | 850 | 1000 | 85 | 35 |
| 100 | 250 | 25 | 25 | 850 | 1050 | 85 | 35 |
| 75 | 220 | 300 | 300 | 800 | 1050 | 85 | 35 |
| 50 | 300 | 30 | 30 | 775 | 950 | 85 | 35 |

Figure 13 shows TEM images of Ni particles which are the same sample with B in Figure 12. Figure 13a shows that Ni particles are perfect spherical shape. The diffraction pattern of the sphere in Figure 13b matched the reflection of {211} faces of single-crystalline Ni, confirming that the spherical Ni particle is pure single-crystalline Ni. Figure 13c shows that the agglomerated Ni particles, and they would be attached to each other by soft-agglomeration, but not by hard-agglomeration.

Figure 13d shows the oxide layer of Ni particles, and their thickness is approximately 3.5 nm. This result indicates that only native oxide layer was formed.

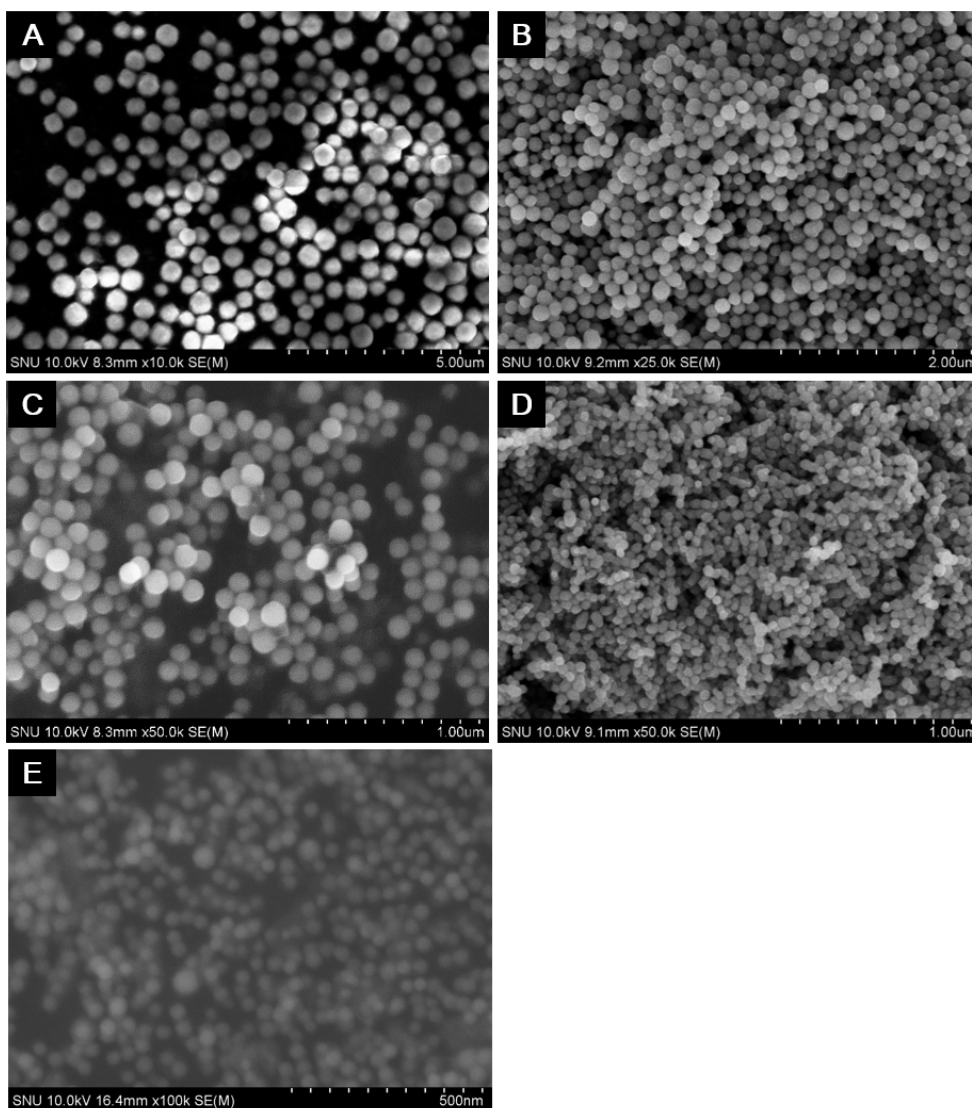


Figure 12. SEM images of nickel particles whose average size is (A) 500, (B) 200, (C) 100, (D) 75, and (E) 50 nm, prepared by a vertical reactor.

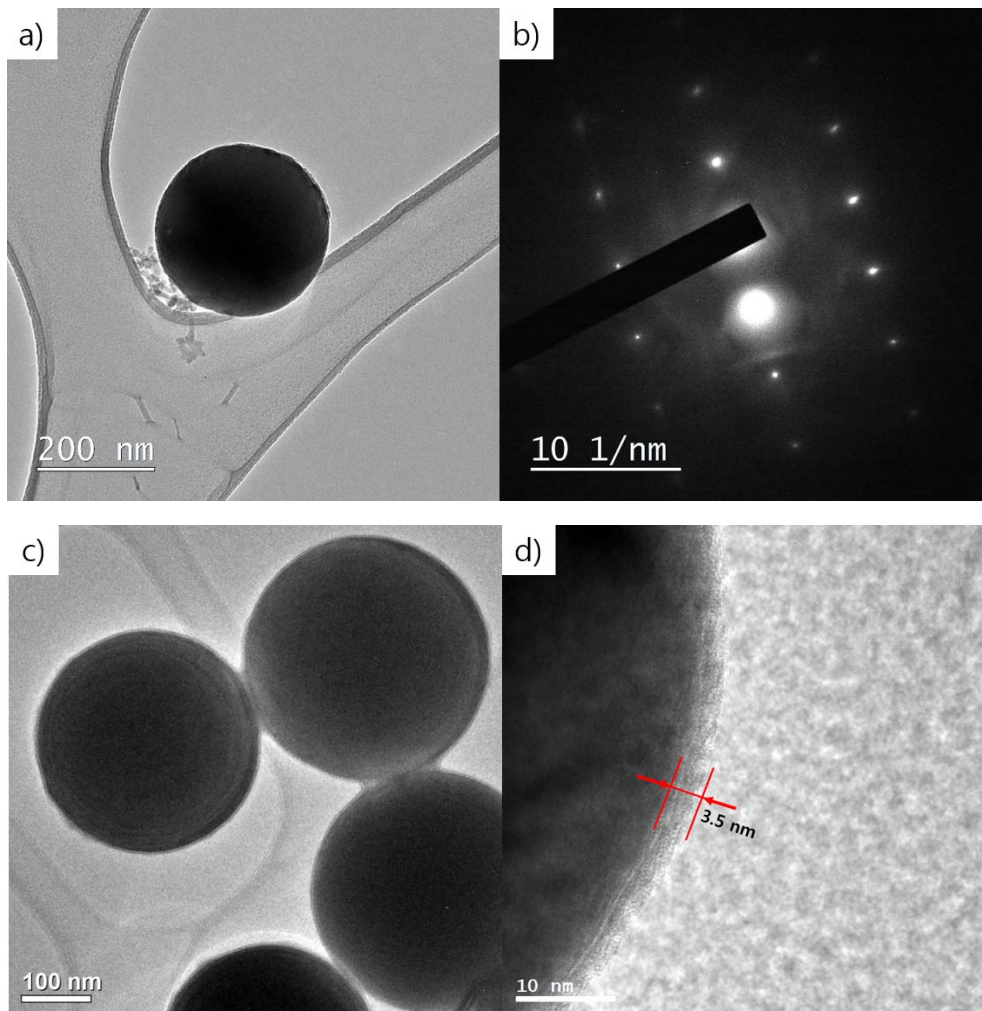


Figure 13. TEM images of nickel particles which are same with B in Figure 12. (a, c) spherical nickel particles, (b) diffraction pattern of sample (a), (d) oxide layer

The size distribution of Ni particles in Figure 12 was obtained by approximately measuring of the diameter with a ruler. From these measurement, the geometric standard deviation (GSD) and the mean size of particles were calculated. The size

distribution of Ni particles in Figure 12 are presented in Figure 14. The mean diameter and GSD are also presented in Figure 14.

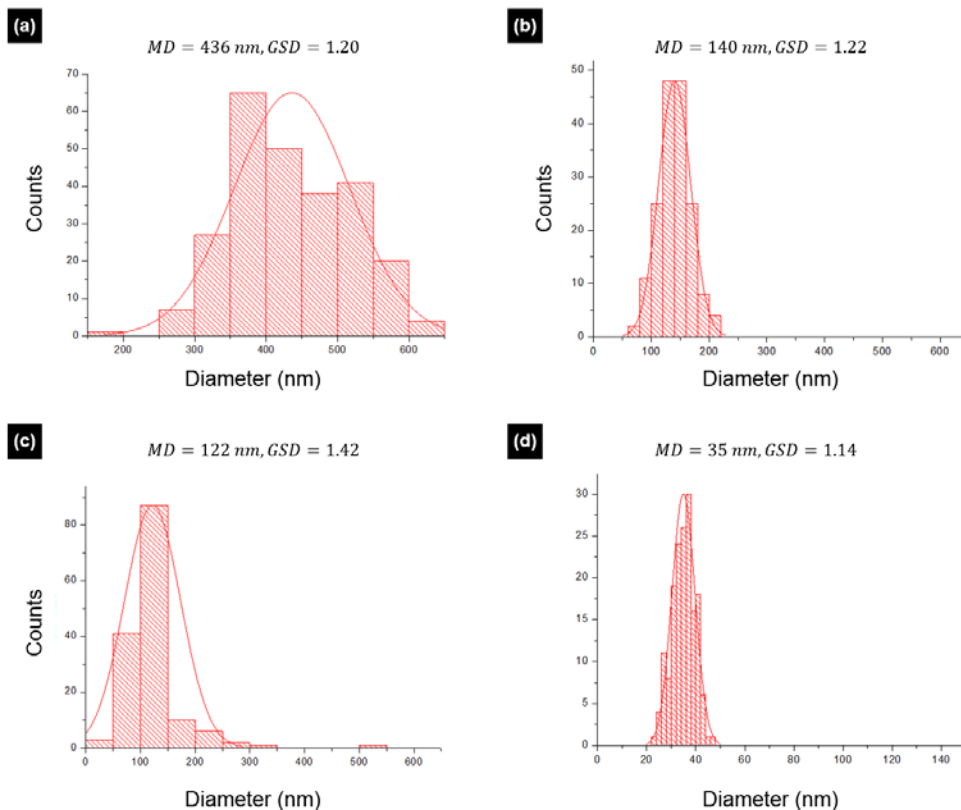


Figure 14. Size distribution of Ni particles in Figure 12. (a), (b), (c), and (d) are (a), (b), (c), and (d) respectively in Figure 12.

The size distribution of Ni particles in Figure 10d and 11b was also obtained by approximately measuring of the diameter with a ruler. From these measurement, the geometric standard deviation (GSD) and the mean size of particles were calculated. The size distribution of Ni particles in Figure 10d and 11b are presented in Figure 15. The mean diameter and GSD are also presented in Figure 15.

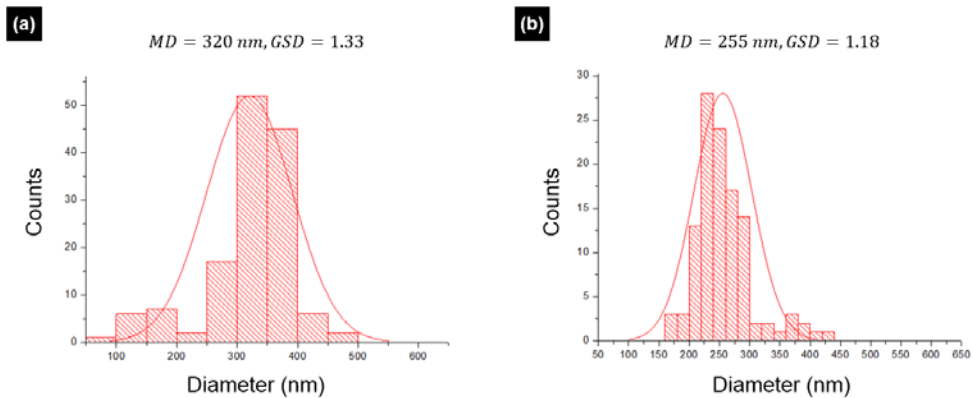


Figure 15. Size distribution of (a) Ni particles in Figure 11b, (b) Ni particles in Figure 10d.

4. Conclusion

The comparison between a horizontal and a vertical reactor was examined by experiment and CFD analysis. It is confirmed that the horizontal reactor tends to form the aggregation of particles. To solve this problem, a new type of reactor is proposed.

It is confirmed that the reaction in the hot zone is important for the synthesis of monodisperse and spherical Ni particles. The following parameters to control the reaction region, are considered: the position of outlet, a distance between position of precursor and reaction zone, and a volume ratio of upper part where H_2 passes through to lower part where $NiCl_2$ and N_2 pass through.

From the results by a vertical reactor, it is confirmed that the key factor for the synthesis of monodisperse spherical Ni particles is where the reaction occurs. It is confirmed that it is still not sufficient for the reaction in the hot zone, although many

parameters are considered. Hence, the improvement of a vertical reactor is proposed. By an improved vertical reactor, the monodisperse Ni spheres are successfully synthesized with less trial and error.

Chapter 5. Gas-phase synthesis of monodisperse metal nanoparticles

1. INTRODUCTION

In the previous works, the study of the gas-phase synthesis of monodisperse nanoparticles was performed only in the Ni CVD system. However the mechanism and method for the synthesis of monodisperse Ni particles can be applied to the other materials and methods. It is known that various metals such as Fe, Co, Ni, Ta, Nb, Mo, W, V and Ti can be synthesized by a reduction of their chlorides. The vapor pressures of various metal chlorides is presented in Figure 1. [94] Also, the Gibbs free energy changes of reactions are listed in Table 1. [94]

In this research, Fe and Co particles were synthesized by the modified vertical reactor which is same with the reactor which was used to synthesize Ni particles by CVD method.

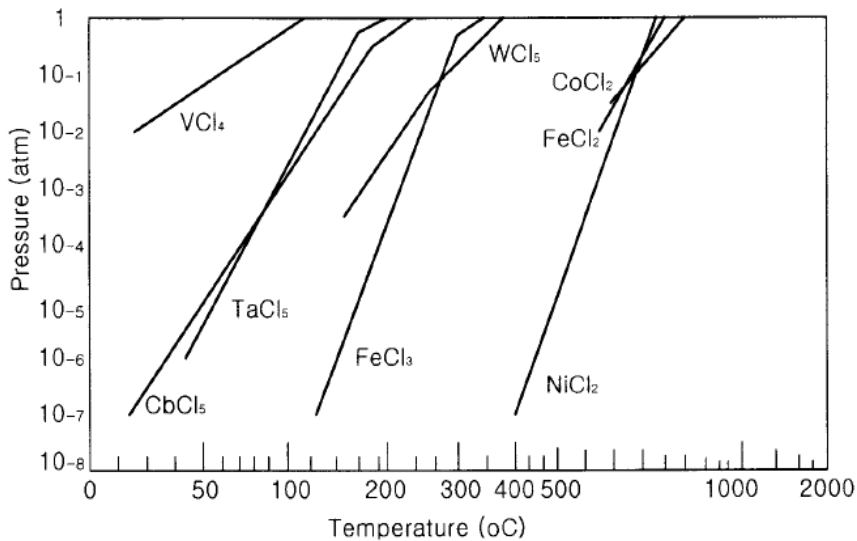


Figure 1. Vapor pressures of various metal chlorides. [94]

Table 1. Gibbs free energy change of the reduction of various metal chlorides by H₂. [94]

| REACTION | ΔG° , Kcal/mol | | | |
|---|-----------------------------|---------|----------|----------|
| | 800 K | 1000 K | 1200 K | 1400 K |
| $\text{CoCl}_2 + \text{H}_2 \rightarrow \text{Co} + 2\text{HCl}$ | -16.601 | -15.263 | -13.997 | -12.831 |
| $\text{FeCl}_2 + \text{H}_2 \rightarrow \text{Fe} + 2\text{HCl}$ | -4.772 | -3.343 | -2.290 | -1.276 |
| $\text{FeCl}_3 + 3/2\text{H}_2 \rightarrow \text{Fe} + 3\text{HCl}$ | -14.076 | -16.103 | -18.286 | -20.582 |
| $\text{NiCl}_2 + \text{H}_2 \rightarrow \text{Ni} + 2\text{HCl}$ | -22.150 | -20.703 | -19.250 | -17.806 |
| $\text{WCl}_6 + 3\text{H}_2 \rightarrow \text{W} + 6\text{HCl}$ | -77.367 | -91.822 | -105.975 | -119.946 |
| $\text{VCl}_4 + 3\text{H}_2 \rightarrow \text{V} + 4\text{HCl}$ | 10.040 | 3.767 | -2.377 | -8.494 |
| $\text{TaCl}_5 + 5/2\text{H}_2 \rightarrow \text{Ta} + 5\text{HCl}$ | 29.119 | 19.216 | 9.527 | -0.026 |
| $\text{NbCl}_5 + 5/2\text{H}_2 \rightarrow \text{Nb} + 5\text{HCl}$ | 13.691 | 3.595 | -6.307 | -16.069 |
| $\text{MoCl}_5 + 5/2\text{H}_2 \rightarrow \text{Mo} + 5\text{HCl}$ | -47.099 | -57.106 | -66.906 | -76.585 |

2. EXPERIMENTAL PROCEDURE

The experiments were carried out in the 2-stage vertical tubular reactor shown in Figure 2, consisting of a quartz tube with an inner diameter of 4.5 cm and a length of 120 cm. The synthetic conditions for Fe and Co particles are summarized in Table 2.

For the synthesis of Fe nanoparticles, carrier gas N₂ and reduction gas H₂ were passed through (10) and (11) respectively. A commercial FeCl₂ (Strem, anhydrous) or CoCl₂ (Aldrich, anhydrous) powder was put in the quartz crucible, which was placed in the center of the first heating zone (8) in Figure 2. Metal chlorides will be reduced by H₂ in the middle of the second heating zone (7) in Figure 2.

The particle collection was done for 30 min by filter which is connected to the outlet. The collected Ni particles were characterized by field-emission scanning electron microscope (FESEM, SU-70, Hitachi).

Table 2. Synthetic conditions for Fe and Co particles.

| Mat er. | Sample number | Zone 1 Temp. (°C) | Zone 2 Temp. (°C) | N ₂ | H ₂ , top | H ₂ , bottom | Outlet position (cm) | Crucible position (cm) | Middle tube type |
|------------|------------------|-------------------------|-------------------------|----------------|-------------------------|----------------------------|----------------------------|------------------------------|------------------------|
| Fe | a | 820 | 950 | 500 | 125 | - | 80 | 35 | - |
| Co | b | 825 | 1000 | 200 | 22 | 44 | 85 | 36.5 | Cylind er |
| | c | 850 | 950 | 250 | 22 | 22 | | | Cone |
| | d | | 1000 | | 40 | 40 | | | |

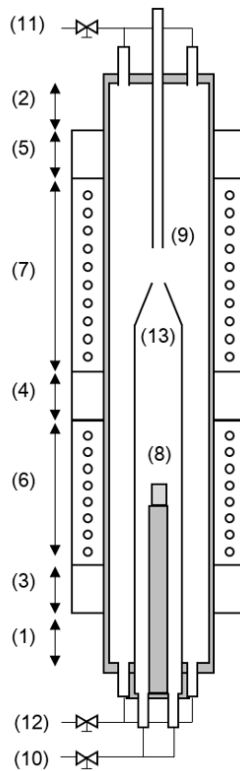


Figure 2. Schematics of reactor: (1, 2) cooling zone, (3-5) insulation, (6) first heating zone, (7) second heating zone, (8) NiCl₂ in crucible, (9) outlet, (10) N₂ inlet, (11) H₂ inlet

3. RESULTS AND DISCUSSION

Figure 3 shows the FESEM images of (a), (b), (c), and (d) in Table 2, respectively. Figure 3a shows Fe particles which are synthesized by the modified vertical reactor. The first heating zone temperature was 820 °C, the second heating zone temperature

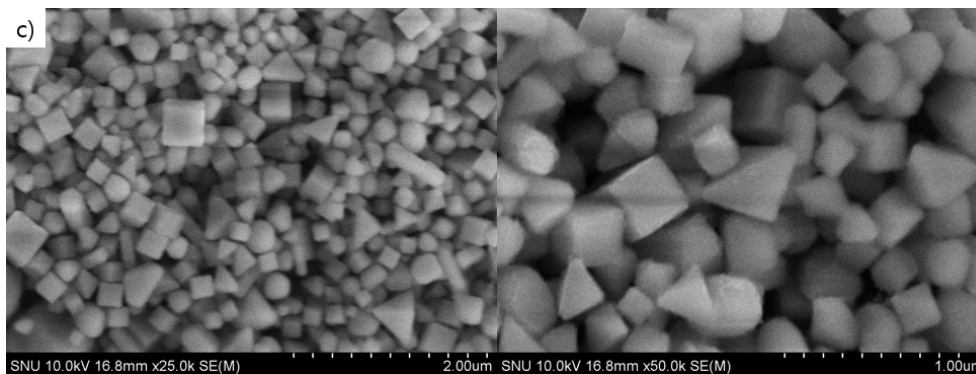
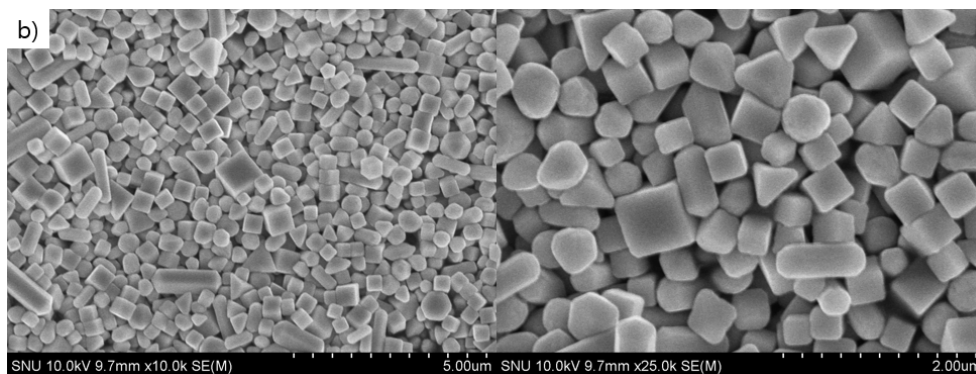
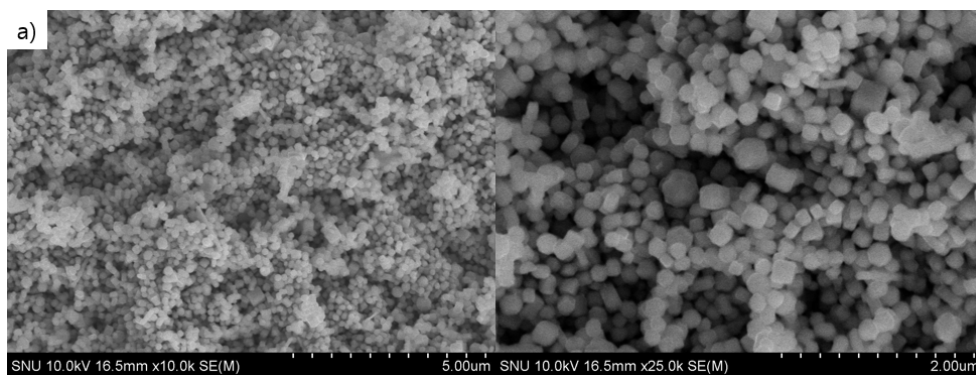
was 950 °C. The flow rate of N₂ and H₂ were 500 and 125 sccm, respectively. The outlet tube was placed at 80 cm. The crucible was placed at 35 cm. The mean diameter of particles is approximately 250 nm. Both cubic and spherical shapes were observed in Figure 3a.

Figure 3b-d show Co particles which are synthesized by the modified vertical reactor. Figure 3b shows Co particles which are synthesized by the modified vertical reactor. The first heating zone temperature was 825 °C, the second heating zone temperature was 1000 °C. The flow rate of N₂, H_{2, top} and H_{2, bottom} were 200, 22, and 44 sccm, respectively. The outlet tube was placed at 85 cm. The crucible was placed at 36.5 cm. The inner tube which is cylindrical tube was used. The mean diameter of particles in Figure 3b is approximately 350 nm. Various shaped particles such as cubes, tetrahedrons, spheres, and rods were observed in Figure 3b.

Figure 3c shows Co particles which are synthesized by the modified vertical reactor. The first heating zone temperature was 850 °C, the second heating zone temperature was 950 °C. The flow rate of N₂, H_{2, top} and H_{2, bottom} were 250, 22, and 22 sccm, respectively. The outlet tube was placed at 85 cm. The crucible was placed at 36.5 cm. The inner tube which is cylindrical tube with cone-like narrow end in Figure 2 was used. The mean diameter of particles in Figure 3c is approximately 200 nm. Various shaped particles such as cubes, tetrahedrons, spheres, and rods were observed in Figure 3c.

Figure 3d shows Co particles which are synthesized by the modified vertical reactor. The first heating zone temperature was 850 °C, the second heating zone temperature was 1000 °C. The flow rate of N₂, H_{2, top} and H_{2, bottom} were 250, 40, and 40 sccm, respectively. The outlet tube was placed at 85 cm. The crucible was placed at 36.5 cm. The inner tube which is cylindrical tube with cone-like narrow end in Figure 2

was used. The mean diameter of particles in Figure 3d is approximately 150 nm. Almost of Co particles in Figure 3d show the spherical shape.



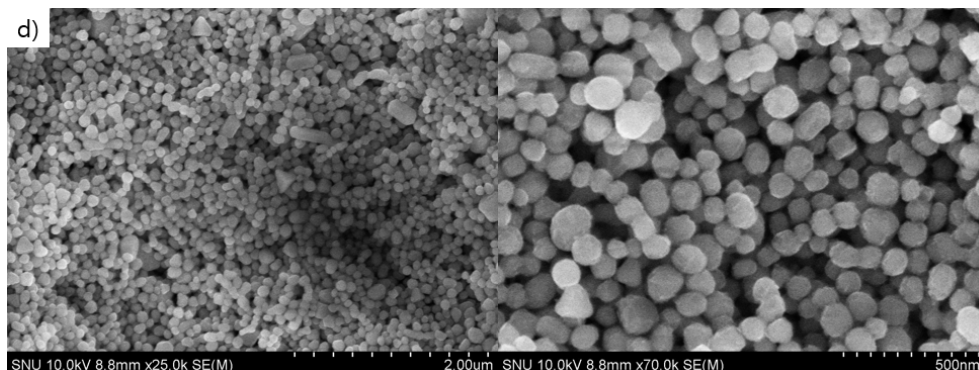


Figure 3. Fe and Co particles which prepared by the modified vertical reactor. (a) Fe particles, (b-d) Co particles. (a), (b), (c), and (d) show the SEM images of (a), (b), (c), and (d) in Table 2, respectively.

This result shows two possibilities. The first one is that the synthesis of monodisperse particles by modified vertical reactor might be applied to the other materials which are synthesized by reduction of metal chlorides. Figure 3d shows that the aggregation was inhibited, however the process parameters should be optimized by the additional experiments. The second one is that Fe and Co cubes were observed in Figure 3a-c. This means that FeCl_2 and CoCl_2 might stabilize $\{100\}$ surfaces of Fe and Co, respectively. The mechanism would be same with the stabilization of $\{100\}$ surfaces of Ni particles by the adsorption. The shape control of Fe and Co might be possible by controlling of reduction rate.

Considering that FeCl_2 and CoCl_2 vapor stabilizes $\{100\}$ faces of Fe and Co respectively, if the polycrystalline Fe or Co sheet is annealed under FeCl_2 or CoCl_2 atmosphere, the sheet is expected to have a cube texture with $\{100\}$ faces. As another application, the synthesis of cubic and spherical Fe and Co particles could be controlled systematically.

4. CONCLUSIONS

In conclusion, it was confirmed that the Fe and Co particles can be synthesized by the modified vertical CVD reactor. And Fe and Co cubes were observed. This means that FeCl_2 and CoCl_2 might stabilize $\{100\}$ surfaces of Fe and Co, respectively. Considering that FeCl_2 and CoCl_2 vapor stabilizes $\{100\}$ faces of Fe and Co respectively, if the polycrystalline Fe or Co sheet is annealed under FeCl_2 or CoCl_2 atmosphere, the sheet is expected to have a cube texture with $\{100\}$ faces. As another application, the synthesis of cubic and spherical Fe and Co particles could be controlled systematically.

Chapter 6. Gas-phase coagulation of nickel nanoparticles

1. INTRODUCTION

It is well known that the particles which are generated in the gas phase favor to form aggregates due to the high thermal energy. Also, the gas flow are affected by the buoyancy effect which was discussed in the previous chapter. For these reasons, the particles would change their morphology would be changed depending on the positions. Therefore, in this chapter, the aggregates of particles in the various position was experimentally observed to understand the morphological changes of Ni particles during a flight in the reactor.

2. EXPERIMENTAL PROCEDURE

The tube reactor to examine the effect of H₂ and NiCl₂ vapor is a 1-stage horizontal furnace, consisting of a quartz tube with an inner diameter of 4.5 cm and a length of 120 cm, which is shown in Figure 1. The circulating flow of gas in the both ends of a reactor is described in Figure 1. N₂ and H₂ was passed through an inlet of the quartz tube at the flow rate of 900 and 300 standard cubic centimeter per minute (sccm), respectively. To observe the Ni particles in the various position, the substrate was placed at A-D in Figure 2. A commercial nickel (II) chloride (NiCl₂) powder (98%, Aldrich) was put in the quartz crucible where the temperature is approximately 900 °C. The reaction temperature was controlled to be 950 °C. The deposition of Ni particles on the substrate was performed for the 5 min. The specimens were observed by field-emission scanning electron microscope (FESEM (SU-70, Hitachi)).

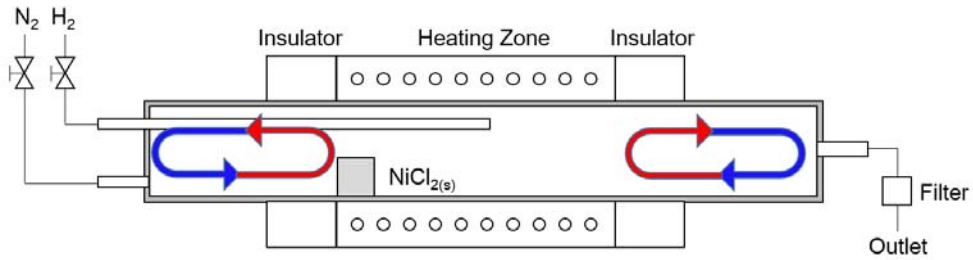


Figure 1. Schematic of the circulating gas flow in a horizontal reactor.

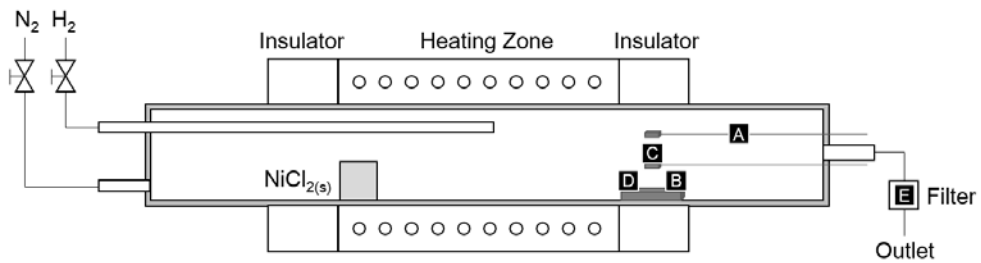


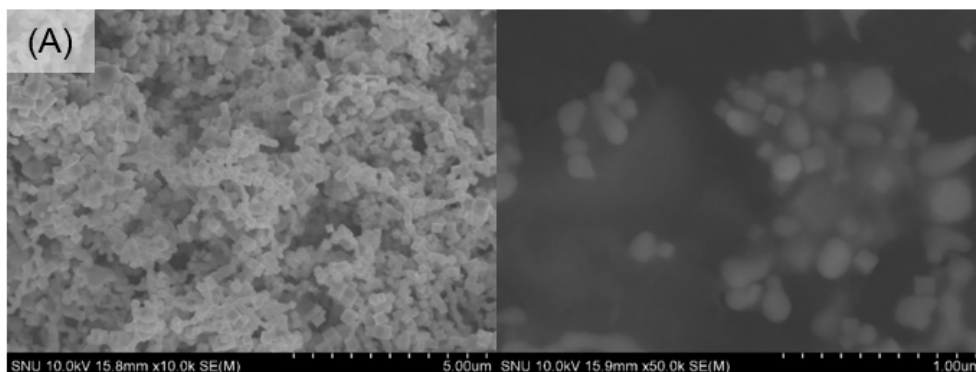
Figure 2. Positions of substrates to deposit Ni particles depending on the positions.

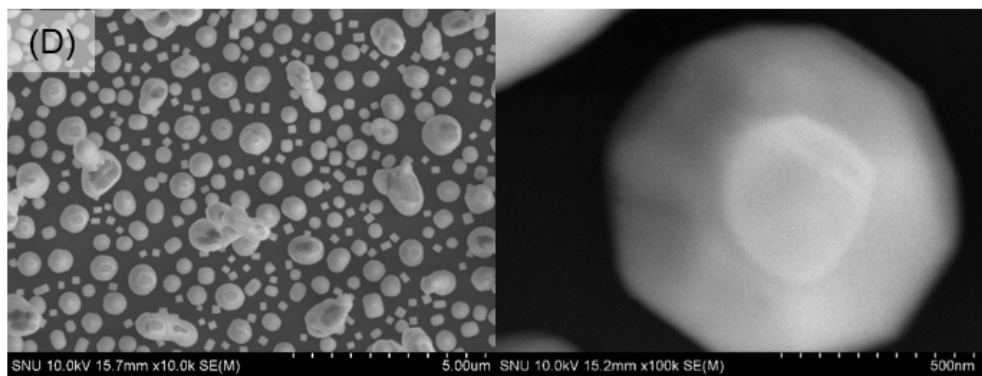
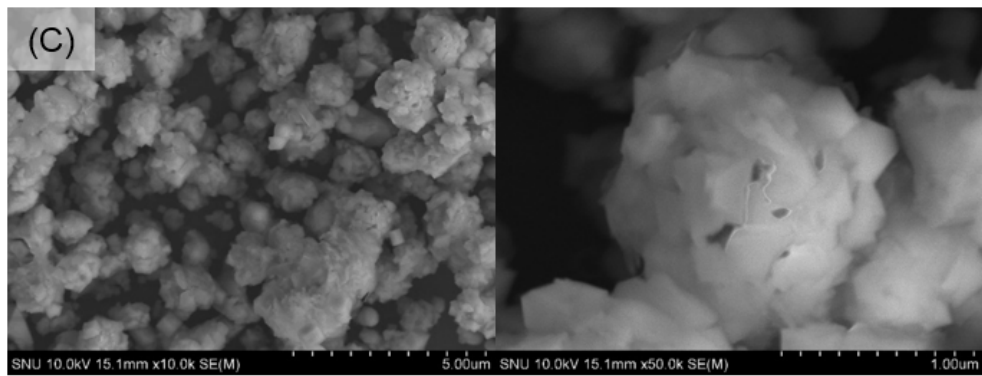
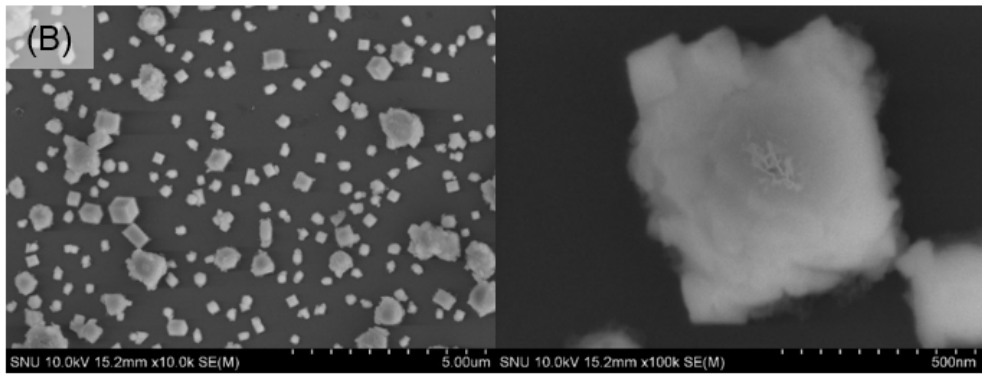
3. RESULTS AND DISCUSSION

Figure 3 shows FESEM images of Ni particles which are deposited substrates. Considering the circulating flow, the time-order of the positions would rank A, B, C or D. Figure 3E shows FESEM image of Ni particles which are collected in the filter which is connected to the outlet.

Ni particles which is shown in Figure 3A shows similar shape or a little thermal roughened shape with Ni particles in Figure 3E. Figure 3B shows the aggregates of Ni particles, the primary particles of the aggregates are expected to be cube. Also the aggregates show the cubic shapes. Figure 3C shows the aggregates of Ni particles, the primary particles of the aggregates are expected to be cube. However the aggregates show the roughened shapes. Figure 3D shows large particles with a size of ~700 nm which is similar size with Ni particles of Figure 3B and C.

Therefore it was confirmed that particles favor to form aggregates in the reactor. And the aggregates show cubic shape before thermal roughening in the higher temperature region. The cubic aggregates can change their shape into spheres by thermal roughening. These mean that the shape and size of Ni particles cannot be uniform under these conditions. It is described in Figure 4. Therefore, to synthesize the Ni particles with a uniform size and shape, this circulating gas flow should be inhibited. Considering this, the reactor was modified as introduced in the Chapter 2.





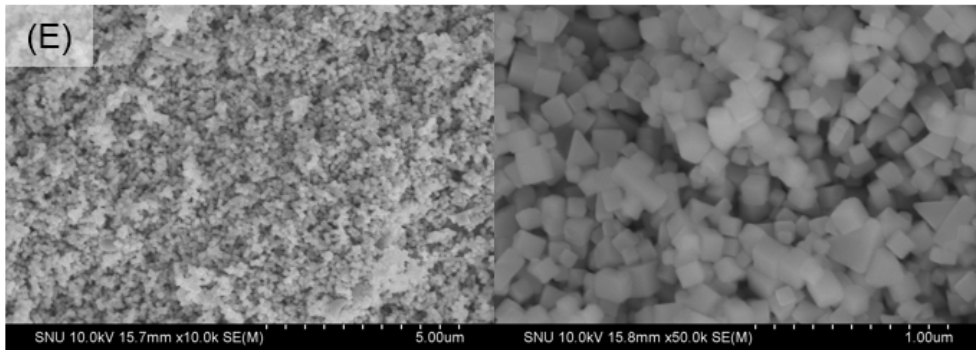


Figure 3. Deposited Ni particles on the substrates depending on the positions which are described in the Figure 2.

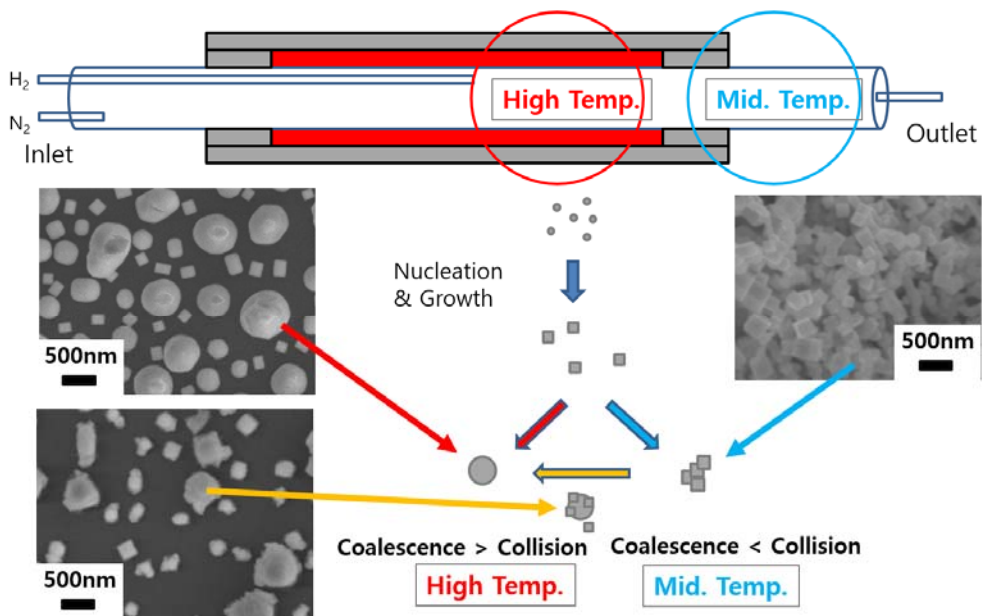


Figure 4. Shape and size changes of Ni particles during the flight in the reactor.

4. CONCLUSIONS

The aggregates of particles in the various position was experimentally observed to understand the morphological changes of Ni particles during a flight in the reactor. It was confirmed that the shape and size of Ni particles cannot be uniform in the horizontal reactor due to the circulating gas flow. For this reason, the reactor should be modified to inhibit the circulating gas flow

Chapter 7. Generation of charged nanoparticles during thermal evaporation of silver at atmospheric pressure

1. INTRODUCTION

Nanoparticles (NPs) have received great attentions due to their unique properties distinguished from bulk materials. They have unusual electromagnetic, optical and mechanical properties that can be applied to various fields of industry (Ozin [95]; Barnes, Dereux [96]). Especially silver nanoparticles, which have outstanding conductivity, are applied to conductive ink and paste ([97]; [98]). The demand for silver nanopowder and thin films increases with the growth of photovoltaic and display markets ([99]).

Most commercial metal powders are produced by a liquid or vapor synthesis. The liquid phase synthesis needs additional processes to remove impurities and to dry powders, although it has an advantage of producing uniform-sized powders and controlling the reaction relatively easily. The vapor phase synthesis has an advantage of not needing such additional processes and of producing powder with high purity ([98]). For the production of the suitable nanopowder using the vapor phase synthesis such as spray pyrolysis, chemical vapor condensation (CVC) and physical vapor condensation ([41]), the nucleation should be made to occur extensively in the gas phase and the nuclei are made to grow to a suitable size. Therefore fundamental understanding of the nucleation and growth behavior of nanoparticles is a key to make a systematic approach to the synthesis of nanopowder.

Considering the previous reports that charged nanoparticles were generated without exception under typical film processing conditions in the CVD process, the generation of CNPs is also expected during thermal evaporation of metals at atmospheric pressure. Although it is well known that nanoparticles are generated

during thermal evaporation at atmospheric pressure, it has been implicitly assumed that those nanoparticles are electrically neutral because no intentional effort is made to charge them. The purpose of this paper is to examine the possibility that silver nanoparticles generated during thermal evaporation at atmospheric pressure might be electrically charged using the nano-DMA combined with a Faraday cup electrometer (FCE). The deposition behavior of CNPs is also studied.

2. EXPERIMENTAL DETAILS

Silver was thermally evaporated at atmospheric pressure under flowing nitrogen. A ceramic heater connected with an AC power supply was used to heat the silver powder above its melting point. The heater plate of $50 \times 5 \times 1.5 \text{ mm}^3$ was placed in the small quartz reactor 34 mm in diameter and 100 mm in length. The schematic of the experimental setup is shown in Fig. 1. In order to confirm the generation of charged silver nanoparticles during thermal evaporation at atmospheric pressure, a DMA was connected to the quartz reactor as shown in Fig. 1. If charged nanoparticles are generated in the quartz reactor, they are passed through the DMA after being sampled in the quartz reactor by the tube and then size-classified by the electric field. The amount of size-selected charged nanoparticles is detected as electric current on the FCE. Finally, the current data are converted to determine the size distribution of charged nanoparticles. The DMA used was a nano-DMA (TSI Inc., 3085) which can measure the size range of 1 to 100 nm. The deposition behavior of nanoparticles on the quartz substrate was examined by field-emission scanning electron microscope (FE-SEM) with various nitrogen flow rates of 0.5, 1, 2 and 4 l/min. The evaporation

temperature was controlled by modulating AC voltage levels (70 V, 90 V, 110 V and 120 V). Initial weight of silver chosen for evaporation varied from 0.01g to 0.2g.

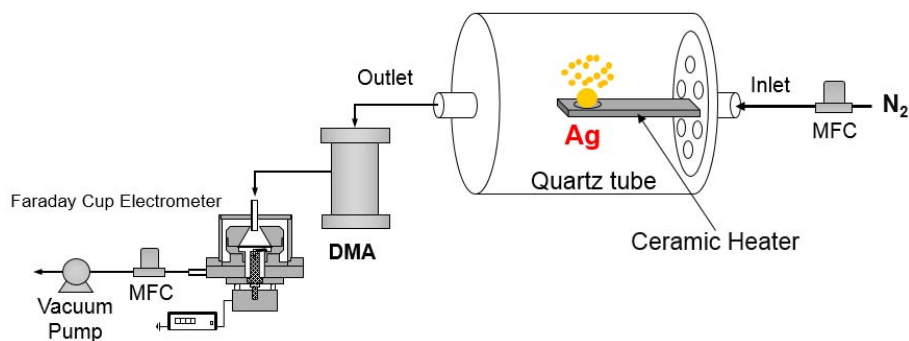


Fig. 1. Schematic of experimental set of the DMA-FCE system.

The gas flow in the reactor, which affects the deposition of nanoparticles, was analyzed by computational fluid dynamics (CFD) calculation under the condition of 1215 °C and the gas flow rate of 1 l/min. To examine the deposition behavior on different locations, quartz substrates about 1×1 cm² were placed in various positions around the heater. One substrate was placed above the heater. Other substrates at intervals of 2 mm or at intervals of 50 mm were placed horizontally with the heater. The deposition was done for 30 min at the evaporation temperature of 1215 °C under the nitrogen flow rate of 1 l/min. Since the electric bias is expected to affect the deposition behavior of charged nanoparticles, the direct current (DC) bias of -200 V was applied to the stainless steel substrate holder.

3. RESULTS

Under all experimental conditions, the generation of charged silver nanoparticles was confirmed by DMA. Fig. 2 shows that the size distribution of both positively and negatively charged nanoparticles is varied with the evaporation temperature under a nitrogen flow rate of 1 l/min. At 975 °C which is slightly higher than the melting point (961 °C) of silver, the mean diameter and the number density of nanoparticles were the smallest in Fig. 2(a). As the temperature increased, the number density also increased. When the temperature increased from 975 °C to 1035 °C, the mean diameter of positively charged nanoparticles increased but when the temperature further increased to 1155 °C and 1215 °C, the mean diameter slightly decreased. The diameter of both positively and negatively charged nanoparticles varied from 3.5 to 95 nm. The total number concentrations of positively and negatively charged nanoparticles varied from 20×10^5 to 30×10^5 and from 50×10^5 to 25×10^5 particles/cm³, respectively. Fig. 2(b) shows that negatively charged nanoparticles were not detected at relatively low temperatures of 975 °C and 1035 °C in Fig. 2(b).

Fig. 3 shows how the size distribution is varied with the nitrogen flow rate (0.5, 1, 2, and 4 l/min) at the evaporation temperature of 1215 °C. The ranges of the diameter and number concentration are similar to those in Fig. 2. As the nitrogen flow rate increased from 0.5 l/min to 1 l/min, the number density increased but the mean diameter slightly decreased. When the flow rate increased further to 2 l/min and 4 l/min, the number density and the mean diameter changed only slightly.

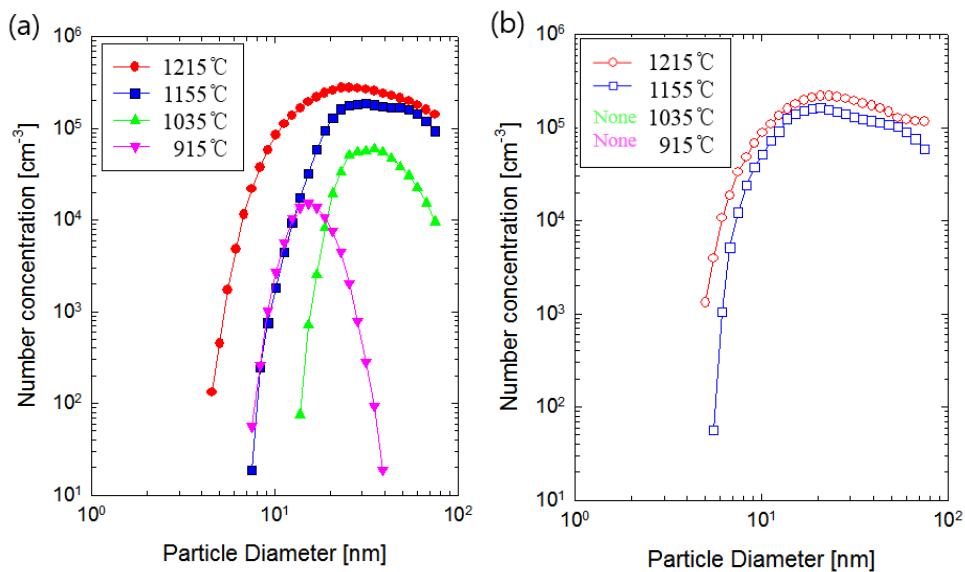


Fig. 2. The size distribution of (a) positively and (b) negatively charged nanoparticles at the nitrogen flow rate of 1000 sccm and the initial silver of 0.01 g.

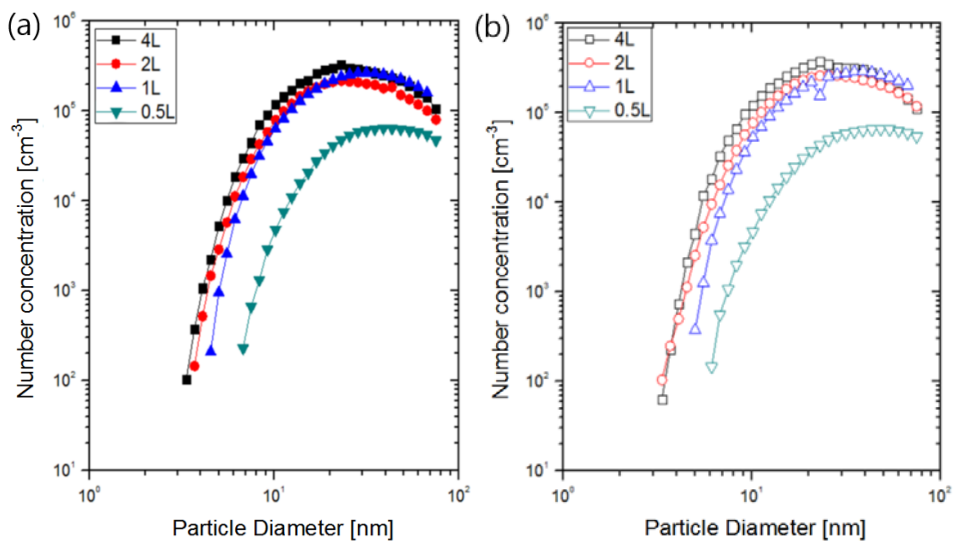


Fig. 3. The size distribution of (a) positively and (b) negatively charged nanoparticles with varying flow rate of nitrogen at the evaporation temperature of 1215 °C and the initial silver of 0.01 g.

Fig. 4 shows how the size distribution is varied with the initial weight of silver to be evaporated at the evaporation temperature of 1215 °C and the nitrogen flow rate of 1 l/min. With increasing initial weight of silver, the number density of both positively and negatively charged nanoparticles did not change much and the mean diameter decreased slightly.

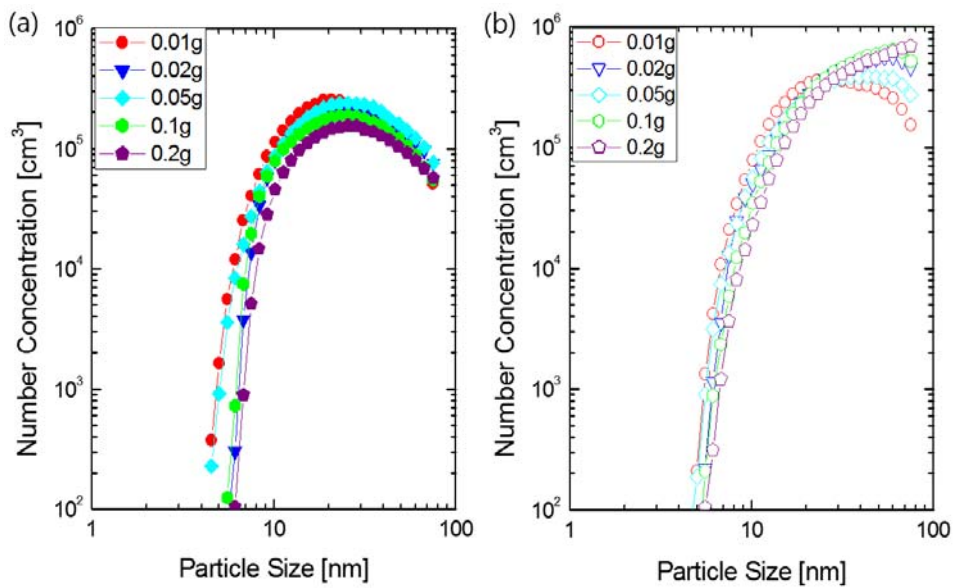


Fig. 4. The size distribution of (a) positively and (b) negatively charged nanoparticles with varying initial weight of silver at the evaporation temperature of 1215 °C and the nitrogen flow rate of 2000 sccm.

The motion of nanoparticles is affected by the gas flow because of the drag force. Therefore their deposition behavior will be affected by the gas flow. The gas flow in

the reactor can be calculated by CFD (ANSYS Fluent v16.0), which can numerically analyze the fluid flow.

The gas interacts with the surface, which is defined by the boundary condition. Fig. 5 shows the fluid flow in a quartz tube at the evaporation temperature of 1215 °C, indicating that the heated gas moves upward and escapes to the outside along the inner wall. Near the ceramic heater, the temperature gradient is steep. As a result, the gas moves upward rapidly and moves outside slowly at around 1.3×10^{-1} m/s.

Fig. 6 shows the deposition behavior on two different locations, upper and beside the ceramic heater. SEM images of silver thin films deposited on these two locations matched with the result of the calculation by CFD. According to the CFD calculations, most of evaporated silver nanoparticles are expected to deposit on the quartz substrate above the ceramic heater. In accordance with these calculations, a smooth and dense thin film was formed on the upper substrate whereas an irregular thin film was deposited on the substrate beside the heater. Therefore, the convection in the evaporation reactor is an important factor in the deposition of nanoparticles.

To examine the effect of the applied bias on the film microstructure, the bias of -200 V was applied to the stainless steel substrate holder with the quartz substrates placed with intervals of 2 mm horizontally with the ceramic heater. Fig. 7(a), which is the thin film deposited without bias, shows a highly irregular surface, whereas Fig. 7(b), which is the thin film deposited under -200 V, show a rather smoother surface. This results not only indicates that an appreciable percentage of nanoparticles generated in the gas phase is electrically charged but also indicates that a film microstructure can be controlled by applying the bias, which accelerates charged nanoparticles.

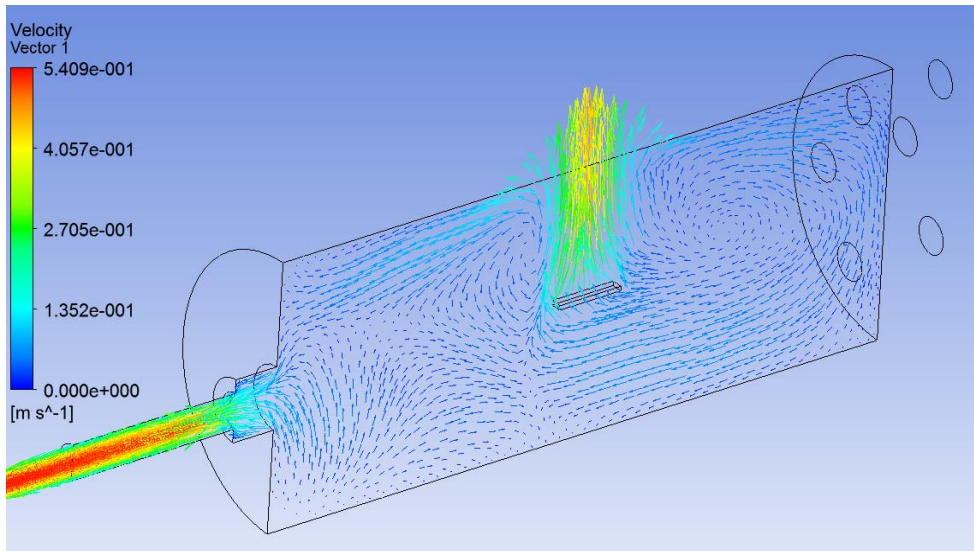
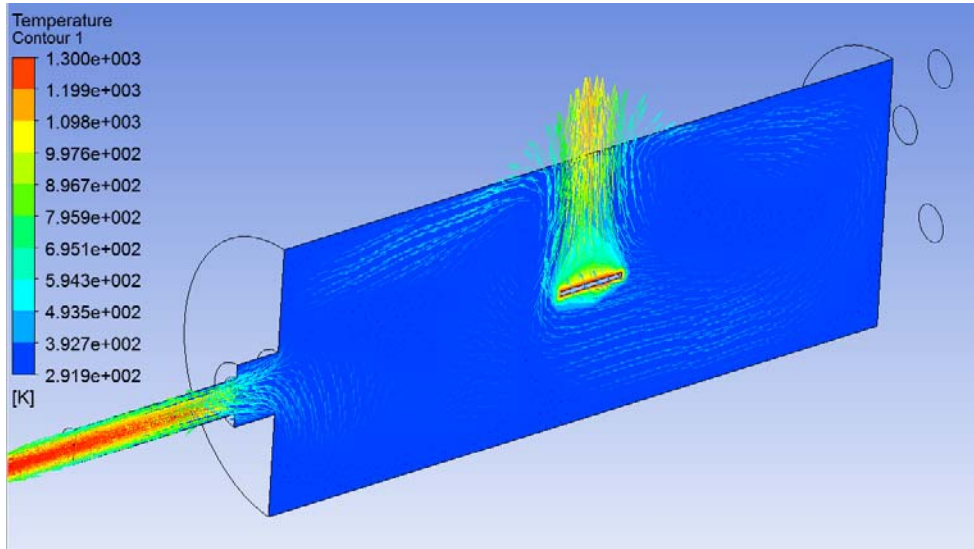


Fig. 5. CFD analysis of (a) temperature in a reactor and (b) gas flow velocity.

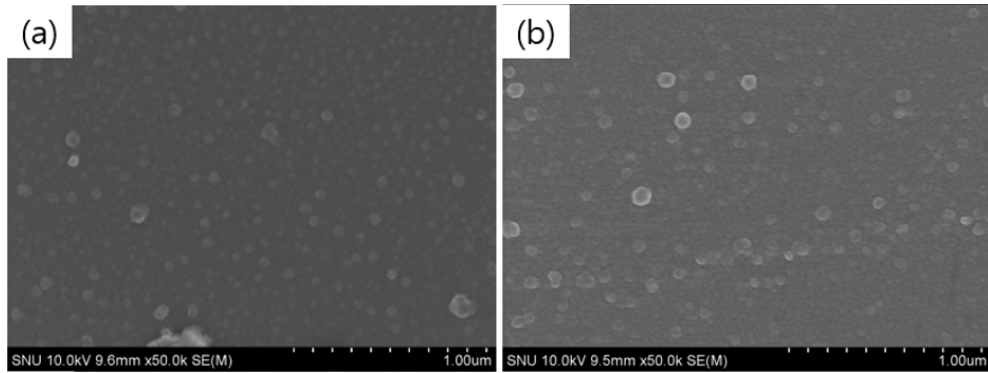


Fig. 6. SEM images of silver thin films deposited for 30 min on quartz substrates (a) beside (b) above the ceramic heater at the evaporation temperature of 1215 °C, and the nitrogen flow rate of 1000 sccm.

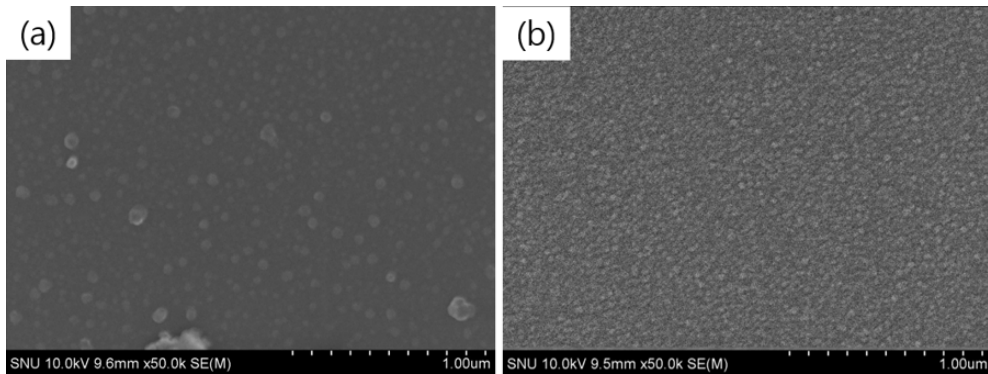


Fig. 7. SEM images of silver thin films deposited for 30 min under the bias (a) 0 V and (b) -200 V applied to the stainless steel substrate holder at the evaporation temperature of 1215 °C, and the nitrogen flow rate of 1000 sccm.

4. DISCUSSION

This study confirms that an appreciable percentage of nanoparticles generated during thermal evaporation at atmospheric pressure is electrically charged. The determination of the relative percentage between charged and neutral particles is another problem, which is our future topic. The generation of charged nanoparticles from hot surfaces was first reported by Schmidt-Ott et al. in 1980, whose fact has been used widely for the production of metallic particles ([100]; [101]; [102]; [103]). Schmidt-Ott et al. reported that large photoconductivity resulted from the photoelectrons emitted when photon collides with small particles below 50 Å. It can induce aerosol to have a small negative charge, at the same time particles left with a positive charge ([100]).

Considering that charging occurs at relatively low temperature in a non-plasma condition in our experiment, the activation energy for charging appears to be low. One possible mechanism of charging is that nanoparticles are formed first by evaporation and then the nanoparticles undergo the surface ionization after being in contact with any surface in the reactor. If the nanoparticle undergoes the positive surface ionization, it will be positively charged and vice versa. This mechanism was suggested by Jeon et al. ([104]; [105]). In this case, the activation energy would be the difference in the work function between nanoparticles and any surface being in contact with nanoparticles. It is easy that nanoparticles formed during evaporation undergo the positive surface ionization since they have much smaller ionization energy which decreases with their increasing size than atoms ([104]). Jeon et al. explained the origin of positively charging of nanoparticles generated during thermal evaporation of copper ([104]) and silver ([105]) by comparing the work function of each of the metals and an oxidized tungsten basket surface.

Another possible mechanism for positive charging would be the positive surface ionization of the alkali metals, which may exist as impurities in silver and have low ionization energy. This mechanism was suggested by Peineke et al. based on the observation that wires of different purities and with purification by out-gassing at high temperatures led to pronounced differences in positive particle production ([106, 107]). The amount of positively charged nanoparticles increased with impurity concentration of wires at other same conditions ([106]). Peineke and Schmidt-Ott further suggested that the source of negative charge might come from electrons emitted from the heated metal. Peineke et al. explained the possibility that electrons can be emitted from heated surfaces at high temperature and obtained the negative current density using the Richardson equation ([107]).

The reason why negatively charged nanoparticles are not measured at low evaporation temperature whereas positively charged nanoparticles are measured in Fig. 2 might be related with the charging mechanism. If the origin of negative charge comes from the thermionic emission of the heated metal surface as suggested by Peineke and Schmidt-Ott, the absence of negatively charged nanoparticles might be attributed to the lack of thermionic electron emission at low temperature ([107]).

Although the data of neutral nanoparticles are absent in this work, they are expected to exist. Since the collision and coagulation between charged and neutral nanoparticles produce the charged nanoparticles, the percentage of neutral nanoparticles at atmospheric pressure would be far less than that at low pressure.

The fact that charged nanoparticles are generated during evaporation of metals can be utilized in various ways. One possibility is to produce the monodisperse nanoparticles because their size can be selected by applying electric field based on a

similar concept of the size selection used in the DMA. The other possibility would be to apply the electric bias, which can produce a higher deposition rate or a smoother surface as demonstrated in Fig. 7.

5. CONCLUSION

Charged nanoparticles are generated during thermal evaporation of silver at atmospheric pressure under all processing conditions adopted in this study. The deposition behavior was affected strongly by the applied bias, implying that charged nanoparticles are actively involved in the deposition. This study added the confirmation of the charged nanoparticle generation during thermal evaporation of silver at atmospheric pressure to the previous confirmation that charged nanoparticles were generated during many chemical vapor deposition processes at low pressure as well as atmospheric pressure, extending the generality for the generation of charged nanoparticles.

REFERNCES

1. Fahlman, B.D., *Materials chemistry*. Springer, Mount Pleasant, 2007: p. 282-283.
2. Halperin, W., *Quantum size effects in metal particles*. Reviews of Modern Physics, 1986. **58**(3): p. 533.
3. Klabunde, K.J. and R. Richards, *Nanoscale materials in chemistry*. Vol. 1035. 2001: Wiley Online Library.
4. Schmid, G., *Nanoparticles: From Theory to Application*. Wiley-VCH, Weinheim, 2004.
5. Au, L., et al., *A quantitative study on the photothermal effect of immuno gold nanocages targeted to breast cancer cells*. *ACS Nano*, 2008. **2**(8): p. 1645-1652.
6. Cang, H., et al., *Gold nanocages as contrast agents for spectroscopic optical coherence tomography*. *Optics Letters*, 2005. **30**(22): p. 3048-3050.
7. Chen, J., et al., *Gold nanocages: Bioconjugation and their potential use as optical imaging contrast agents*. *Nano Letters*, 2005. **5**(3): p. 473-477.
8. Cheng, M.M.C., et al., *Nanotechnologies for biomolecular detection and medical diagnostics*. *Current Opinion in Chemical Biology*, 2006. **10**(1): p. 11-19.
9. Fortina, P., et al., *Applications of nanoparticles to diagnostics and therapeutics in colorectal cancer*. *Trends in Biotechnology*, 2007. **25**(4): p. 145-152.
10. Hamilton, J., *The silver halide photographic process*. *Advances in Physics*, 1988. **37**(4): p. 359-441.
11. Jain, P.K., I.H. El-Sayed, and M.A. El-Sayed, *Au nanoparticles target cancer*. *Nano Today*, 2007. **2**(1): p. 18-29.

12. Jeong, S., et al., *Controlling the thickness of the surface oxide layer on Cu nanoparticles for the fabrication of conductive structures by ink-jet printing*. *Advanced Functional Materials*, 2008. **18**(5): p. 679-686.
13. Maier, S.A., et al., *Plasmonics - A route to nanoscale optical devices*. *Advanced Materials*, 2001. **13**(19): p. 1501-+.
14. Murray, C., et al., *Monodisperse 3d Transition-Metal (Co, Ni, Fe) Nanoparticles and Their Assembly into Nanoparticle Superlattices*. *Mrs Bulletin*, 2001. **26**(12): p. 985-991.
15. Nicewarner-Peña, S.R., et al., *Submicrometer Metallic Barcodes*. *Science*, 2001. **294**(5540): p. 137-141.
16. Sanders, A.W., et al., *Observation of plasmon propagation, redirection, and fan-out in silver nanowires*. *Nano Letters*, 2006. **6**(8): p. 1822-1826.
17. Skrabalak, S.E., et al., *Gold nanocages for cancer detection and treatment*. *Nanomedicine*, 2007. **2**(5): p. 657-668.
18. Skrabalak, S.E., et al., *Gold nanocages for biomedical applications*. *Advanced Materials*, 2007. **19**(20): p. 3177-3184.
19. Somorjai, G.A., *Modern Surface Science and Surface Technologies: An Introduction*. *Chemical Reviews*, 1996. **96**(4): p. 1223-1236.
20. Tani, T., *Physics of the photographic latent image*. *Physics Today*, 2008. **42**(9): p. 36-41.
21. Taton, T.A., C.A. Mirkin, and R.L. Letsinger, *Scanometric DNA array detection with nanoparticle probes*. *Science*, 2000. **289**(5485): p. 1757-1760.
22. Templeton, A.C., W.P. Wuelfing, and R.W. Murray, *Monolayer-protected cluster molecules*. *Accounts of Chemical Research*, 2000. **33**(1): p. 27-36.

23. Tkachenko, A.G., et al., *Multifunctional gold nanoparticle-peptide complexes for nuclear targeting*. Journal of the American Chemical Society, 2003. **125**(16): p. 4700-4701.
24. Wang, H., et al., *Plasmonic nanostructures: Artificial molecules*. Accounts of Chemical Research, 2007. **40**(1): p. 53-62.
25. West, J.L. and N.J. Halas, *Engineered nanomaterials for biophotonics applications: Improving sensing, imaging, and therapeutics*. Annual Review of Biomedical Engineering, 2003. **5**: p. 285-292.
26. Yang, X.M., et al., *Photoacoustic tomography of a rat cerebral cortex in vivo with au nanocages as an optical contrast agent*. Nano Letters, 2007. **7**(12): p. 3798-3802.
27. Zhang, X.Y., et al., *Rapid detection of an anthrax biomarker by surface-enhanced Raman spectroscopy*. Journal of the American Chemical Society, 2005. **127**(12): p. 4484-4489.
28. Kishi, H., Y. Mizuno, and H. Chazono, *Base-metal electrode-multilayer ceramic capacitors: past, present and future perspectives*. Japanese Journal of Applied Physics, 2003. **42**(1R): p. 1.
29. Tsantilis, S. and S.E. Pratsinis, *Soft-and hard-agglomerate aerosols made at high temperatures*. Langmuir, 2004. **20**(14): p. 5933-5939.
30. Eggersdorfer, M.L. and S.E. Pratsinis, *Agglomerates and aggregates of nanoparticles made in the gas phase*. Advanced Powder Technology, 2014. **25**(1): p. 71-90.
31. Nichols, G., et al., *A review of the terms agglomerate and aggregate with a recommendation for nomenclature used in powder and particle characterization*. Journal of pharmaceutical sciences, 2002. **91**(10): p. 2103-2109.

32. Wu, S.H. and D.H. Chen, *Synthesis and stabilization of Ni nanoparticles in a pure aqueous CTAB solution*. Chemistry Letters, 2004. **33**(4): p. 406-407.
33. Xia, B., I.W. Lenggoro, and K. Okuyama, *Preparation of Nickel Powders by Spray Pyrolysis of Nickel Formate*. Journal of the American Ceramic Society, 2001. **84**(7): p. 1425-1432.
34. Carenco, S., et al., *Controlled design of size-tunable monodisperse nickel nanoparticles*. Chemistry of Materials, 2010. **22**(4): p. 1340-1349.
35. Tseng, W.J. and C.-N. Chen, *Dispersion and rheology of nickel nanoparticle inks*. Journal of materials science, 2006. **41**(4): p. 1213-1219.
36. Gurav, A., et al., *Aerosol processing of materials*. Aerosol science and technology, 1993. **19**(4): p. 411-452.
37. Klabunde, K.J. and R.M. Richards, *Nanoscale materials in chemistry*. 2009: John Wiley & Sons.
38. Schmid, G., *Nanoparticles: from theory to application*. 2011: John Wiley & Sons.
39. Sugimoto, T., *Monodispersed particles*. 2001: Elsevier.
40. Hwang, N.-M., D.-K. Lee, and J.-S. Jung, *Thermodynamics and Kinetics in the Synthesis of Monodisperse Nanoparticles*. 2012: INTECH Open Access Publisher.
41. Swihart, M.T., *Vapor-phase synthesis of nanoparticles*. Current Opinion in Colloid & Interface Science, 2003. **8**(1): p. 127-133.
42. Seol, K.S., et al., *Gas-phase production of monodisperse lead zirconate titanate nanoparticles*. Applied physics letters, 2002. **81**(10): p. 1893-1895.
43. Park, J., et al., *Ultra-large-scale syntheses of monodisperse nanocrystals*. Nat Mater, 2004. **3**(12): p. 891-895.

44. Park, J., et al., *Synthesis of Monodisperse Spherical Nanocrystals*. Angewandte Chemie International Edition, 2007. **46**(25): p. 4630-4660.
45. Keskinen, H., et al., *Size-selected agglomerates of SnO₂ nanoparticles as gas sensors*. Journal of Applied Physics, 2009. **106**(8): p. 084316.
46. Skandan, G., et al., *Synthesis of oxide nanoparticles in low pressure flames*. Nanostructured materials, 1999. **11**(2): p. 149-158.
47. Hong, J.-S., et al., *Equilibrium shape of nickel crystal*. Philosophical Magazine, 2009. **89**(32): p. 2989-2999.
48. Cölfen, H. and M. Antonietti, *Mesocrystals and Nonclassical Crystallization in Mesocrystals and Nonclassical Crystallization*. 2008, John Wiley & Sons, Ltd. p. 1-276.
49. Alivisatos, A., *Naturally aligned nanocrystals*. Science, 2000. **289**(5480): p. 736-737.
50. Gebauer, D. and H. Cölfen, *Pre-nucleation clusters and non-classical nucleation*. Nano Today, 2011. **6**(6): p. 564-584.
51. Li, D., et al., *Direction-specific interactions control crystal growth by oriented attachment*. Science, 2012. **336**(6084): p. 1014-1018.
52. Niederberger, M. and H. Cölfen, *Oriented attachment and mesocrystals: non-classical crystallization mechanisms based on nanoparticle assembly*. Physical Chemistry Chemical Physics, 2006. **8**(28): p. 3271-3287.
53. Zhang, Z., et al., *Three-Dimensionally Oriented Aggregation of a Few Hundred Nanoparticles into Monocrystalline Architectures*. Advanced Materials, 2005. **17**(1): p. 42-47.
54. Leite, E., et al., *Crystal growth in colloidal tin oxide nanocrystals induced by coalescence at room temperature*. Applied Physics Letters, 2003. **83**(8): p. 1566-1568.

55. Liao, H.-G., et al., *Real-time imaging of Pt3Fe nanorod growth in solution*. science, 2012. **336**(6084): p. 1011-1014.
56. Yuk, J.M., et al., *High-resolution EM of colloidal nanocrystal growth using graphene liquid cells*. Science, 2012. **336**(6077): p. 61-64.
57. Hwang, N.-M. and D.-K. Lee, *Charged nanoparticles in thin film and nanostructure growth by chemical vapour deposition*. Journal of Physics D: Applied Physics, 2010. **43**(48): p. 483001.
58. Hwang, N.-M. and D.-Y. Kim, *Charged clusters in thin film growth*. International materials reviews, 2004. **49**(3-4): p. 171-190.
59. Youn, W.-K., et al., *Comparison of the Deposition Behavior of Charged Silicon Nanoparticles between Floating and Grounded Substrates*. The Journal of Physical Chemistry C, 2014. **118**(22): p. 11946-11953.
60. Fuchita, E., et al., *Appearance of high-temperature phase in zirconia films made by aerosol gas deposition method*. Journal of the Ceramic Society of Japan, 2011. **119**(1388): p. 271-276.
61. Fuchita, E., et al., *High-temperature phase in zirconia film fabricated by aerosol gas deposition and its change upon subsequent heat treatment*. JOURNAL OF THE CERAMIC SOCIETY OF JAPAN, 2013. **121**(1412): p. 333-337.
62. Kim, C.-S., et al., *Generation of charged nanoparticles during synthesis of ZnO nanowires by carbothermal reduction*. Aerosol Science and Technology, 2009. **43**(2): p. 120-125.
63. Kim, C.-S., et al., *Generation of charged nanoparticles during the synthesis of carbon nanotubes by chemical vapor deposition*. Carbon, 2009. **47**(10): p. 2511-2518.

64. Kim, C.-S., et al., *Generation of charged nanoparticles during the synthesis of silicon nanowires by chemical vapor deposition*. The Journal of Physical Chemistry C, 2010. **114**(8): p. 3390-3395.
65. Kim, C.-S., W.-K. Youn, and N.-M. Hwang, *Generation of charged nanoparticles and their deposition during the synthesis of silicon thin films by chemical vapor deposition*. Journal of Applied Physics, 2010. **108**(1): p. 014313.
66. Lee, S.-S., C.-S. Kim, and N.-M. Hwang, *Generation of Charged Nanoparticles During the Synthesis of GaN Nanostructures by Atmospheric-Pressure Chemical Vapor Deposition*. Aerosol Science and Technology, 2012. **46**(10): p. 1100-1108.
67. Hong, J.-S., et al., *In-Situ Measurements of Charged Nanoparticles Generated During Hot Wire Chemical Vapor Deposition of Silicon Using Particle Beam Mass Spectrometer*. Aerosol Science and Technology, 2013. **47**(1): p. 46-51.
68. Bube, R.H., *Electrons in Solids*. 1992: Academic Press.
69. Kingdon, I.L.a.K.H., Proc. R. Soc. London, Ser. A, 1925. **107**: p. 61.
70. Gao, W., S. Shen, and Y. Cheng, *Synthesis of dispersed superfine fcc nickel single crystals in gas phase*. The Journal of Physical Chemistry C, 2013. **117**(18): p. 9223-9228.
71. LaGrow, A.P., et al., *Synthesis, alignment, and magnetic properties of monodisperse nickel nanocubes*. Journal of the American Chemical Society, 2011. **134**(2): p. 855-858.
72. Chen, K., et al., *Catalytic properties of nanostructured hydrogen storage nickel particles with cerium shell structure*. Nanostructured materials, 1997. **8**(2): p. 205-213.

73. Kim, K.H., et al., *Preparation of submicron nickel powders by microwave-assisted hydrothermal method*. Materials chemistry and physics, 2005. **92**(1): p. 234-239.
74. Park, S.H., et al., *Control of size and morphology in Ni particles prepared by spray pyrolysis*. Journal of Materials Science Letters, 2003. **22**(21): p. 1537-1541.
75. Zhang, Z.-p., et al., *Three-dimensionally oriented aggregation of a few hundred nanoparticles into monocrystalline architectures*. Advanced Materials, 2005. **17**(1): p. 42-47.
76. Sunagawa, I., *Growth and morphology of diamond crystals under stable and metastable conditions*. Journal of Crystal Growth, 1990. **99**(1): p. 1156-1161.
77. Williams, E.D. and N.C. Bartelt, *Surface faceting and the equilibrium crystal shape*. Ultramicroscopy, 1989. **31**(1): p. 36-48.
78. Zhu, C., et al., *Kinetically controlled overgrowth of Ag or Au on Pd nanocrystal seeds: from hybrid dimers to nonconcentric and concentric bimetallic nanocrystals*. Journal of the American Chemical Society, 2012. **134**(38): p. 15822-15831.
79. Pang, M., et al., *Highly monodisperse MIII-based soc-MOFs (M= In and Ga) with cubic and truncated cubic morphologies*. Journal of the American Chemical Society, 2012. **134**(32): p. 13176-13179.
80. Xiong, Y., et al., *Size-dependence of surface plasmon resonance and oxidation for Pd nanocubes synthesized via a seed etching process*. Nano letters, 2005. **5**(7): p. 1237-1242.
81. Zhang, Y., et al., *Highly selective synthesis of catalytically active monodisperse rhodium nanocubes*. Journal of the American Chemical Society, 2008. **130**(18): p. 5868-5869.

82. Xia, X., et al., *Quantitative analysis of the role played by poly (vinylpyrrolidone) in seed-mediated growth of Ag nanocrystals*. Journal of the American Chemical Society, 2012. **134**(3): p. 1793-1801.
83. Ren, J. and R.D. Tilley, *Preparation, self-assembly, and mechanistic study of highly monodispersed nanocubes*. Journal of the American Chemical Society, 2007. **129**(11): p. 3287-3291.
84. Sun, Y. and Y. Xia, *Shape-controlled synthesis of gold and silver nanoparticles*. Science, 2002. **298**(5601): p. 2176-2179.
85. Harris, P., *Sulphur-induced faceting of platinum catalyst particles*. Nature, 1986. **323**: p. 792-794.
86. Cabié, M., et al., *Direct observation of the reversible changes of the morphology of Pt nanoparticles under gas environment*. The Journal of Physical Chemistry C, 2010. **114**(5): p. 2160-2163.
87. Forsman, J., et al., *Production of cobalt and nickel particles by hydrogen reduction*. Journal of Nanoparticle Research, 2008. **10**(5): p. 745-759.
88. Sato, N., H. Katayama, and S. Ogasawara, *Ni fine powder for multi-layer ceramic capacitors manufactured by chemical vapor deposition method*. Kawasaki Steel Giho, 2002. **34**(3): p. 120-124.
89. Zucker, R.V., et al., *New software tools for the calculation and display of isolated and attached interfacial-energy minimizing particle shapes*. Journal of Materials Science, 2012. **47**(24): p. 8290-8302.
90. Foo, K. and B. Hameed, *Insights into the modeling of adsorption isotherm systems*. Chemical Engineering Journal, 2010. **156**(1): p. 2-10.
91. Sato, S., et al., *Mechanism of improvement of resistance degradation in Y-doped BaTiO₃ based MLCCs with Ni electrodes under highly accelerated*

- life testing*. Journal of the European Ceramic Society, 1999. **19**(6): p. 1061-1065.
92. Huang, G.-y., et al., *Preparation of fine nickel powders via reduction of nickel hydrazine complex precursors*. Transactions of Nonferrous Metals Society of China, 2009. **19**(2): p. 389-393.
93. Blokhin, A. and M. Blokhina, *Production of spherical powders of palladium and its alloys with silver for multilayer ceramic capacitors*. Powder Metallurgy and Metal Ceramics, 1995. **33**(1): p. 97-99.
94. Pankratz, L., J. Stuve, and N. Gokcen, *Thermodynamic data for mineral technology*. 1984.
95. Ozin, G.A., *Nanochemistry: Synthesis in diminishing dimensions*. Advanced Materials, 1992. **4**(10): p. 612-649.
96. Barnes, W.L., A. Dereux, and T.W. Ebbesen, *Surface plasmon subwavelength optics*. Nature, 2003. **424**(6950): p. 824-830.
97. Tsai, J.T. and S.T. Lin, *Silver powder effectiveness and mechanism of silver paste on silicon solar cells*. Journal of Alloys and Compounds, 2013. **548**: p. 105-109.
98. Puchalski, M., et al., *The applicability of global and surface sensitive techniques to characterization of silver nanoparticles for Ink-Jet printing technology*. Silver Nanoparticles, 2010: p. 63-78.
99. Inberg, A., et al., *Silver nanometer-scale thin films by electroless deposition on insulating surfaces activated by gold nanoparticles*. Electrochimica Acta, 2013. **113**: p. 792-796.
100. Schmidt-Ott, A., P. Schurtenberger, and H. Siegmann, *Enormous yield of photoelectrons from small particles*. Physical Review Letters, 1980. **45**(15): p. 1284.

101. Burtscher, H., et al., *Probing aerosols by photoelectric charging*. Journal of Applied Physics, 1982. **53**(5): p. 3787-3791.
102. Fernandez de la Mora, J., et al., *Mass and size determination of nanometer particles by means of mobility analysis and focused impaction*. Journal of aerosol science, 2003. **34**(1): p. 79-98.
103. Müller, U., A. Schmidt-Ott, and H. Burtscher, *First measurement of gas adsorption to free ultrafine particles: O₂ on Ag*. Physical review letters, 1987. **58**(16): p. 1684.
104. Jeon, I.-D., et al., *Origin of positive charging of nanometer-sized clusters generated during thermal evaporation of copper*. Journal of crystal growth, 2003. **247**(3): p. 623-630.
105. Jeon, I.-D., D.-Y. Kim, and N.-M. Hwang, *Spontaneous generation of charged atoms or clusters during thermal evaporation of silver: Dedicated to Professor Dr. Duk Yong Yoon on the occasion of his 65th birthday*. Zeitschrift für Metallkunde, 2005. **96**(2): p. 186-190.
106. Peineke, C., M. Attoui, and A. Schmidt-Ott, *Using a glowing wire generator for production of charged, uniformly sized nanoparticles at high concentrations*. Journal of aerosol science, 2006. **37**(12): p. 1651-1661.
107. Peineke, C. and A. Schmidt-Ott, *Explanation of charged nanoparticle production from hot surfaces*. Journal of Aerosol Science, 2008. **39**(3): p. 244-252.

APPENDIX

1. The equipments used in this study



Figure 1. Vertical/horizontal switchable reactor with two heating zones.

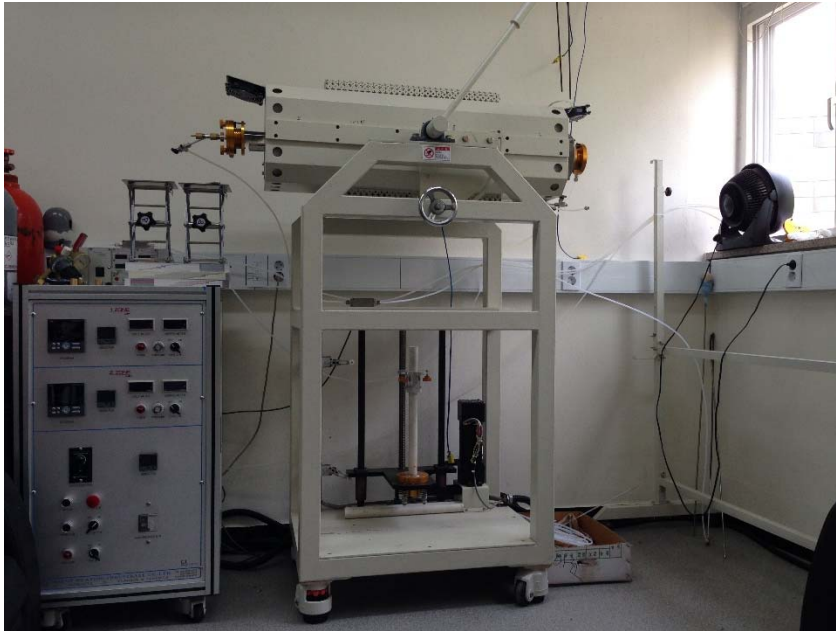


Figure 2. Vertical/horizontal switchable reactor with two heating zones.



Figure 3. Particle collector.

국문초록

니켈 나노입자는 특별한 광학, 자성, 그리고 촉매 특성으로 인해 많은 관심을 받아온 물질이다. 또한, MLCC 의 내부전극 물질로 사용되던 팔라듐의 원가 상승으로 인해, 최근 니켈 나노입자를 팔라듐을 대체하여 내부전극 물질로 사용되기 시작하였다. 한편으로 최근 전자기기의 소형화 추세에 따라 MLCC 또한 소형화 그리고 고용량화가 요구되고 있다. 따라서, 내부전극 물질인 니켈 나노입자 또한 100 nm 이하의 작은 크기가 요구되고 있으며, 또한 높은 적층 밀도를 위해 응집되지 않고 분산이 용이한 구형 형상이 요구되고 있다.

일반적으로 니켈 나노입자는 두 가지 방법으로 합성된다. 하나는 액상법이며 나머지 하나는 기상법이다. 액상법은 나노입자의 크기와 형상을 제어하기에 유리한 것으로 알려져 있다. 하지만, 입자들간의 낮은 결정성, 낮은 순도, 분산이 어려운 점, 계면활성제 등에 의한 오염은 액상법으로 나노입자를 합성할 때 피할 수 없는 문제이다. 대부분의 기상법은 나노입자의 크기와 형상을 제어하기가 까다로운 것으로 알려져 있지만, 액상법으로 얻기 어려운 높은 결정성, 높은 순도와 분산이 용이하다는 점에서 경우에 따라 선호되는 분말 합성법이다. 많은 기상법 중 화학기상증착법이 본 연구에 적용되었으며, 이는 화학기상증착법이

높은 결정성과 높은 순도를 보장하면서도 입자의 크기와 다른 주요 공정변수들을 제어하기가 용이하기 때문이다.

그러나, 기상공정을 통해 나노입자를 합성하게 되면, 보통 입도 분포가 넓고 입자들간의 응집과 응집 후 소결이 일어나 원하는 형상과 크기의 입자를 얻기가 어렵다고 잘 알려져 있다. 본 연구에서는 이러한 기상공정의 문제점을 해결하기 위해 수정된 수직반응기를 적용하였고, 단분산 니켈 입자를 합성하는데 성공하였다. 이 공정은 니켈 화학기상증착 공정에만 적용 가능한 것이 아니라, 기상환원법을 통해 합성할 수 있는 다른 물질들에도 적용이 가능할 것이며, 그 가능성을 철과 코발트 입자를 합성함으로써 확인하였다. 또한, 이 새로운 공정의 메커니즘은 기상환원법뿐 아니라 열분해법이나 물리기상증착법과 같은 공정에도 적용이 가능할 것이라 기대된다.

한편으로 니켈 나노입자의 물성은 크기 뿐 아니라 형상, 조성, 그리고 결정성의 영향을 받는다. 특히 육면체의 니켈입자는 구형일 때 보다 우수한 자성 특성을 갖는 것으로 알려져 있다. 그러나 니켈은 면심입방의 결정 구조를 갖기 때문에, 열역학적으로 불안정한 {100}면이 발달한 육면체를 합성하기 위해서는 {100}면에 선택적으로 흡착하는 계면활성제 등에 의한 {100}면의 선택적 안정이 필요하다. 하지만, 본 연구에서는 특별한 처리 없이 육면체 니켈이 합성되는 것이 확인되었다. 따라서 왜 {100}면의 선택적 안정이 일어나는 지에 관한 연구를 진행하였고, 이를 바탕으로 화학기상증착 공정을 이용한 니켈 입자의

합성에서 형상 제어에 있어 주요 공정변수를 확인하고 제어할 수 있는 기술을 개발하였다.

.....

주요어: 단분산, 니켈 나노입자, 응집, 기상합성공정, 평형상

학번 : 2011-30935